

Proceedings
of the
19th International Conference on
Biomedical Applications of
ELECTRICAL IMPEDANCE TOMOGRAPHY

Edited by Alistair Boyle, Nick Polydorides and Jiabin Jia

June 11–13, 2018
University of Edinburgh
Edinburgh, Scotland, UK



This document is the collection of papers accepted for presentation at the 19th International Conference on Biomedical Applications of Electrical Impedance Tomography (EIT2018), Edinburgh.

Each individual paper in this collection: © 2018 by the indicated authors.

Collected work: © 2018 Alistair Boyle, Nick Polydorides, Jiabin Jia



This work is licensed under a [Creative Commons Attribution 4.0 International License](https://creativecommons.org/licenses/by/4.0/).

Cover design: Alistair Boyle

Photo credit (front cover): Holyrood area of Edinburgh from Calton Hill

Photo credit (back cover): Edinburgh Castle

Printed in the United Kingdom

DOI: [10.5281/zenodo.1210247](https://doi.org/10.5281/zenodo.1210247) (revision 0; conference)

School of Engineering

The University of Edinburgh

Edinburgh, Scotland,

United Kingdom

www.eng.ed.ac.uk

N.Polydorides@ed.ac.uk

+44(0)131 6502769

eit2018.org

Table of Contents

<i>M. Kircher et al.,</i> Method for comparing pulmonary perfusion measured by PET/CT and indicator based EIT measurements in a porcine model	1
<i>Symon Stowe et al.,</i> A comparison of EIT lung perfusion measures	2
<i>Benjamin Hentze et al.,</i> Towards Regional Lung Ventilation to Perfusion Ratio by EIT	3
<i>Sarah J. Hamilton et al.,</i> Deep D-bar for Absolute EIT Imaging: Experimental Results	4
<i>Andy Adler et al.,</i> Comparing D-bar and Regularization-based reconstruction	5
<i>Tomasz Rymarczyk et al.,</i> Using Statistical Methods for Image Reconstruction in Structural Objects	6
<i>Evgeny Tsizin et al.,</i> Passive Electric Impedance Tomography	7
<i>Neeta Ashok Kumar et al.,</i> Electric and Magnetic Field Distributions in Deep Brain Stimulation	8
<i>Barry McDermott et al.,</i> Classification Applied to Brain Haemorrhage Detection: Initial Phantom Studies using Electrical Impedance Measurements	9
<i>Taweechai Ouypornkochagorn et al.,</i> In Vivo Estimation of the Head Tissue Conductivities	10
<i>Leonardo Fiuza et al.,</i> Impedance Change due to Ion Channel Opening in Muscle as a Potential Robust Means for Controlling Bionic Prostheses	11
<i>James Hope et al.,</i> Electrode drive and measurement patterns for EIT of neural activity in peripheral nerve	12
<i>S. J. H. Heines et al.,</i> Effect of a PEEP trial on global inhomogeneity index alveolar overdistension/collapse in cardiothoracic surgery and ARDS patients	13
<i>M. Y. Chang et al.,</i> Patient-ventilator asynchrony	14
<i>F. Thürk et al.,</i> Influence of noise figure controlled regularisation on derived physiological parameters in Electrical Impedance Tomography	15
<i>Saaïd H. Arshad et al.,</i> Norm-Minimized Cardiac-Gated Electrical Impedance Tomography for Stroke Volume Monitoring	16
<i>Tobias Menden et al.,</i> Frequency-Differential Reconstruction Algorithm for Thoracic EIT Using Absolute Values	17
<i>Ethan K. Murphy et al.,</i> Absolute Phantom Reconstructions using Fused-Data EIT	18

Hancong Wu et al.,
Multi-plane electrode configuration for 3D cellular assay of electrical impedance tomography 19

Alistair Boyle et al.,
Integrating Circuit Simulation with EIT FEM Models 20

Wrichik Basu et al.,
Model based EIT signal estimation in the presence of transients: Experimental validation using 3D phantoms and in vivo trials..... 21

Yandan Jiang et al.,
Biomedical Application of Capacitively Coupled Electrical Resistance Tomography (CCERT) 22

Michaël Rapin et al.,
Noise Performance Assessment of a Wearable EIT System..... 23

Christopher A. R. Chapman et al.,
Low impedance multiple electrode array neural cuff for imaging peripheral nerve activity using Electrical Impedance Tomography (EIT) 24

Tobias Becher et al.,
Effect of intravenous fluid administration on end-expiratory lung impedance in critically ill adult patients 25

Claas Strodthoff et al.,
Effect of suctioning on chest EIT findings in neonates:preliminary results of a multicentre clinical study 26

M. Elenkov et al.,
Localisation of pixels representing the aorta in electrical impedance tomography images based on time and frequency domain features..... 27

Andy Adler et al.,
Phase-contrast functional EIT images 28

Munish Chauhan et al.,
Ion diffusion measurement using DT-MREIT 29

Saurav Z. K. Sajib et al.,
Comparison of reconstructed in-vivo current densities for F3-RS and F4-LS electrode montages 30

Saurav Z. K. Sajib et al.,
Comparison of in-vivo DT-MREIT scaling factor images for in- and off-plane current administration of transcranial AC stimulation. 31

Fanrui Fu et al.,
Functional Magnetic Resonance Electrical Impedance Tomography of Salamander Retina 32

Jianping Li et al.,
Red Blood Cells Aggregability Measurement with Multiple-frequency Electrical Impedance Spectroscopy 33

Xiao-Qian Chen et al.,
Biological specimen experimental results of an EIM system..... 34

Attila Toth et al.,
Investigation of Liver Fat Content Using a Bioimpedance Spectrum Measurement Method 35

Ilya Tarotin et al.,
Effect of dispersion in nerve on impedance change: a modelling study 36

Christin Wenzel et al.,
A modulated physical model for simulating regional ventilation with EIT 37

Hyeuknam Kwon et al.,
Intramuscular electrical impedance imaging using a needle device 38

Ethan K. Murphy et al.,
A Coupled US/EIT System for Assessing Muscle Health 39

Eoghan Dunne et al.,
EIT Image-Based Bladder State Classification for Nocturnal Enuresis 40

Hancong Wu et al.,
3D cell spheroids drug response monitoring using electrical impedance tomography 41

<i>Tong In Oh et al.,</i> Development of Multiple Electrodes based Impedance Spectroscopy for Screening of Cervical Dysplasia and Cervical Cancer	42
<i>Andy Adler et al.,</i> Accelerating Space-Time Regularized Reconstructions	43
<i>Shengheng Liu et al.,</i> Sequential EIT Frame Reconstruction Exploiting Spatiotemporal Correlation	44
<i>Ethan K. Murphy et al.,</i> Deep Neural Networks for Noise-Robust Cardiac Output Monitoring	45
<i>Christian Gibas et al.,</i> EIT for recognition of muscle activity for a physiological rehabilitation therapy	46
<i>Yunjie Yang et al.,</i> Quasi-2D EIT-optical Dual Modality Sensor for Cellular Imaging	47
<i>Hyeuknam Kwon et al.,</i> EIT for assessing muscle contractures: A convenient tool for a common condition?	48
<i>Inéz Frerichs et al.,</i> Wearable chest electrical impedance tomography system – a validation study in healthy volunteers	49
<i>Serena de Gelidi et al.,</i> Towards a thoracic conductive phantom for EIT	50
<i>Christos Dimas et al.,</i> A Field Theory Approach in EIT with Green's Functions	51
<i>Ariungerel Jargal et al.,</i> Deep learning method for lung EIT	52
<i>Tingting Zhang et al.,</i> Fat volume quantification by using weighted frequency difference Electrical Impedance Tomography (wfdEIT)	53
<i>Nima Seifnaraghi et al.,</i> Effect of Thorax Deformation during Neonatal Lung EIT	54
<i>Jared Vicory et al.,</i> Creation and Visualization of High-quality Tetrahedral Meshes from Segmentations using 3D Slicer	55
<i>Bo Gong et al.,</i> An efficient classification-reconstruction method for 3D EIT	56
<i>Sabine Krueger-Ziolek et al.,</i> Evaluating the Severity of Cystic Fibrosis related Lung Disease by Electrical Impedance Tomography	57
<i>Anita Just et al.,</i> 3D FEM Simulations of EIT Measurements on the Human Thorax	58
<i>Munish Chauhan et al.,</i> Demonstration of Multi-frequency MREIT using Semipermeable Membrane Models and Experiments	59
<i>Tobias Becher et al.,</i> Clinical acceptance of various EIT parameters in neonatology and paediatrics: A systematic assessment of clinicians' opinions	60
<i>Paul Wright et al.,</i> A 64-channel EIT system for the investigation of optimal measurement approaches for lung protective ventilation ...	61
<i>Bartłomiej Grychtol et al.,</i> Separation of 3D EIT electrode planes	62
<i>Xiaobo Huang et al.,</i> Measures of lung fluid via posture-change fEIT	63
<i>Gerald Sze et al.,</i> Enhanced breast model for EIM simulation	64

Method for comparing pulmonary perfusion measured by PET/CT and indicator based EIT measurements in a porcine model

M. Kircher¹, A. Braune², T. Bluth², M. Gama de Abreu², O. Dössel¹, B. Stender³

¹Institute of Biomedical Engineering, Karlsruhe Institute of Technology, Karlsruhe, Germany, michael.kircher@kit.edu

²Department of Anesthesiology and Intensive Care Medicine, University Hospital Carl Gustav Carus, Dresden, Germany

³Drägerwerk AG & Co. KGaA, Lübeck, Germany

Abstract: The potential of saline indicator based pulmonary perfusion measurements with EIT was investigated in five different lung states of a porcine model. Based on corresponding regions within the relative regional perfusion images overall limits of agreement (LoA) around 10% were determined between EIT and PET/CT measurements.

1 Introduction

Assessing pulmonary perfusion using Electrical Impedance Tomography (EIT) at the bedside could potentially support the optimization of mechanical ventilation in daily clinical routine. The application of a saline solution as an EIT indicator has been studied before [1,2]. In this study, multiple saline concentrations have been used to compute regional lung perfusion maps. The perfusion measured by EIT was compared to PET/CT perfusion as a reference. The method of comparing 2D-EIT and 3D-PET/CT perfusion distributions will be described in the following.

2 Methods

The preclinical study: Five different perfusion conditions were investigated in 13 anesthetized pigs. During each state, pulmonary perfusion was assessed by EIT during respiratory hold phases at mean airway pressure. 10 ml of different indicator concentrations (3%, 5%, 10%) were injected central-venously. Consecutively, PET/CT scanning was performed using ⁶⁸Ga as nuclear tracer.

EIT indicator dilution: EIT measurements were conducted with the PV500 at a frame rate of 50 frames/s. The reconstruction was performed using a general porcine torso shape based on all 13 animals, a homogeneous background conductivity and a 1-step Gauss Newton solver.

The injection of a saline solution results in a regional increase in relative conductivity $\Delta\sigma_{s,i}$ during the presence of the saline bolus in pixel i . Similar to previous analyses [1], a surrogate for the amount of blood flow $q_{EIT,i}$ into pixel i was calculated by:

$$q_{EIT,i} = \left. \frac{d\Delta\sigma_{s,i}}{dt} \right|_{max} \quad (1)$$

A normalized distribution Q_{EIT} is calculated after removing the ventricular region based on pulsatility analysis.

Comparing EIT with PET/CT perfusion: EIT images represent a projection of current flowing within a volume around the electrode plane. Thus, to compare 2D-EIT images and 3D-PET/CT volumes of perfusion adequately, the PET/CT volume should optimally be projected with a profile corresponding to the sensitivity distribution of an EIT measurement. Two projection profiles were hence investigated: 1) rectangular profile (equal weighting of each transversal plane) and 2) bell shaped weighting profile [3]. Finally, the resulting images were subdivided into eight re-

gions of interest (ROIs) to compare both images by means of the Pearson's correlation coefficient (r) and limits of agreement (LoA) of a Bland-Altman analysis. The division of the image into ROIs was performed with two different approaches: a) division based on the centroid of segmented healthy lung tissue of the co-registered CT (ROI_{CT}); b) division based on the centroid of the measured PET/CT distribution (ROI_{PET}). The second one is potentially better accounting for the physiologically inhomogeneous distribution of perfusion within the lung.

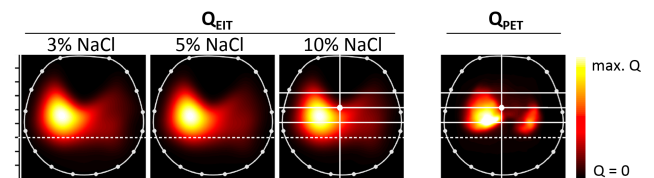


Figure 1: The three images on the left show the relative perfusion measured by EIT, the right image presents the corresponding projected PET image during unilateral ventilation. The CT based ROIs are depicted (white lines).

3 Results

The qualitative comparison for one exemplary lung state is depicted in figure 1. The quantitative measures using a 3% saline solution are shown in table 1.

Table 1: Results of the comparison with different PET projection profiles and in different ROIs for the lowest saline concentration of 3% including all experimental states.

	rectangular profile		simulation profile	
	ROI_{CT}	ROI_{PET}	ROI_{CT}	ROI_{PET}
r	0.87	0.81	0.88	0.85
LoA (%)	10.7	10.4	9.5	10.3

4 Discussion

The comparison of regional perfusion distributions Q_{EIT} and Q_{PET} shows good overall agreement both qualitatively and quantitatively. The potentially more adequate projection profile for the comparison of PET and EIT measurements results in lower LoAs. The ROIs based on CT segmentation might virtually increase the correlation coefficient due to the already inhomogeneous distribution of perfusion within the lungs.

References

- [1] J Borges, F Suarez-Sipmann, S Bohm et al. *J Appl Physiol*, 112: 225–236, 2012
- [2] I Frerichs, J Hinz, P Herrmann et al. *IEEE Trans. Med. Imag.*, 21: 646–652, 2002
- [3] B Stender, J Maier *Conf 16th ICEBI & 17th EIT*, Stockholm, Sweden, Jun 2016

A comparison of EIT lung perfusion measures

Symon Stowe¹, Alistair Boyle¹, Michaël Sage², Mathieu Nadeau², Jean-Paul Praud², Étienne Fortin-Pellerin², Andy Adler¹

¹Carleton University, Ottawa, Canada, andy.adler@carleton.ca

²Université de Sherbrooke, Canada

Abstract: Several different techniques have been proposed to measure the distribution of perfusion in the lung using EIT: using a bolus of hypertonic saline, or frequency filtering the EIT images at the cardiac rate. We compare these techniques in newborn lambs. The preliminary results from two animals show a common trend between bolus injection and frequency analysis measures of perfusion.

1 Introduction

The “holy grail” of EIT-based lung function assessment is measurement of both ventilation and perfusion distribution. While EIT measures of ventilation are reasonably well validated, multiple different measures of perfusion are used and their relationship is poorly understood [1]. True EIT-perfusion measures can be made with a vascular injection of a conductivity contrasting (hypertonic NaCl) fluid, but this is invasive, must be infrequent to avoid hypernatremia, and can affect the EIT signal over time [2]. The second approach uses cardiac-frequency filtering of the time-series EIT images. This shows what has been called “pulsatility”, and is affected by cardiac-related movement and is not sensitive to the continuous blood flow in the capillaries.

Our goal is to compare images from these techniques

to determine whether the distribution of perfusion and its trends are consistent between bolus- and filtering-derived functional images. Data with a large change in ventilation status due to the introduction of total liquid ventilation (TLV) were used [3].

2 Methods & Results

Newborn lambs were anesthetized and ventilated in a supine position. 16-electrode, EIT data were acquired at 4.7 frames/s using the Sigatome II EIT device [4], and the experimental protocol of Fig. 1 used. P_B was measured by a injection of a 7.9% saline solution during an apnoea. P_A and P_V were measured during apnoea and ventilation.

Results show a relationship between images in overall shape and distribution of pulsatility images through the stages of the protocol, from gas ventilation (baseline), through TLV filling, stable (5 minutes) and 2h post filling.

References

- [1] D Nguyen, *et al*, *Physiol Meas* 33:695–706, 2012
- [2] J Yap, *et al*, *Parenteral and Enteral Nutrition* 41:641–646, 2017
- [3] M Sage *et al*, *PloS one*, 13:e0191885, 2018.
- [4] N Robitaille *et al*, *Physiol Meas*, 30:S57–S71, 2009.

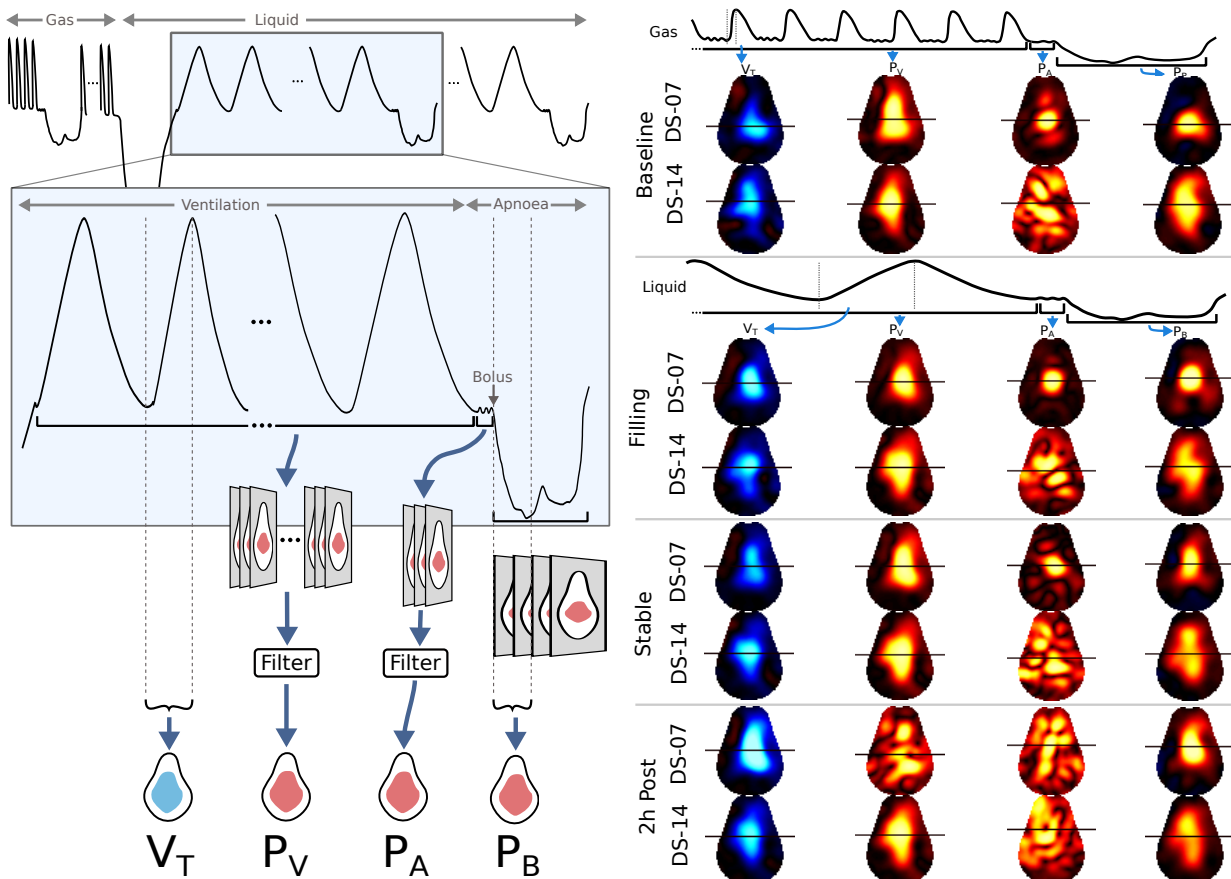


Figure 1: Protocol (left) and Images (right) in two lambs. P_V : pulsatility (perfusion) image during ventilation, from frequency filtering EIT data during ventilation; P_A : pulsatility (perfusion) image during apnoea, from frequency filtering EIT data during apnoea; P_B : perfusion image from bolus, calculated between bolus measures and an apnoea reference measure; and V_T : tidal ventilation image.

Towards Regional Lung Ventilation to Perfusion Ratio by EIT

Benjamin Hentze^{1,2}, Thomas Muders², Christian Putensen², Steffen Leonhardt¹, Marian Walter¹

¹Philips Chair for Medical Information Technology, RWTH Aachen University, Germany, hentze@hia.rwth-aachen.de

²Department of Anaesthesiology and Intensive Care Medicine, University of Bonn, Germany

Abstract: In order to analyze the feasibility of monitoring regional lung ventilation to perfusion ratio (\dot{V}/\dot{Q}) by electrical impedance tomography (EIT), we validated regional ventilation (\dot{V}) and perfusion (\dot{Q}) by EIT against single-photon emission computed tomography (SPECT). While individual assessment of \dot{V} and \dot{Q} is possible, substantial research is necessary to enable \dot{V}/\dot{Q} by EIT.

1 Introduction

In intensive care patients with acute respiratory distress syndrome (ARDS), lung gas exchange is often severely impaired. EIT is a noninvasive imaging modality that allows real-time monitoring of \dot{V} at bedside [1]. Furthermore, it was shown that \dot{Q} can be obtained by bolus injection of saline into the central venous catheter (CVC) [2]. Since gas exchange only takes place in lung regions that are simultaneously ventilated and perfused, the availability of \dot{V}/\dot{Q} at bedside is likely to open up new possibilities to guide ventilation therapy.

2 Methods

We reevaluated data of a previous study [4]. After admission of the animal ethics committee (Uppsala University Hospital, Uppsala, Sweden), four healthy pigs were anesthetized and mechanically ventilated at positive end-expiratory pressures (PEEP) of 0 and 15 cmH₂O in supine position. EIT and SPECT measurements of both \dot{V} and \dot{Q} were performed at both PEEP levels. EIT was acquired using the EEK 2 (Draeger Medical GmbH, Germany) at a frame rate of 40 Hz. A bolus injection of saline (NaCl 10%, 10 ml) into the CVC was used to obtain \dot{Q} based on a previously described model-based approach [5]. SPECT was acquired using a dual-head gamma camera (Millenium, General Electric, USA). Krypton gas (^{81m}Kr) was used to assess \dot{V} , while Technetium-labeled macro-aggregated albumin (^{99m}Tc-MAA) served to obtain \dot{Q} . Imaging properties were analyzed by comparing pixel sums of rows (dorsal-ventral) and columns (right-left) of both EIT and SPECT images (see Figure 1). Furthermore, a correlation analysis

was performed to quantify image similarity.

3 Results

Analysis of imaging properties revealed a strong agreement between EIT and SPECT for both \dot{V} and \dot{Q} . However, imaging artefacts, such as central compression, are pronounced and most obvious in right-left direction (see Figure 1, right). Furthermore, ventral and dorsal shifts of EIT over SPECT were observed at both PEEP levels. At PEEP 0 cmH₂O, a dorsal shift was observed for \dot{V} , whereas \dot{Q} exhibits a ventral shift (see Figure 1, left). Correlation analysis revealed very strong ($r^2 = 0.94$ to 0.95) similarity for \dot{V} and \dot{Q} in dorsal-ventral direction at both PEEP levels. Moderate ($r^2 = 0.36$ to 0.46) and moderate to strong ($r^2 = 0.61$ to 0.82) similarity resulted for \dot{V} and \dot{Q} in right-left direction, respectively.

4 Conclusions

The results indicate that individual assessment of \dot{V} and \dot{Q} by EIT is possible. However, the dorsal shift of \dot{V} and the ventral shift of \dot{Q} introduce a position error that is different for both quantities. As a result, the spatial matching of \dot{V} and \dot{Q} cannot be ensured and a direct calculation of \dot{V}/\dot{Q} as a pixel-wise quotient will be erroneous. We thus suggest to investigate new algorithms for EIT reconstruction with a focus on low position error to enable \dot{V}/\dot{Q} by EIT.

5 Acknowledgements

We gratefully acknowledge funding (PU 219/2-1) by the German Research Foundation (DFG).

References

- [1] I Frerichs et al. *Thorax*, 72(1): 83–93, 2017
- [2] J B Borges et al. *Journal of Applied Physiology*, 112(1): 225–236, 2012
- [3] S Leonhardt, B Lachmann *Intensive Care Medicine*, 38(12): 1917–1929, 2012
- [4] H Luepschen et al. *44. Jahrestagung der DGBMT*, Rostock, Germany, Oct 2010
- [5] B Hentze et al. *39th Int. Conf. of the IEEE EMBC*, pp. 3596–3599, Seogwipo, South Korea, Jul 2017

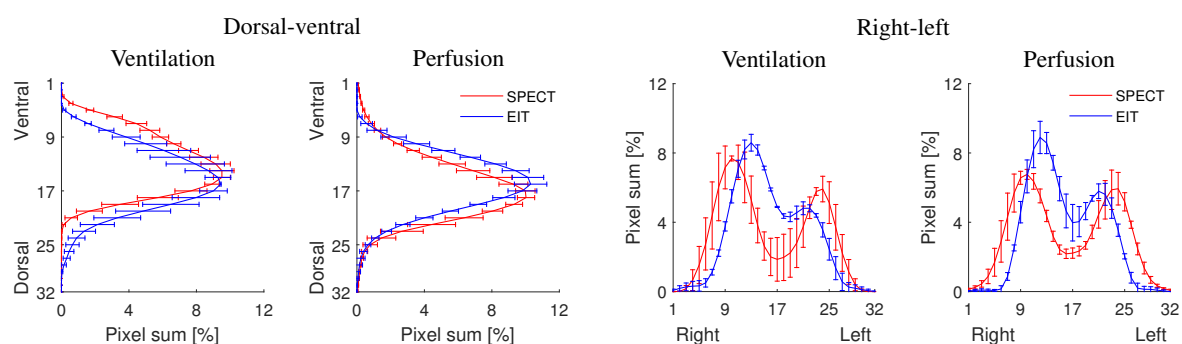


Figure 1: Analysis of imaging properties at PEEP 0 cmH₂O: Mean and standard deviation of the pixel sums in dorsal-ventral (left) and right-left (right) direction over all subjects are shown for both EIT (blue) and SPECT (red).

Deep D-bar for Absolute EIT Imaging: Experimental Results

Sarah J. Hamilton¹ and Andreas Hauptmann²

¹Marquette University, Milwaukee, WI, USA, sarah.hamilton@marquette.edu

²University College London, London, UK, a.hauptmann@ucl.ac.uk

Abstract: D-bar based reconstruction methods for EIT are robust to noise and modeling errors [3, 4] yet suffer blurring due to a low-pass filtering of nonlinear Fourier data. CNNs can learn the blurring present in reconstructions and provide effective post-processing for deblurring D-bar images. Results are presented for experimental data.

1 Introduction

In Electrical Impedance Tomography (EIT) the interior conductivity of a body Ω is recovered from surface electrical current/voltage measurements. While various reconstruction methods exist, here we focus on D-bar methods which are based on nonlinear Fourier transforms of the current/voltage data tailor-made for the EIT problem. The conductivity $\sigma \in \Omega$ is recovered by solving a $\bar{\partial}_k$ -equation in the transform variable k .

Deep learning methods have shown great promise for improving low quality or corrupted images. By viewing the blurred D-bar reconstructions as convolutions, we can train a Convolutional Neural Network (CNN) to undo the blurring inherent in low-pass filtered D-bar based images and use the trained network as a post-processing step.

2 Methods

In [1] we trained a CNN to deblur D-bar reconstructions from simulated noisy voltage/current data (continuum boundary conditions and known boundary shape). Here we remove potential biases from boundary shape, electrode locations, etc. completely by instead generating the training data from the non-physical Beltrami equation and using the ‘Shortcut D-bar Method’ [2]. For the training we generated conductivities $\sigma_n \in L^\infty(\Omega)$ and their corresponding low-pass D-bar reconstructions σ_n^{DB} as follows:

Step 1: Generate the Beltrami scattering data $\tau_n(k)$ for $\sigma_n(z)$ for $k \in \mathbb{C}$, $|k| \leq R$ as in [2]

$$\overline{\tau_n(k)} := \frac{1}{2\pi} \int_{\mathbb{R}^2} \bar{\partial}_z [M_{+\mu_n}(z, k) - M_{-\mu_n}(z, k)] dz_1 dz_2 \quad (1)$$

where $M_{\pm\mu_n}(z, k) = e^{-ikz} f_{\pm\mu_n}(z, k)$ are solutions to the Beltrami equation $\bar{\partial}_z f_{\pm\mu_n}(z, k) = \pm\mu_n(z) \bar{\partial}_z f_{\pm\mu_n}(z, k)$ satisfying $M_{\pm\mu}(z, k) = 1 + \mathcal{O}\left(\frac{1}{|z|}\right)$ for large $|z|$ and $\mu_n(z) = \frac{1-\sigma_n(z)}{1+\sigma_n(z)}$ denotes the Beltrami coefficient.

Step 2: Recover the low-pass D-bar reconstruction σ_n^{DB} by solving the Schrödinger $\bar{\partial}_k$ equation (see [5]) with scattering data $\mathbf{t}_n(k) = -4\pi i \bar{k} \tau_n(k)$.

Note that no electrode or boundary information is used in the training data as $\mu(z) = 0$ near $\partial\Omega$ (we require σ_n to be constant near the boundary, scaled to one). Pairs of simulated data $\{\sigma_n, \sigma_n^{\text{DB}}\}_n$ were then used as training data for the CNN. The trained network was then directly applied, with no transfer training required, to the D-bar reconstruction σ^{exp} for the experimental data. The D-bar image σ^{exp} was reconstructed from the measured current/voltage data Λ_σ using Step 2 above with scattering data \mathbf{t}^{exp}

$$\mathbf{t}^{\text{exp}}(k) = \int_{\partial\Omega} e^{i\bar{k}z} \left[\Lambda_\sigma \left(e^{ikz} \right) - ik\nu e^{ikz} \right] ds(z), \quad (2)$$

where $\nu = \nu(z)$ denotes the unit outward facing normal vector to the boundary, which can be computed numerically from a guess at the boundary shape function (see [3] for robustness to incorrect boundary shape and derivation of (2)). Preliminary results are shown in Figure 1.

3 Conclusions

Combining the power of CNNs with D-bar methods results in significantly sharper EIT reconstructions. No reliance on boundary shape or electrode locations was used nor noise included in the training data. Rather we sought to learn to undo the blurring inherent in D-bar. The methods developed here work with absolute and time-difference EIT in 2D. Further details will be given in the talk.

4 Acknowledgements

The experimental data was provided by the EIT lab at RPI [<https://www.ecse.rpi.edu/homepages/saulnier/eit/eit.html>], for which we express our thanks.

References

- [1] S. J. Hamilton and A. Hauptmann. *IEEE Trans. Med. Imaging*, doi: 10.1109/TMI.2018.2828303, 2018.
- [2] K. Astala, J.L. Mueller, L. Päiväranta, S. Siltanen. *Applied and Computational Harmonic Analysis*, 29(1):391-403, 2010.
- [3] S. J. Hamilton, J. L. Mueller, T. R. Santos. (under review) *arXiv preprint: 1712.00379*, 2017.
- [4] E. K. Murphy, J. L. Mueller. *IEEE Trans. on Med. Imag.*, 28(10):1576-1584, 2009.
- [5] K. Knudsen, M. Lassas, J.L. Mueller, S. Siltanen. *Inverse Problems and Imaging*, 3(4):599-624, 2009.

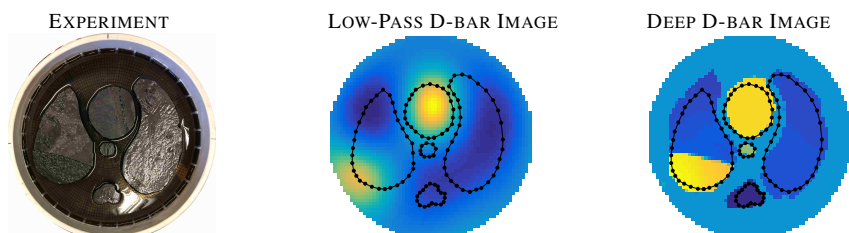


Figure 1: Demonstration of absolute imaging with the Deep D-bar method on experimental data from the ACT4 system with agar/graphite targets. The heart/aorta are more, and lungs/spine less, conductive than the background. The right (DICOM) lung contains an injury with conductivity matching the heart. No simulations of current/voltage data were required for any step of the process. The *Structural SIMilarity (SSIM)* index increased from 0.5176 (D-bar) to 0.6963 (Deep D-bar).

Comparing D-bar and Regularization-based reconstruction

Andy Adler¹, Sarah Hamilton², William RB Lionheart³

¹Carleton University, Ottawa, Canada, ²Marquette University, Milwaukee, USA, ³University of Manchester, UK

Abstract: EIT reconstruction algorithms based on D-bar methods offer various advantages. One limitation to wider use of these algorithms has been a lack of comparisons of algorithm performance on reconstruction metrics. We show some initial results comparing D-bar and regularization-based reconstructions for phantom data.

1 Introduction

Reconstruction of EIT images is a challenging non-linear problem which needs to overcome the poor sensitivity to changes at depth. Over the years, many EIT reconstruction algorithms have been proposed for 2D and 3D geometries, and for difference and absolute reconstructions.

One relatively novel approach to image reconstruction is D-bar, a non-iterative absolute approach [2]. The D-bar literature is rich, but there is little direct comparison of performance to traditional (iterative, regularized) approaches. Comparison of algorithms is challenging, because there are multiple comparison criteria: resolution, ability to suppress noise, ability to maintain sharp edges, resistance to electrode movement and other artefacts.

Our goal is to present initial results comparing D-bar with two popular regularized algorithms, iterative Gauss-Newton (with a smoothing prior) and GREIT [1], all for reconstruction of difference images with small contrasts.

2 Results and Discussion

Two simulation phantoms were used, shown in fig. 1. One is a shape – “Pac-Man” – with sharp edges and holes, while the other moves a small target from centre to the side. Small ($0.1 \times$ background) contrasts were used. All algorithms were set to calculate difference 32×32 pixel EIT images assuming a circular 2D body with 32 equally spaced electrodes of the indicated width. Stimulation patterns were “skip 4” with monopolar voltage measurements on all electrodes (including driven ones).

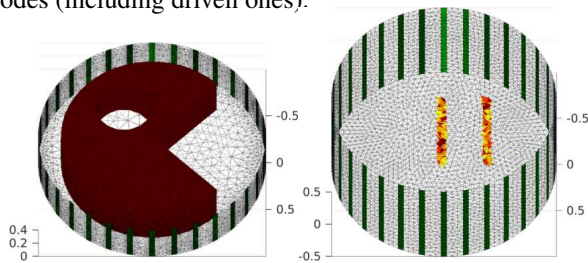


Figure 1: Phantoms: “Pac-Man” shape, and point targets

Most algorithms have parameters to control the trade-off between resolution and noise performance. D-bar uses a radius (r), GN uses a hyperparameter (λ) and GREIT uses a noise figure (NF). We wanted to first select parameters which for which the noise performance is equal, and then subsequently evaluate other characteristics. Fig. 2 reconstructs the phantom with added Gaussian noise for comparison of parameter settings. We observe that D-bar shows a different pattern (lower spatial frequency) for the reconstructed noise compared GN and GREIT.

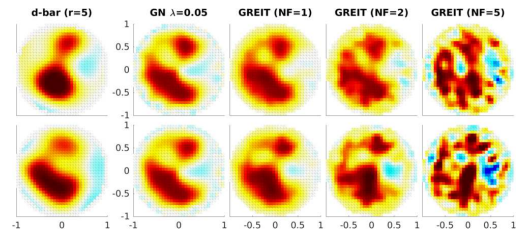


Figure 2: Reconstructions of data with added Gaussian noise (noise sample per row) for algorithms and parameter settings.

Next, we analysed the “point spread function” versus radial position (fig. 3). D-bar has more uniform resolution, compared to improving resolution near the boundary.

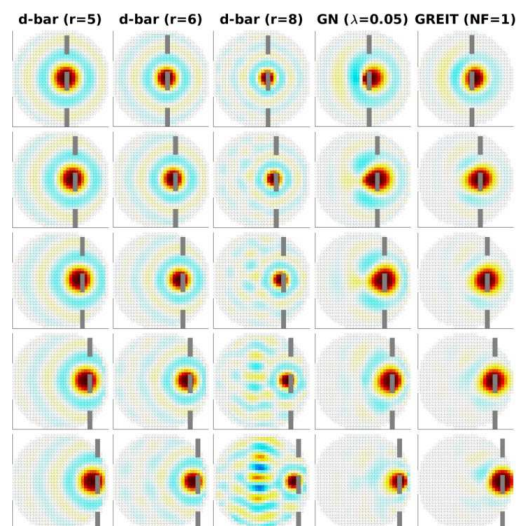


Figure 3: Reconstructions of points (at grey dotted line)

Last, we explore the ability to reconstruct difference images where electrodes move between measurements. Here the right centre electrode moves by the indicated amount (in degrees). Results show D-bar is least affected.

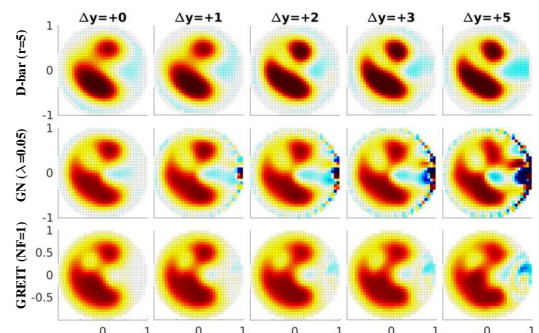


Figure 4: Reconstructions of moving electrode near “mouth”

Our results show that D-bar: 1) has position invariant point-spread function, 2) projects noise into images very differently, and 3) appears much less sensitive to electrode position errors than regularized reconstructions. There is clearly plenty of work needed to understand these effects.

References

- [1] A Adler *et al*, *Physiol Meas*, 30:S35–S55, 2009
- [2] Isaacson *et al*, *IEEE TMI*, 23:7, 821–828 2004.

Using Statistical Methods for Image Reconstruction in Structural Objects

Tomasz Rymarczyk^{1,2}, Edward Kozłowski³

¹ Research and Development Center, Netrix S.A., Lublin, Poland e-mail: tomasz@rymarczyk.com

² University of Economics and Innovation in Lublin, Lublin, Poland

³ Lublin University of Technology, Lublin, Poland

Abstract: The method presented in paper allows us to produce accurate baseline prediction of conductivity for image reconstruction. The statistical algorithms enable us to estimate the adequate parameters for linear models, that describe the linear dependences between conductivities and measurements of voltage on the electrodes.

1 Introduction

The highly correlated predictors with each other's in linear models do not allow to determine the precisely influences of these predictors on the output variable. Directly application the least square method to estimate the unknown parameters may lead to a poor prediction. Dampness in structural objects such as walls is a serious problem in the construction industry. The traditional techniques used to deal with this kind of problem show, to be ineffective, justifying the need to find a new approach [1-3].

2 Algorithm

Let us consider the system of state equations where $Y \in \mathbb{R}^n$, $X \in \mathbb{R}^{n \times k}$ denote the observation matrices of response and input variables respectively, $\beta \in \mathbb{R}^k$ denotes the vector of unknown parameters. Sometimes by applying the algorithm of predictor selection we may obtain the variables which are linearly dependent. Then after estimating the unknown parameters β in linear model we observe the large absolute values of parameters for collinear variables. The obtained model does not have a prediction accuracy. Whereas the application LASSO, Elastic net, LAR methods allows us to shrink the coefficients β toward 0. The shrinkage of coefficients often improves the prediction accuracy

The following algorithm has been proposed:

1. Using the location and scale transformation we standardize all predictors. The intercept in expression () is equal a mean of response variable. Additionally, we put that the active set (set of predictors) is empty, $\beta_1 = \beta_2 = \dots = \beta_k = 0$. At the beginning the sequence of residuals $\{\varepsilon_i\}_{1 \leq i \leq n}$ is equivalent to sequence of response variable $\{y_i\}_{1 \leq i \leq n}$, ie. $\varepsilon_i = y_i$ for $1 \leq i \leq n$.
2. Calculate the residuals for the linear model with all predictors from active set. Determine the predictor X_j , $1 \leq j \leq k$ (which is not in active set) most correlated with residuals and attach to the active set.
3. Move coefficient β_j from 0 towards its least-squares coefficient $\langle X_j, \varepsilon \rangle$, until some other competitor X_s (which belong to active set) has a much correlation with the current residuals as does X_j .
4. Move β_j and β_s in the direction defined by their joint least square coefficient of the current residual on

(X_j, X_s) , until some other competitor X_l from active set has a much correlation with the current residual.

5. Go to step 2 and continue in this way until all k predictors have been entered.

3 Results

The image reconstructions were made on the testing set $\tilde{\Omega} = \{\tilde{Y}, \tilde{X}\}$, $\tilde{Y} = \text{col}(\tilde{Y}_i)$, $\tilde{X} = \text{col}(\tilde{X}_i)$ for $1 \leq i \leq n_2$.

The picture 1a presents the randomly chosen dampness of the block corresponding to the conductivity vector \tilde{Y}_i , from the testing set, whereas the picture 1b shows the reconstructions $\hat{Y}_i = (\tilde{X}_i - \bar{x})\hat{\beta} + \bar{y}$ based on the measurements \tilde{X}_i .

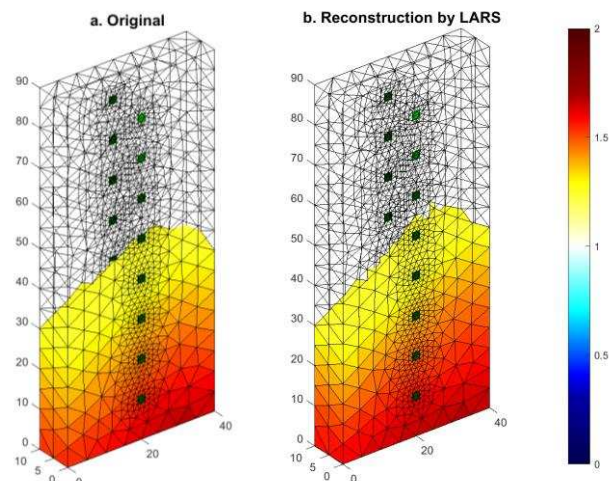


Figure 1: The damp of block and reconstruction based on the voltage on the electrodes.

4 Conclusion

In this paper, there were proposed algorithms based on statistical methods for the purpose of more accurate and stable reconstruction results in solving EIT inverse problem. The presented algorithm determines the moisture of the test model. These methods will be applied very successfully in many areas of the scientific modelling.

References

- [1] Hoła J., Matkowski Z., Schabowicz K., Sikora J., Nita K. and Wójtowicz S.: *Identification of Moisture Content in Brick Walls by means of Impedance Tomography*, COMPEL, Vol. 31, Issue 6, pp. 1774-1792, 2012
- [2] James G., Witten D., Hastie T., Tibshirani R.: *An Introduction to Statistical Learning with Applications in R*, Springer, New York, 2013.
- [3] Rymarczyk T., *New Methods to Determine Moisture Areas by Electrical Impedance Tomography*, International Journal of Applied Electromagnetics and Mechanics, vol. 37, Issue 1-2, pp.79-87, 2016.

Passive Electric Impedance Tomography

Evgeny Tsizin¹, Alex Bronstein^{1,2}, Talma Hendler^{1,3} and Mordekhay Medvedovsky³

¹School of Electrical Engineering, Tel Aviv University

²Department of Computer Science, Technion – Israel Institute of Technology

³Center for Brain Functions, Tel Aviv Sourasky Medical Center

Abstract: We introduce an electric impedance tomography modality without any active current injection. By loading the probe electrodes with a time-varying network of impedances, the proposed technique exploits electrical fields existing in the medium due to biological activity or EM interference from the environment or an implantable device. A phantom validation of the technique is presented.

1 Introduction

The aim of the Electrical Impedance Tomography (EIT) is to deduce the spatial distribution of electrical impedance in a region of interest (ROI) enclosed by electrodes. The measurements consist of the potential created on the electrodes as a response to current injection from each electrode, which are expressed concisely as a pairwise impedance matrix. An inverse problem is then solved to infer the properties of the medium [2].

Here we introduce a novel technique for electrical impedance monitoring in which the pairwise impedance matrix of the electrodes is deduced from the voltage response to the loading of electrical fields existing in the medium by means of a time-varying network of impedances switched at a high frequency. The existing fields may result from biological activity (such as EEG, ECG or EMG), power line electrical noise, or from the communication signal of an implantable device. The potential advantages of the proposed passive EIT technique include reduced power consumption due to the absence of active current injection, reduced sensitivity to electromagnetic interferences, decreased nonlinear effects, and the possibility to monitor the bio-impedance change on the frequencies overlaying with the spectrum of the electrophysiological signals while measuring these signals [2, 3]. All these properties are important especially for wearable and implantable devices.

2 Theory and results

We assume a nonzero electrical potential vector \mathbf{V}_0 is measured in a conductive medium by means of a passive system of N electrodes characterized by the unknown $N \times N$ pairwise impedance matrix \mathbf{Z} (each z_{ij} measuring the impedance between the electrodes i and j). When the electrodes are loaded by a passive impedance network whose pairwise impedance matrix is \mathbf{Z}_L , the following relation holds between the voltages \mathbf{V} and currents \mathbf{I} on the electrodes

$$\mathbf{V} = \mathbf{Z}_L \mathbf{I} \quad \mathbf{V}_0 - \mathbf{V} = \mathbf{Z} \mathbf{I} \quad (1)$$

Given M measurements \mathbf{V}_i , $i=1, \dots, M$, each corresponding to loading by an invertible matrix $\mathbf{Z}_L[i]$, the following linear system can be solved for \mathbf{Z}

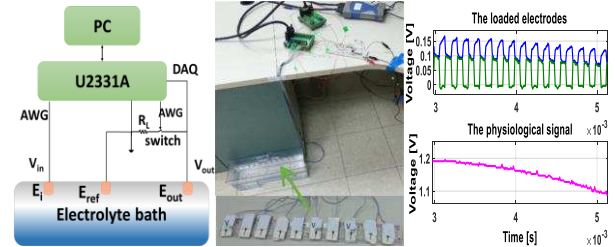


Figure 1: Left-to-right: a schematic diagram of the phantom for the passive EIT, its physical implementation and experimental validation.

$$(\mathbf{V}_0 - \mathbf{V}_1, \dots, \mathbf{V}_0 - \mathbf{V}_M) = \mathbf{Z}(\mathbf{Z}_L^{-1}[1]\mathbf{V}_i, \dots, \mathbf{Z}_L^{-1}[M]\mathbf{V}_i). \quad (2)$$

The load switching frequency should be fast enough to consider \mathbf{V}_0 constant during a single loading period (about 10kHz for the biological signals and in our experimental validation). In such a case \mathbf{V}_0 is the voltage measured on the electrodes for the unloaded periods, while \mathbf{V}_i are for the loaded ones. For multi-frequency excitation the values in (1) can be considered phasors [1]. If the signal is much faster than the switching frequency (e.g. communication signal of the implantable device) the values in (1) is voltage power averaged over the switching period (RMS).

Our experimental setup for the validation of the passive EIT technique comprised a saline bath with an immersed electrode array (Fig. 1). The slow "physiological" signal induced in the bath was periodically loaded on the electrodes through the analogue switch by resistors (Fig. 1). Comparing the voltages on electrodes during the loaded and unloaded periods allowed to passively determine the conductivity of the saline solution.

Conclusions

We introduced the theory and experimentally validated a passive EIT technique. In contrast to active EIT, our technique works with low current density on electrodes, which in turn reduces nonlinear effects on the tissue/electrode interfaces and the amount of current injected into tissues, and its power is harvested from the biological activation or noise. The spectrum of potential applications ranges from seizure onset sensing and myocardial ischemia detection to human-machine interfaces.

References

- [1] Desoer, Charles A. Basic circuit theory. Tata McGraw-Hill Education, 2009.
- [2] DS Holder *Electrical Impedance Tomography* IOP Publishing: Bristol, 2005
- [3] Aristovich, Kirill Y., Brett C. Packham, Hwan Koo, Gustavo Sato dos Santos, Andy McEvoy, and David S. Holder. *NeuroImage* 124 (2016): 204-213.

Electric and Magnetic Field Distributions in Deep Brain Stimulation

Neeta Ashok Kumar, Munish Chauhan, and Rosalind Sadleir

School of Biological and Health Systems Engineering, Arizona State University, AZ, USA. Rosalind.Sadleir@asu.edu

Abstract: Deep Brain Stimulation (DBS) electric and magnetic fields were mapped using MREIT. In-house carbon electrodes were fabricated to address challenges in using traditional DBS electrodes in an MRI environment. Reduced susceptibility artifacts with equivalent electric fields were achieved using carbon electrodes.

1 Introduction

Neuromodulation techniques such as Deep Brain Stimulation (DBS) apply electric fields to regulate abnormal neural activity involved in Parkinson's disease [1]. DBS currents are typically applied via Pt-Ir electrodes (e.g. Medtronic DBS 3387/3389 lead) implanted in the brain to a neurostimulator body within the subcutaneous pectoral area. The spatio-temporal localization of electrical stimulation induced changes in neural activity is critical to understand mechanisms underlying DBS. An MR-based impedance imaging technique, Functional Magnetic Resonance Electrical Impedance Tomography (fMREIT), is being developed to spatially map the activation and inactivation of neural centers on the timescale of neural activity.

Challenges such as field inhomogeneities and joule heating are inherent in the MRI use of Pt-Ir ($\chi_{Pt-Ir} = 230$ ppm, $\sigma_{Pt-Ir} = 4 \times 10^6 \text{ S/m}$) [2]. Effects increase with MR field strength and faster imaging sequences (e.g. Gradient echo). We fabricated carbon electrodes ($\chi_{Carbon} = -26.11$ ppm, $\sigma_{Carbon} = 1 \times 10^3 \text{ S/m}$) [2] for better MRI-compatibility. Electric and magnetic field distributions produced by carbon and size-matched Pt/Ir electrodes were mapped in isotropic and anisotropic phantoms.

2 Methods

Electrodes - In-house carbon electrodes (500/270 μm diameter one-contact, 1C; 1200 x 500 μm^2 two-contact, 2C) were prepared with insulative coatings (Nafion in Isopropanol, Polyvinylidene Fluoride in acetone) surrounding conductive carbon fibers.

Experimental setup - Size-matched carbon (1C and 2C) and Pt-Ir electrodes (Pt-Ir wire; 3389 DBS lead) were imaged together in isotropic gel phantoms (5.2g/L NaCl, 20g/L Agar, 50g/L Gelatin; conductivity, $\sigma = 0.29 \text{ S/m}$ at 1 kHz). DBS-style current was injected between each of these electrodes to an external ground. Additionally, 1-C carbon/ground electrodes were used in a formalin-fixed rodent head. All images were obtained using a Bruker Biospec 7T preclinical MRI system at the Barrow Neurological Institute (Phoenix, AZ).

MREIT Imaging Parameters: Spin echo (SE) and gradient echo (GE) MREIT [3] sequences were employed. Scan parameters were SE-MREIT: FOV: 60 x 60 mm^2 (40 x 40 mm^2 for anisotropic phantoms), Matrix size = 128 x 128, TR/TE = 1000/20 ms, Slice thickness = 3 mm, Averages = 4. ± 1 mA current injection pairs were applied

for 10 ms each after 90° and 180° pulses respectively. GE-MREIT: Same as SE-MREIT except TR/TE = 500/10 ms.

Processing: Susceptibility artifacts associated with carbon and Pt/Ir electrodes were assessed by computing ratios of full-width half-maximum (FWHM) apparent size on magnitude images to actual electrode sizes. Complex MR data was processed to magnetic flux density (B_z) [3] and projected current density (J^P) magnitude [4] distributions. Current density magnitude images of uniform phantoms (J^0) were compared with J^P .

3 Results

Artifacts around carbon electrodes (2C:1.34x) were smaller than around Pt/Ir electrodes (DBS:2.34x). Complete and partial B_z dipoles were observed around source carbon and Pt/Ir electrodes respectively. The scales of B_z and J^P distributions were similar for size-matched 2C/DBS electrodes (Fig. 1(a,b)). J^P surrounding the cylindrical DBS lead was symmetric whereas rectangular 2C electrode was asymmetric. The smaller volume (3.15x) of the anisotropic phantom (Fig. 1(d)) compared to isotropic phantoms (Fig. 1(a,b,c)) led to larger B_z and J^P scales.

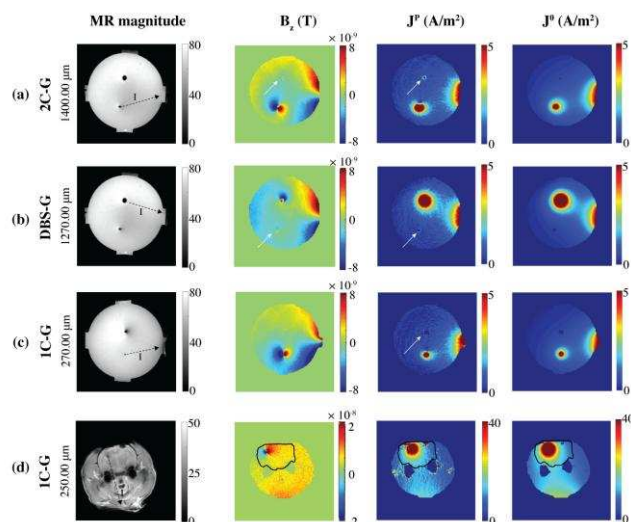


Figure 1: Current injected in isotropic gel phantoms (a-c) and anisotropic rodent head (d) 1C-G. MR magnitude, B_z , J^P and J^0 distributions are shown for each sample.

4 Conclusions

MR susceptibility artifacts surrounding carbon electrodes were smaller than their Pt/Ir analogs without compromising the efficiency of current injection. Simulated and experimental current density distributions agreed for both isotropic and anisotropic phantoms.

References

- [1] EB Montgomery, JT Gale *Neurosci Biobehav Rev*, 32:388-407, 2008
- [2] J Matthey, H Garden *The PGM Database*, 2017
- [3] RJ Sadleir *Physiol Meas*, 27:S261-70, 2006
- [4] C Park *PhysMed Biol*, 52:3001-13, 2007

Classification Applied to Brain Haemorrhage Detection: Initial Phantom Studies using Electrical Impedance Measurements

Barry McDermott¹, Martin O'Halloran¹, Adam Santorelli¹, Brian McGinley¹ and Emily Porter¹

¹Translational Medical Device Lab, National University of Ireland, Galway, b.mcdermott3@nuigalway.ie

Abstract: Machine learning and classification algorithms are applied to data collected from an EIT system. The system is used with an anatomically accurate head phantom setup in a variety of situations modelling normal and haemorrhagic brain. This initial study demonstrates the promise of classification, but also indicates challenges.

1 Introduction

EIT has traditionally shown most success when applied to situations featuring changes in time such as lung function monitoring [1]. Static or quasi-static lesions such as established brain haemorrhage have conversely proved challenging to detect using EIT [2]. Machine learning approaches have shown potential in tackling such cases with related diagnostic modalities such as microwave imaging [3] but have not to date been studied in depth in the EIT sphere.

In this study an anatomically accurate two layer head phantom was developed along with a range of phantom bleeds, varying in size and shape. A 16 electrode ring was placed around the head and connected to a Swisstom Pioneer EIT system. EIT data measurement frames were recorded for a wide variety of test scenarios differing in ring orientation, bleed size and bleed location. These frames were labelled as 'normal' or 'bleed'. This data was then divided and used to train and test classifiers to differentiate between the two cases. Linear support vector machines (SVMs) in particular showed good performance, thus sample results from this classifier are presented here.

2 Methods

A two layer head phantom was developed with an outer layer modelling aggregate scalp, skull and cerebrospinal fluid, constructed from a graphite, carbon black and polyurethane composite. This composite emulated the conductivity of this layer. Another composite based on these materials was used to produce phantom bleeds, modelled as spheres and rectangular cuboids of volume 6 ml to 36 ml. The conductivity of the brain compartment of the head phantom was modelled using saline. A ring of 16 EEG electrodes was placed around the head and connected to the Swisstom Pioneer. In total 216 different abnormal test scenarios were captured as EIT measurement sets differing in bleed size (4 sizes), location (9 locations) and ring position (6 ring orientations). A sample setup is shown in Fig. 1. An equal number of corresponding normal (healthy) scenarios were captured. These frames were divided in a variety of ways and used to train and test a range of classifiers. Linear SVMs appeared to perform best with some sample results shown from this classifier type shown in Table 1. A True Positive (TP) is where a bleed is detected and is truly present. A

True Negative (TN) is where normal is detected and is truly the case.

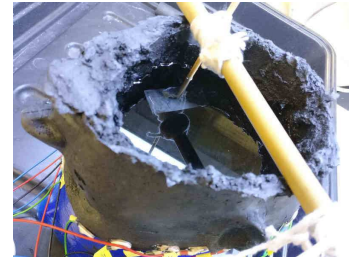


Figure 1: This example of a typical test setup shows a rectangular cuboid bleed suspended into the saline brain layer of the head phantom.

	TP %	TN %
Train on all Rings (1-6)	84 %	95 %
Half Ring 3 Withheld	72 %	100 %
Half Ring 1 Withheld	75 %	100 %
Ring 1 Withheld	75 %	86 %
Ring 2 Withheld	0 %	100 %

Table 1: True Positive & True Negative % for linear SVM Classifier. Sample results are those from testing on withheld data (and training on all the rest); except for the first row which is the performance when trained with cross validation on all of the data (none withheld).

3 Conclusions

The results of this initial phantom study show that classification may help in applying EIT techniques to static or quasi-static situations such as detection of an established bleed. The classifier works well when the ring layout(s) used in test data match those in training data. However, introducing test data from an unseen ring can result in significantly poorer performance. Improved data processing as well as training on a significantly higher number of test cases (i.e. differing heads) should improve performance and help make the technology valuable clinically.

4 Acknowledgements

The research leading to these results has received funding from the European Research Council under the European Union's Horizon 2020 Programme/ ERC Grant Agreement BioElecPro n.637780, and from the Hardiman Research Scholarship, NUIG.

References

- [1] A Adler, A Boyle, *IEEE Transactions on Biomedical Engineering* 64(11):2494-2504,2017
- [2] A Romsauerova, A McEwan, L Horesch, *Physiological Measurement* 27(5):S147-S161,2006
- [3] M Persson, A Fhager, H Trefna et al., *IEEE Transactions on Biomedical Engineering* 61(11):2806-2817,2014

In Vivo Estimation of the Head Tissue Conductivities

Taweechai Ouypornkochagorn

Faculty of Engineering, Srinakharinwirot University, Thailand, taweechai@g.swu.ac.th

Abstract: The scalp (σ_{scalp}), skull (σ_{skull}), cerebral spinal fluid (CSF, σ_{CSF}), grey matter (GM, σ_{GM}) and white matter (WM, σ_{WM}) conductivities are determined from Electrical Impedance Tomography (EIT). Gauss-Newton (GN) with bound constrained optimisation was used. Our estimations of them are 0.60 S/m, 0.010 S/m, 1.36 S/m, 0.30 S/m, and 0.22 S/m respectively.

1 Introduction

Many studies have reported values of head tissue conductivities by using an in vivo estimation method [1-4]. However, all of them can only estimate σ_{scalp} and σ_{skull} due to the very low sensitivity of boundary voltages (V) to conductivity perturbation of the tissues inside skull. Including σ_{CSF} , σ_{GM} , σ_{WM} in the estimation may result unexpected negative values. For example, [2] estimated σ_{scalp} , σ_{skull} and the brain conductivity resulting large negative conductivities by 44-56% of the subjects. To deal with this negative-value problem, [5] proposed to constrain the estimation to be always positive by transforming σ to γ with a logistic function

$$\sigma = p + \frac{t-p}{1+e^{-\gamma/\kappa}} \text{ or } \gamma = -\kappa \log\left(\frac{t-p}{\sigma-p} - 1\right), \quad (1)$$

where t is the upper bound, p is the lower bound, and κ is the relaxation factor. The sensitivity matrix in the γ domain (∂G) computes by

$$\partial_{\gamma} G(\gamma) = \partial_{\sigma} U(\sigma)(\sigma-p)(t-\sigma)(t-p)^{-1}\kappa^{-1}, \quad (2)$$

where U is the known modeling function of σ , and then G is now that of γ . ∂U is the 5-parameter sensitivity matrix of σ domain. Thus the forward computation is now

$$V = G(\gamma) + e, \quad (3)$$

where e is noise, and the estimation is now based on

$$\hat{\gamma} = \arg \min_{\gamma} \left\{ \|V - G(\gamma)\|^2 \right\}. \quad (4)$$

Finally, $\hat{\sigma}$ can be computed for $\hat{\gamma}$, i.e. the estimated conductivity in σ domain, by (1).

2 Methods

A trial, approved by NHS RECs and MHRA, was carried out on a healthy subject. The EIT measurement was performed by fEITER machine [6], complying with IEC60601, on 32 electrodes. 1 mA_{peak-peak} 10kHz excitation current was injected in 20 diametric directions, and 509 adjacent measurements were collected with a speed of 100 fps. The measurement data over 12 s were averaged to reduce influences of noise. A subject head model containing 178,480 elements was used, where the geometry of the attached electrodes were included. GN method without constraint (the conventional method) and GN with constraint (the constrained method) were used, with 20 iterations and the regularization parameter of 1×10^{-4} . The lower and the upper bounds were 0 S/m and 2 S/m respectively. The relaxation factor was set to 1. Three

initial guesses of all conductivities were randomly selected. The contact impedance of the electrodes was set to 1,200 Ω .

3 Results

The estimation results and the errors are shown in Table 1 and Fig. 1 respectively. The reported conductivities are also presented in the last column of Table 1. Obviously, the estimates obtained from the constrained method are much more consistent to the reported conductivities than those of the conventional method where some negative values occurred. The standard deviations of those of the constrained method are also much lower than those of the conventional method by the average of 193 times. The estimation errors of the constrained method are significantly lower and more robust to the change of initial guesses as well.

Table 1: The estimated σ (S/m)¹

σ	Conventional method (S/m)	Constrained method(S/m)	Reported Conductivities(S/m)
σ_{scalp}	1.96±2.02	0.60±0.02	0.33[1], 0.32[2], 0.58[3], 0.4[4]
σ_{skull}	0.374±0.633	0.010±0.001	0.008[1], 0.016[2], 0.008[3], 0.005[4]
σ_{CSF}	8.86±9.73	1.36±0.43	1.456 [7]
σ_{GM}	-3.33±4.74	0.30±0.08	0.28 [8]
σ_{WM}	0.99±1.72	0.22±0.02	0.26 [9]

¹The presented values are in the format of mean±standard deviation.

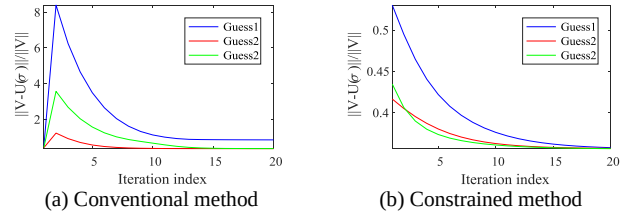


Figure 1: Estimation errors.

4 Conclusions

Constrained method can effectively estimate the conductivity of the five head tissues with plausible consistency to the reported conductivities obtained from different methods. It is also robust to the selection of initial guesses as well.

References

- [1] Gonçalves, S. I., et al. *IEEE transactions on Biomedical Engineering*, 50(6):754-767, 2003.
- [2] Baysal, U and Hauelsen *J Physiol. Meas.*, 25:737-748, 2004.
- [3] Ouypornkochagorn, T, McCann, H, Polydorides, N, *Conf 15th EIT2014*, Ontario, Canada, 2014.
- [4] Fernández-Corazza, M, et al. *IFMBE Proceeding*, 54(5):5-8, 2016.
- [5] Polydorides, N and Ouypornkochagorn, T, *Conf 15th EIT2014*, Ontario, Canada, 2014.
- [6] McCann, H, et al., *Conf EMBS2011*, Boston, USA, 2011.
- [7] Baumann, S. B, *IEEE transactions on biomedical engineering*, 44(3): 220-223, 1997.
- [8] Latikka, J., T. *Phys. Med. Biol.*, 46: 1611–1616, 20

Impedance Change due to Ion Channel Opening in Muscle as a Potential Robust Means for Controlling Bionic Prostheses

Leonardo Fiuza¹, James Avery¹, David Holder¹, and Kirill Aristovich¹

¹Department of Medical Physics and Biomedical Engineering, University College London, UK,
l.fiuza.17@ucl.ac.uk

Abstract: A novel approach was developed for detecting functional muscle activity using EIT and surface ECG electrodes placed on the forearm. The method shows average real-time SNR of 5, which is free from motion and geometry-related artefacts and allows real-time control of prosthetic arm.

1 Introduction

Control of prosthetic devices may be achieved using surface EMG. Unfortunately, the signal is contaminated by crosstalk, which makes it difficult to separate signals from different muscles. EIT could be used as an input signal by imaging muscle shape changes or density with recording with 10-60 surface electrodes at around 50 kHz [1,2] but this was limited by artefacts from motion and external shape changes. We propose a novel approach in which ion channel opening, rather than muscle bulk, is recorded by extension of the approach of fast neural EIT [3]. In this, impedance decreases with neuronal depolarization, with optimal changes at 1.7 and 6 kHz for cerebral cortex and nerve respectively. As muscle activation is accompanied by ion channel opening, we propose that this could provide a more accurate method as input for prosthesis control.

The purpose of this work was to demonstrate the feasibility of using EIT measurements of functional spontaneous muscular activity as control signals for prosthetics. Questions were: 1) What is the SNR and optimal frequency? 2) Is the approach likely to yield sufficient independent measures to anticipate control of prosthetic arm?

2 Methods

4 conventional ECG Ag/AgCl/Solid adhesive pregelled electrodes were placed 7cm apart on the volar mid-forearm in 3 subjects. 4 electrode impedance changes (dZ) were recorded during wrist flexion to 70° using 20 sinusoidal currents between 100 Hz and 10 kHz at 10 current levels from 50 to 500 μ A. EMG signals were recorded simultaneously with low-pass filter f_c 80 Hz. dZ was extracted by demodulation around the carrier frequency with a bandwidth of 100 Hz (lowered for lower frequencies), and high-pass filtered at 30 Hz to remove geometry and motion artefact-related changes.

3 Results

Reproducible significant ($P < 0.001$) dZ with peak SNR of 5 ± 0.5 occurred during wrist flexion, over 500-2000Hz with a peak at 1.2kHz. Filtered dZ correlated with EMG as well as RMS dZ correlated with RMS EMG ($P < 0.001$, Fig.1, $n=270$ in 3 subjects). The relaxed muscle motion resulted in EMG-uncorrelated non-significant dZ changes ($P > 0.5$).

4 Discussion

This study suggests, for the first time, that there is an impedance change associated with muscle depolarization which is equivalent to the surface recorded EMG. Improved resolution with surface recording for prosthetics could in theory be achieved with imaging either by EIT or inverse source modelling of the EMG, or machine learning applied to either approach. However, EIT has the advantages that there are more independent measures for the number of electrodes, and the inverse solution is in principle unique. The range of usable frequencies (500-2000 Hz) suggests that real-time frequency division multiplexing approach (FDM-EIT) will be the most suitable for real-time control of the prosthetic device.

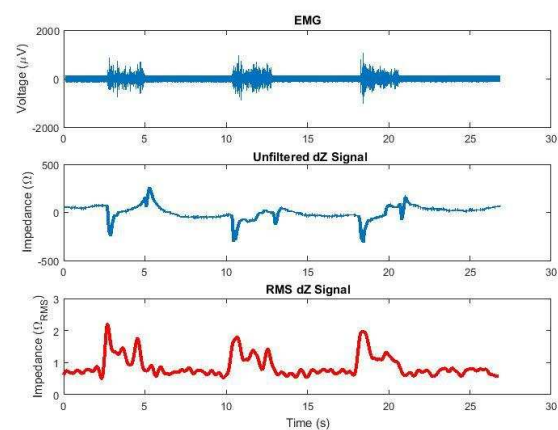


Figure 1: Typical Example of the real-time measurement. Top: EMG signal with increased RMS during muscle contraction. Middle: Unfiltered dZ contaminated with motion and shape change-related artefacts, Bottom: RMS of high-pass filtered dZ representing functional muscle activity.

Work in progress is to record dZ simultaneously using frequency division multiplexing EIT with 6 frequencies with the greatest SNR using two 6 electrode rings around the mid-forearm 7 cm apart. This yields total of 66 linearly independent measurements. The RMS dZ signals will be used for a pre-trained machine learning kernel (SVM) to compute outputs for 5 DC and 1 stepper motor of the OpenBionics 3D-printed arm prosthesis [4]. Theoretically this paradigm is suitable for a linear control strategy using 25 independent parameters, which should result in precise force-finger motion control.

References

- [1] Yang Zhang Robert Xiao Chris Harrison, ISBN 978-1-4503-4189-9/16/10
- [2] Seward B. Rutkove: Muscle Nerve. 2009 Dec; 40(6): 936–946.
- [3] KY Aristovich, BC Packham, H Koo, GS dos Santos, A McEvoy, DS Holder NeuroImage 124, 204-213
- [4] <https://www.openbionics.com>

Electrode drive and measurement patterns for EIT of neural activity in peripheral nerve

James Hope^{1,2} and F. Vanholsbeeck², A. McDaid¹

¹Department of Mechanical Engineering, The University of Auckland, NZ, jhop030@aucklanduni.ac.nz

²Dodd Walls Centre, The Department of Physics, The University of Auckland, NZ

Abstract: The performance of six EIT drive and measurement electrode patterns have been investigated and compared using a finite element (FE) model of a nerve cuff, with dual-ring electrode array, implemented on a three fascicle peripheral nerve. Unique and non-unique solutions were observed due to anisotropy in the nerve tissue.

1 Introduction

Physical alignment of nerve fibres in a peripheral nerve produces higher conductivity in the longitudinal axis, aligned parallel to the fibre length direction. In EIT, anisotropic anomalies can produce boundary voltage data with non-unique solution, although, the use of numerical modelling techniques with some *a-priori* information can circumvent this problem [1]. Previous studies on EIT imaging of neural activity in peripheral nerve [2, 3] have used a single-ring electrode configuration with drive current on the transverse plane, perpendicular to the longitudinal axis, thus largely eliminating the influence of tissue anisotropy. An electrode configuration which utilises the longitudinal axis offers the benefit of a larger fraction change in impedance during neural activity but may not provide a unique solution due to anisotropy in the active neural tissues. Here, we present results of a simulation study in which we aim to resolve fascicle level neural activity in peripheral nerve using longitudinal current electrode patterns.

2 Methods

2.1 Drive and measurement patterns

We considered a total of six electrode drive and measurement patterns; four patterns utilised longitudinal current by passing current between two rings, spaced 10 mm apart, on a 2x16 dual-ring electrode configuration; two patterns utilised a transverse current within a 1x16 single-ring electrode configuration. Longitudinal current drive-electrode pairs were on different rings and either ‘Opposing’, i.e. an angular offset of 180 degrees, or ‘In-line’, i.e. an angular offset of 0 degrees. Longitudinal current measurement electrode pairs were either ‘Opposing’ or ‘In-line’, defined in the same way as above, and taken as differential measurements. Transverse current drive and measurement electrode pairs were on the same electrode ring and were either ‘Adjacent’ or ‘Opposing’.

2.2 FE Model

The forward EIT problem used a cylindrical 4-layer shell model of a single fascicle nerve with the intra-fascicle volume divided into a grid of 50 sub-volumes, whereas the inverse EIT problem contained 3 fascicles, see Ref [4]. Both models were implemented in COMSOL 5.3.

2.3 Performance criteria

Electrode patterns were compared using three criteria: 1) analysis of the singular values from singular value decomposition of the sensitivity matrix (Fig 1a); 2) the signal to error ratio:

$$SER = 20 \log(v_\sigma/v_e) \quad (1)$$

where v_σ is the standard deviation of the normalised differential boundary voltage measurements and v_e is the normalised maximum possible voltage error from noise and hardware errors (Fig 1b); and 3) qualitative analysis of the reconstructed conductivity (Fig 1c).

3 Results and Conclusions

Transverse current patterns produced higher singular values but also significantly poorer SER’s at central grid locations, Figs 1a and 1b. Longitudinal current with (drive/measurement) Opposing/Opposing and In-line/In-line patterns produced the highest SER’s across all grid locations, Fig. 1b, however, these two patterns also produced solutions with conductivity in significantly wrong locations, Fig 1c.

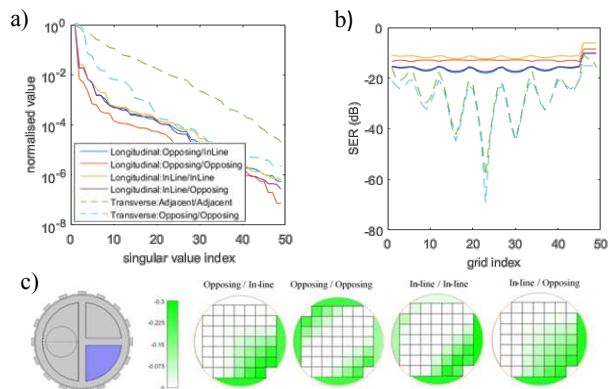


Figure 1: a) Singular values; b) SER; c) Fascicle-level neural activity (purple) reconstructed with longitudinal current drive and measurement patterns (green).

We have demonstrated, through simulations, the viability of two electrode patterns for EIT of neural activity with a longitudinal current: Opposing/In-line and In-Line/Opposing. Both produce reasonable SER magnitudes across the sample depth.

References

- [1] Adler, A., Gaburro, R., and Lionheart, W., *EIT*, in *Handbook of Mathematical Methods in Imaging: Vol 1, 2nd Ed.* 2015.
- [2] Aristovich, K., Blochet, C., Avery, J., Donega, M., Holder, D., *BAEIT, Proceedings*, 2016
- [3] Aristovich, K., Donega, M., Perkins, J., Fjordbakk, C., Avery, J., Holder, D., *BAEIT, Proceedings*, 2017.
- [4] Hope, J., Vanholsbeeck, F., McDaid, A., *Phys. Meas.*, 2018 (currently under review)

Effect of a PEEP trial on global inhomogeneity index, alveolar overdistension/collapse in cardiothoracic surgery and ARDS patients

SJH Heines, U Strauch, MCG van de Poll, PMHJ Roekaerts, DCJJ Bergmans

Department of Intensive Care, Maastricht University Medical Centre+, the Netherlands, S.Heines@mumc.nl

Abstract: With electrical impedance tomography (EIT) alveolar overdistension (OD), collapse (CL) and the global inhomogeneity index (GI) was calculated in patients with ARDS and postoperative cardiothoracic surgical patients (CTS) during a PEEP trial. We found the same changes with different PEEP levels between both groups.

The GI decreased during each incremental PEEP step and increased during each decremental PEEP step. The opposite was the case for ODCL (Fig. 1). The change in ODCL and GI during the PEEP trial was not significantly different between CTS and ARDS patients ($p=0.06$ and $p=0.54$ respectively).

1 Introduction

Several parameters derived from EIT data have been developed in order to optimize ventilator settings e.g. the best balance between alveolar OD and CL (ODCL), where the percentage of OD is subtracted from the percentage of CL. Furthermore, it has been suggested that optimal PEEP is established when ventilation is most homogeneously distributed. Therefore the GI, which quantifies the homogeneity of tidal volume distribution, has been used previously [1]. The present study describes the effect of PEEP on ODCL and GI in ARDS patients, using postoperative CTS as a reference group.

2 Methods

Seventeen CTS and 27 ARDS patients were retrospectively analysed (Table 1). The GI and ODCL was calculated at each PEEP step by EIT during an incremental and decremental PEEP trial. The analysis is performed in 4 consecutive incremental followed by 4 decremental PEEP steps of 2 cmH₂O. The smaller the GI, the more homogeneous the tidal volume is distributed. An ODCL of 0% would indicate an optimal balance between alveolar OD and CL.

2.1 Statistics

Data are expressed as a number (%) for categorical variables and as mean \pm SD for continuous variables. Characteristics between CTS and ARDS patients were compared using paired sample *t*-test. Changes in GI and ODCL between CTS and ARDS patients were tested using two-way ANOVA.

2.2 Results

There was a significant difference between CTS and ARDS patients in APACHE II and PaO₂/FiO₂-ratio ($p<0.05$).

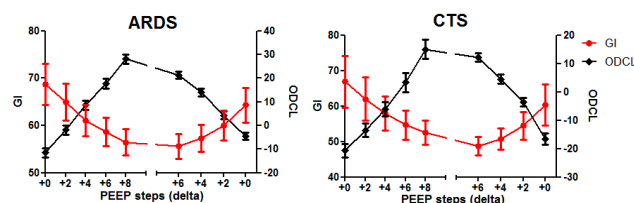


Figure 1: Changes in GI (circle) and ODCL (diamond) in CTS and ARDS patients during an incremental and decremental PEEP trial.

2.3 Discussion

Increasing airway pressure enhances homogeneous ventilation distribution. The most homogeneous ventilation resulted in the largest amount of OD in ARDS patients, this effect however was similar in CTS patients with presumably healthy lungs. Solely trying to minimize inhomogeneity without limiting the upper level of PEEP may lead to severe OD and can be harmful. Using the combination of GI and ODCL for PEEP setting may be required to develop a feasible and safe bedside tool.

3 Conclusions

Individual monitoring of regional lung mechanics using EIT is feasible and the effect of different PEEP levels can be reliably assessed. EIT has a large potential to become the golden standard tool for patient-tailored ventilator setting. Agreement on which indices, or combinations of EIT derived calculations should be used to guide ventilator setting remains to be determined.

4 Acknowledgements

Not applicable.

References

- [1] Z. Zhao, D Steinmann, I Frerichs *Crit Care*, 14(1):R8,2010

Table 1: Patient characteristics. Data are presented as means \pm SD, unless stated otherwise. (* $p < 0.05$)

	Patients (%)	Age, years (SD)	Sex (M/F)	APACHE II (SD)	PaO ₂ /FiO ₂ -ratio
ARDS	28 (62)	63 (16)	17/11	28 (8)	137 (49)
CTS	17 (38)	66 (14)	14/3	17 (5)*	339 (73)*

Patient-ventilator asynchrony

MY Chang¹ CH Gow¹ S Krueger-Ziolek² B Gong² Z Zhao^{2,3} and K Möller²

¹Department of Internal Medicine, Far Eastern Memorial Hospital, Taiwan

²Institute of Technical Medicine, Furtwangen University, VS-Schwenningen, Germany, zhanqi.zhao@hs-furtwangen.de

³Department of Biomedical Engineering, Fourth Military Medical University, Xi'an, China

Abstract: Patient-ventilator asynchrony increases work-of-breathing and prolongs patient weaning from ventilator. Inappropriate triggering might sometimes not be recognized via pressure or flow patterns. Analysis of impedance-time curves measured with EIT is able to identify the asynchrony of respiratory time.

1 Introduction

Patient-ventilator asynchrony increases work-of-breathing and the duration of mechanical ventilation. Patient-ventilator asynchrony can be detected by clinical inspection of the patient and interpretation of breath-by-breath real-time ventilator waveforms [1]. Ineffective triggering is one of the common asynchrony, where a patient's inspiratory effort does not trigger a mechanical breath because of inappropriate ventilator settings or the patient status change after the initial settings [2]. Therefore, the status of the respiratory system including the lung mechanics, respiratory muscle and neural drive should be measured and closely monitored. Chest EIT is a non-invasive and effective monitoring technique to achieve this goal. In a previous study, the effect of trigger sensitivity on redistribution of ventilation was evaluated [3].

2 Methods

A patient with chronic obstructive pulmonary disease (COPD) was mechanically ventilated under assisted-controlled ventilation (age, 84 years; height, 165 cm; weight, 71.1 kg; APACHE II score, 30). Positive end-expiratory pressure (PEEP) and driving pressure were set to 5 and 27 cmH₂O, respectively. Respiratory rate was 12 /minute. An EIT electrode belt with 16 electrodes was placed around the thorax in the fifth intercostal space and one reference electrode was placed at the patients' abdomen (PulmoVista 500, Dräger Medical, Lübeck, Germany). EIT images (each consisting of 32×32 pixels) were generated with a reconstruction algorithm based on a modified 'finite element model' [4]. EIT images were continuously measured at 20 Hz and stored. Respiratory data from the ventilator was transferred to EIT via MEDIBUS connection. The data were filtered using a Butterworth 4th degree low-pass filter with a cut-off frequency of 50/min to eliminate impedance changes synchronous with the heart rate.

3 Results

Small volumes were identified between two mechanical breaths in impedance-time curve (Fig. 1), which indicated spontaneous breaths. However, the spontaneous breaths were hard to discover in airway pressure- or flow-time curves. Further, the expiratory volume (represented with the relative impedance value) of the third breath is smaller

than inspiratory volume of the corresponding breath, which indicates the presence of intrinsic PEEP. The patient-ventilator asynchrony might be due to the trigger sensitivity. External PEEP needs to be correctly set to compensate the effect of intrinsic PEEP. Enhancing the airway management including humidification, spasmolysis and bronchodilation may reduce the airway resistance and decrease intrinsic PEEP. Further, EIT may also help to identify the distribution of intrinsic PEEP [5]. Another potential reason of the asynchrony is that the inspiratory effort occurs out of the trigger window (i.e. during a refractory period). By monitoring the relative impedance-time curve, ineffective triggering can be easily identified.

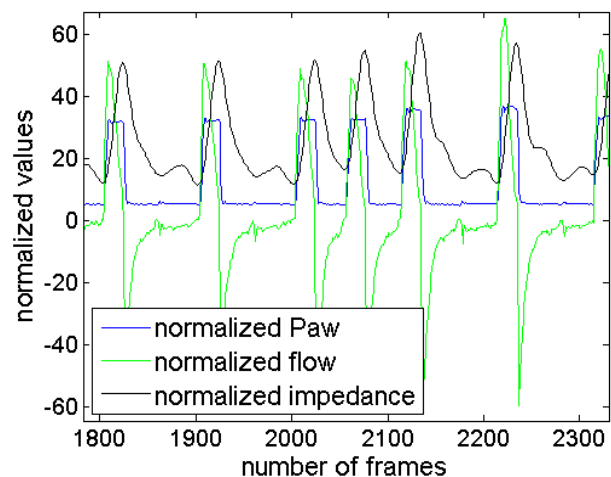


Figure 1: Patient-ventilator asynchrony identified with relative impedance-time curve measured with EIT (black line). Airway pressure (Paw, blue) and flow (green) measured with the ventilator are also plotted for comparison. Data are normalized to fit into the same axis.

4 Conclusions

In the present study, we demonstrated the feasibility using EIT to identify the ineffective triggering of the ventilator.

5 Acknowledgements

This work was partially supported by the project Far Eastern Memorial Hospital (FEMH-2018-C-077).

References

- [1] D Lynch-Smith, CL Thompson, RG Pickering, *et al. Am J Crit Care*, 25:545-551, 2016
- [2] D Gilstrap, N MacIntyre *Am J Respir Crit Care Med*, 188:1058-1068, 2013
- [3] O Radke, T Schneider, E Vogel, *et al. Anesth Pain Med*. 5:e27439, 2015
- [4] E Teschner and M Imhoff *Electrical Impedance Tomography: The realization of regional ventilation monitoring*, Lübeck, Germany, Dräger Medical GmbH. 2010.
- [5] T Mauri, G Bellani, D Salerno, *et al. Am J Respir Crit Care Med*, 188: 1466-1467 2013

Influence of noise figure controlled regularisation on derived physiological parameters in Electrical Impedance Tomography

F. Thürk¹, S. Kampusch¹, M. Elenkov¹, S. Boehme², H. Prosch³ and E. Kaniusas¹

¹ TU Wien, Institute of Electrodynamics, Microwave and Circuit Engineering, Vienna, Austria,

²Medical University of Vienna, Department of Anesthesia, Pain Management and General Intensive Care Medicine, Vienna, Austria

³Medical University of Vienna, Department of Biomedical Imaging and Image Guided Therapy, Vienna, Austria

florian.thuerk@tuwien.ac.at

Abstract: Image reconstruction in EIT is complex and not standardised for clinical use. Different algorithms produce different images and consequently yield different physiological parameters. Here, we investigated the influence of the amount of regularisation, defined by the noise figure, on derived physiological parameters.

1 Introduction

Electrical impedance tomography (EIT) is a promising tool for non-invasive lung monitoring at the bedside. However, due to the complex nature of image reconstruction, clinical images and parameters are not yet standardised and decision pathways are missing. While there are ongoing clinical trials to create the necessary knowledge foundation and also a consensus reconstruction algorithm GREIT [1], the optimal settings for the clinical routine have not yet been identified. Since the mathematical formulation of image reconstruction is “ill-posed”, regularisation is essential for numerical approaches with the hyperparameter controlling the extent of smoothing. From a theoretical perspective, the so-called noise figure nf has been introduced to quantify the effect of the hyperparameter on the basis of signal-to-noise ratios. The behaviour of different nf in the clinical setting has already been investigated [2], but further evaluations are crucial for the adaptation of EIT in the clinical routine.

In this work, the influence of different nf , in GREIT and Gauss Newton (GN) reconstruction algorithms, on the derived physiological parameters such as centre of ventilation CoV and right-left-ratio RL were investigated.

2 Methods

From one mechanically ventilated pig (ethics approval No. 53/11), contours of thorax, lungs and heart were extracted from computed tomography images. These contours were further used to create individualised finite element models as basis or the numerical forward model. Lung and heart regions were weighted (with 0.2 and 1.5) and measured voltages were normalised as $v_{\text{norm}} = \frac{v}{v(t_{\text{ref}})} - 1$. Tidal images were reconstructed using GREIT and GN algorithms with different nf ranging from 0.1 to 1 in steps of 0.1. The hyperparameter for GN was automatically chosen according to the given nf [3]. Further, reconstruction settings of GREIT, target size and weighting radius, were set to 0.08 and 0.15, respectively. For regularisation in GN, the Laplace prior was chosen.

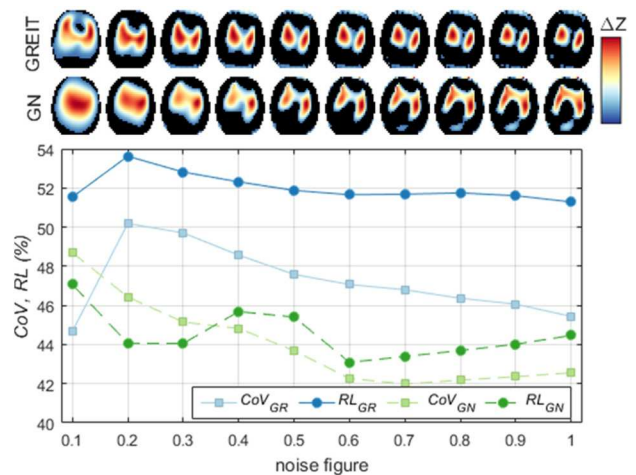


Figure 1: Reconstructed tidal images in one pig with different noise figures for GREIT (GR) and GN and the corresponding physiological parameters, CoV and RL . Please note the inverse y-axis.

The resulting images were then analysed and physiological parameters CoV of the anterior-posterior ventilation distribution and RL were calculated.

3 Results and Discussion

In GREIT, CoV and RL increased after an initial low value at $nf=0.1$. Afterwards, a steady decrease of both parameters with increasing nf could be observed. While CoV decreased quite steadily for GN until $nf=0.7$, RL showed only a slight downward trend with large variability. The total range of CoV values was 44.7% to 50.2% and 42.0% to 48.7% in GREIT and GN, respectively, leading to possibly differing interpretations of measurements (Fig. 1). Both physiological parameters differed significantly from each other ($p < 0.01$ for CoV and RL) between GREIT and GN.

Even though a strong influence of nf on physiological parameters CoV and RL could be observed, further evaluations focussing on changes of these parameters in a larger sample are essential [4]. In addition, a vast amount of reconstruction algorithms and settings exist, which will be investigated in future work.

References

- [1] Adler, Andy, et al. Physiological measurement 30.6 (2009): S35.
- [2] Zhao, Zhanqi, et al. Journal of Physics: Conference Series. Vol. 434. No. 1. IOP Publishing, 2013.
- [3] Graham, B. M., and Andy Adler. Physiological measurement 27.5 (2006): S65.
- [4] Grychtol, Bartłomiej, et al. PLoS One 9.8 (2014): e103045

Norm-Minimized Cardiac-Gated Electrical Impedance Tomography for Stroke Volume Monitoring

Saaid H. Arshad¹, Ethan K. Murphy¹, Joshua Callahan², James DeVries², and Ryan J. Halter¹

¹Thayer School of Engineering, Dartmouth College, Hanover, NH, USA

²Dartmouth-Hitchcock Medical Center, Lebanon, NH, USA

Abstract: This work explores a novel method to reconstruct electrical impedance tomography (EIT) images of the heart. A simulation study was conducted and data was collected from echocardiography patients. Simulation results were compared to the model ground truth and clinical data was validated with echocardiography.

1 Introduction

Stroke volume (SV) is the volume of blood pumped out by the heart every beat and is an important indicator of cardiovascular health [1]. Current methods of monitoring SV are not reliable in long-term, continuous monitoring settings, making it challenging for clinicians to deliver proactive healthcare. Electrical impedance tomography (EIT) has the potential to non-invasively monitor SV over long periods of time. Our previous simulation study demonstrated the sensitivity of EIT to clinically significant changes in SV [2]. The objective of this work is to demonstrate the improvement in image quality through use of norm-minimized cardiac gated averaging (NMCGA) as compared to regular cardiac gated averaging (RCGA) in an in vivo setting.

2 Methods

2.1 Data Collection

Data was collected from 30 patients scheduled for echocardiography under an IRB-approved study. EIT data was recorded immediately before the echocardiography procedures using a 32-channel SwissTom Pioneer Set with electrodes positioned around the thorax two inches above the nipple plane (T4). Pulse oximeter (PO) and ECG-based heart-rate data was collected using a BIOPAC MP150 data acquisition system. Patients were asked to perform an exhaled breath-hold (EBH), inhaled breath-hold (IBH), and no breath-hold (NBH). Data from 14 patients was not included in final analysis due to a variety of issues. Reconstructions are computed with a standard Gauss-Newton EIT algorithm using the dual-mesh method.

2.2 Norm-Minimized Cardiac Gating

The PO and ECG signals were synchronized with the EIT data using an external trigger. EIT frames associated with end-diastole (ED) and end-systole (ES) were identified using the synchronized cardiovascular signals. Conductivity difference images (Figure 1) were computed using the difference between an ES impedance data frame and an ED data frame. For RCGA, difference images between ES and ED are computed for each heart cycle over the duration of acquisition and ensemble averaged to produce a single RCGA-based image of the thorax. Averaging over multiple heart cycles provides a filtered image that suppresses noise and the effects of breathing. In

NMCGA a window of heart cycles about each ES frame is defined and the ED frame that minimizes the norm-difference between ES and ED impedances is used to compute the conductivity difference image. These images computed for each ES frame are then averaged together to define a single NMCGA-based image of the thorax.

The heart and lung regions-of-interest (ROI) are automatically segmented and features are extracted [2]. The contrast-to-noise ratio (CNR) increases by a factor of 2.6 for NMCGA images as compared to RCGA images. A multivariable regression model using heart ROI max and mean conductivities, lung ROI area, max, and mean, and height, weight, and BMI as variables was implemented with known SV from patient echocardiography reports. For RCGA images in the NBH data, an R^2 of 0.53 was achieved with an adjusted R^2 of -0.01; For NMCGA images, an R^2 of 0.95 with an adjusted R^2 of 0.89 was achieved.

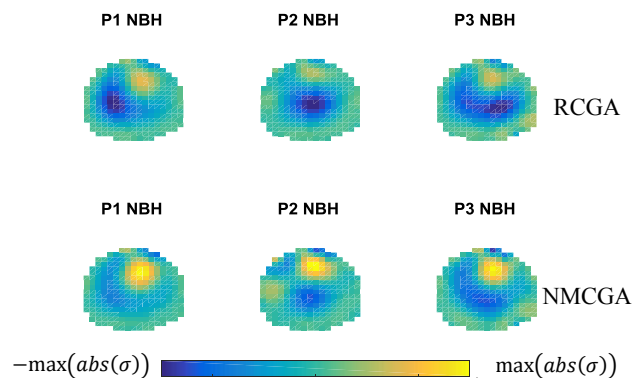


Figure 1: The region of positive conductivity change (yellow) represents blood-flow into the heart. The region of negative conductivity change (blue) represents blood flow out of the lungs, i.e. pulmonary perfusion. NMCGA images show a brighter heart ROI, indicating that the conductivity change due to SV is better isolated in these images.

3 Conclusions

NMCGA images are visually better at isolating the heart-based conductivity changes; the heart regions in the NMCGA images are brighter and larger as compared to the RCGA images, have a higher CNR, and have higher correlations when accounting for body dimensions. More data is needed to improve the generalizability of the models.

4 Acknowledgements

This study was financially supported by Funding Source: NSF (SCH-INT) 1418497.

References

- [1] Alhashemi, et al. *Critical Care*, 15(2), 214, 2011.
- [2] S. Arshad, et al. *Progress in Biomedical Optics and Imaging - Proceedings of SPIE*, February 2018.

Frequency-Differential Reconstruction Algorithm for Thoracic EIT Using Absolute Values

Tobias Menden¹, Jakob Orschulik¹, Kulthisa Sajjamark², Sébastien Dambrun¹,
Susana Aguiar Santos¹, Marian Walter¹, Steffen Leonhardt¹

¹Chair for Medical Information Technology, RWTH Aachen University, Aachen, GER, menden@hia.rwth-aachen.de

²Ruprecht-Karls-Universität Heidelberg, Grabengasse 1, 69117 Heidelberg, GER

Abstract: Frequency-differential EIT reconstructs complex regional conductivity differences. We propose to extend the traditional Gauss-Newton approach with a weighted voltage minimization similar to absolute-EIT. The reconstruction results show a smoother background area and an improved contrast between organs and background.

1 Introduction

Most EIT-systems monitor time-differential conductivity distributions. Measuring at multiple frequencies simultaneously gives information about passive electrical properties and the dispersion of biological tissue. In the long term, the underlying tissue should be identified [1]. One application of frequency-differential Electrical Impedance Tomography (fdEIT) is to monitor lung edema, due to the reduced extracellular resistance [2].

2 Methods

2.1 The Inverse Problem of EIT

In a three-dimensional domain Ω with a given conductivity $\vec{\gamma}$ the resulting voltages \vec{U} of an injected current can be easily calculated by $\mathbf{A} : \vec{\gamma} \mapsto \vec{U}$, where \mathbf{A} is the forward map of Ω . EIT tries to reconstruct $\vec{\gamma}$ from the measured surface potentials. The inverse of \mathbf{A} cannot directly be calculated, as the inverse problem is ill-posed. Therefore, a least-squares minimization $\vec{\gamma}_{opt} = \min \{\Psi\}$ is often used to estimate $\vec{\gamma}$, where Ψ is an objective function of the minimization. $\vec{\gamma}_{opt}$ is optimized in a way that the difference of \vec{U} and the calculated forward solution is minimized. Different approaches exist to solve this problem, e.g. GREIT and Gauss-Newton algorithm [3, 4]

2.2 Frequency-Differential Reconstruction

The objective function of the traditional Gauss-Newton approach is adjusted to meet the requirements for fdEIT:

$$\Psi_{absGN}(\vec{\gamma}_k^{tot}) = \underbrace{\frac{1}{2} \left\| (\Delta \mathbf{A}(\vec{\gamma}_k^{tot})) - (\Delta \vec{U}) \right\|^2}_{\text{differential-term}} + \underbrace{\frac{\lambda}{2} \left\| \mathbf{L}^{tot} \cdot \vec{\gamma}_k^{tot} \right\|^2}_{\text{regularization-term}} + \underbrace{\frac{\beta}{2} \left(\left\| \mathbf{A}(\vec{\gamma}_k^{high}) - \vec{U}^{high} \right\|^2 + \left\| \mathbf{A}(\vec{\gamma}_k^{low}) - \vec{U}^{low} \right\|^2 \right)}_{\text{absolute-term}}. \quad (1)$$

The **differential-term** includes the voltage difference at two frequencies $\Delta \vec{U} = \vec{U}^h - \alpha \vec{U}^l$, where $\Delta \mathbf{A}(\vec{\gamma}_k^{tot}) = \mathbf{A}(\vec{\gamma}_k^h) - \alpha \mathbf{A}(\vec{\gamma}_k^l)$ is the difference of the forward solution of the current conductivity solution. In addition, α describes a weighted difference coefficient as described by Jun [4] to cancel out common errors. The **regularization-term** performs a Tikhonov-Regularization

with a NOSER prior [5]. The hyperparameter λ is chosen with the L-curve criterion [6]. We introduced an **absolute-term**, which minimizes the voltage difference at each single frequency similar to absolute-EIT. The control coefficient $\beta \in [0, 1]$ was introduced to define a ratio between the absolute- and differential-minimization.

3 Results and Discussion

The reference model in fig. 1 mimics an edema in the left lung. Typical tissue-conductivities were derived from the Gabriel-database [7].

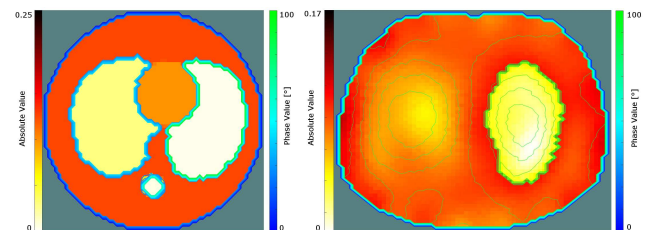


Figure 1: The magnitude of the conductivity distribution is given with the white-yellow-red colorbar. The contour lines depict the phase value with a blue-green colorbar. The Reference model include lung-lobes (one with an edema), heart and spine (left). The reconstruction result is shown on the right.

The model used for the reconstruction has a different shape as the reference model to avoid over-fitting. The background area of the image is smooth and the contrast between organs and background is improved. Especially the phase contour of the edema has a similar shape as the reference lung and has similar values.

4 Conclusions and Outlook

We developed an improved version of a weighted difference algorithm for fdEIT. The newly introduced absolute-minimization term leads to a smoother background and an improved contrast between organs. In the future, the algorithm will be evaluated on different models in simulations as well as in real fdEIT measurements.

References

- [1] Malone E, Sato Dos Santos G, Holder D, et al. *IEEE transactions on medical imaging* **33**(c):1–12, 2013
- [2] Packham B, Koo H, Romsauerova A, et al. *Physiological Measurement* **33**(5):767–786, 2012
- [3] Adler A, Arnold JH, Bayford R, et al. *Physiological measurement* **30**(6):S35–S55, 2009
- [4] Jun SC, Kuen J, Lee J, et al. *Physiological measurement* **30**(10):1087–1099, 2009
- [5] Cheney M, Isaacson D, Newell JC, et al. *International Journal of Imaging Systems and Technology* **2**(1990):66–75, 1990
- [6] Hansen PC, O’Leary DP. *SIAM Journal on Scientific Computing* **14**(6):1487–1503, 1993
- [7] Gabriel S, Lau RW, Gabriel C. *Physiology Medical Biology* **41**:2251 – 2269, 1996

Absolute Phantom Reconstructions using Fused-Data EIT

Ethan K. Murphy¹, Xiaotian Wu¹, and Ryan J. Halter^{1,2}

¹Thayer School of Engineering, Dartmouth College, Hanover, NH, USA, ethan.k.murphy@dartmouth.edu

²Geisel School of Medicine, Dartmouth College, Hanover, NH, USA, Ryan.J.Halter@dartmouth.edu

Abstract: Absolute reconstructions from gelatine prostate phantoms using fused-data transrectal electrical impedance tomography (fd-TREIT) incorporating biopsy electrode measurements are produced. The successful reconstructions are important steps toward ex-vivo and in-vivo evaluation of the technology.

1 Introduction

Detecting prostate cancer non-invasively is clinically challenging. Low threshold PSA-based screening has a high sensitivity, but low specificity due to numerous benign conditions elevating PSA levels [1]. Men with elevated levels of PSA are typically subject to an image-guided biopsy protocol for more accurate diagnosis. Unfortunately, transrectal ultrasound (TRUS)-guided biopsies miss 10-30% of all cancers [1]. A number of ex-vivo studies have shown that electrical properties exhibit significant differences between benign and cancerous prostate [2]. We have previously developed an fd-TREIT system for prostate imaging that fuses tetra-polar impedance data recorded from 18 sonolucent electrodes adhered to a TRUS probe and 4 electrodes integrated near the tip of a biopsy needle. The work presented here advances our prior efforts in fd-TREIT [3]; specifically, improvements include using 1) a realistic number of measurements that could be recovered during a standard 12-core TRUS-guided biopsy, 2) prostate phantoms with metal, plastic, and gelatine inclusions, 3) electromagnetically (EM)-tracked TRUS and biopsy probes, and 4) a parallelized-software implementation providing 8x speed-up for absolute reconstructions.

2 Methods

Gelatine phantoms were produced with either 3 inclusions (2 metal and 1 plastic bead, Fig. 1B) or one large gelatine/graphite inclusion (Fig. 1A). TRUS images were used to segment the prostate and gelatine inclusion. EM-tracking using an NDI Aurora V2 system provided 6 degree-of-freedom states of the TRUS probe and biopsy needle for each EIT measurement and of the true bead locations. For each experiment, 10 x/y-locations (needle insertion sites) were measured at 3 depths yielding a total of 30 measurement locations.

The fd-EIT approach was based on a standard Gauss-Newton algorithm using a regularization scheme optimized for open domains [4]. The fusion process utilizes a single finite element method (FEM) mesh (776k nodes, 4.4M elements) that has the TRUS probe and biopsy needle encoded. The mesh was transformed for each state and related to a fixed coarse inverse mesh using the dual-mesh method. The measurements and Jacobians are concatenated so the problem can be solved as if it were a standard EIT problem. Absolute reconstructions required 90 (30x3) forward solves and 30 Jacobian calculations for

each iteration. Three forward solves per state are due to the standard update and a parabolic linear search algorithm. Matlab's *parfor* with 16 workers solved the forward problems using Pardiso yielding a 8x speedup compared to serial runs while using up to ~150 GB of RAM. Each iteration took approximately 40 minutes, yielding total times of ~3.3 hours for 5 iterations.

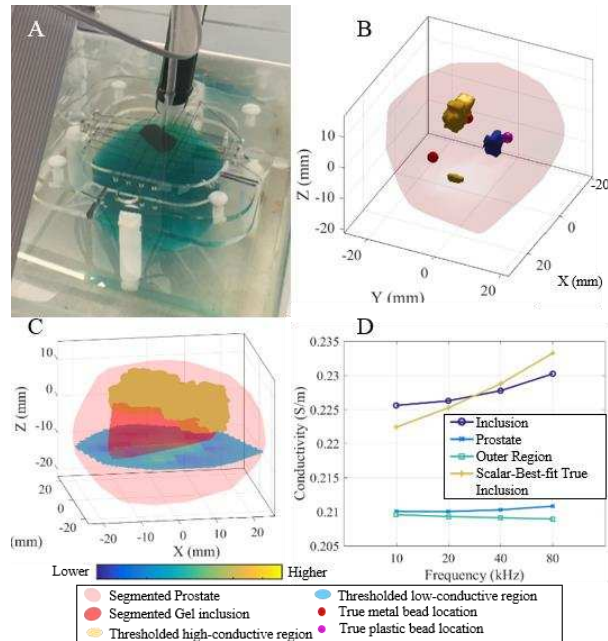


Figure 1: A. Setup for a prostate and gel inclusion experiment, absolute reconstructions of B. a 3 inclusion test and C. a gel inclusion test, and D. average values of each region from C.

The 3-inclusion experiment resulted in average position errors of 6.4 mm. The gel inclusion reconstruction resulted in 44% of the thresholded volume within the true inclusion volume and yielded frequency-dependent conductivities resembling the true inclusions.

3 Conclusions

This study represents significantly steps towards bringing this technology towards pre-clinical evaluation. Further study of EM data and TRUS images can likely improve the results and further speed-up can likely be accomplished.

4 Acknowledgements

This work was supported in part DoD CDMRP Grant W81XWH-15-1-0571.

References

- [1] Campbell's Urology, 9th ed, P. Walsh. 2007, Saunders: Philadelphia
- [2] R. J. Halter, et al., IEEE Trans. Bio. Eng., 54:1321-1327, 2007.
- [3] E.K. Murphy, et al., EIT Conf., Dartmouth, NH, USA, June 2017
- [4] E.K. Murphy, et al., IEEE Trans Med. Imag., 35:1593-1603, 2016.

Multi-plane electrode configuration for 3D cellular assay of electrical impedance tomography

Hancong Wu¹, Yunjie Yang¹, Shengheng Liu¹, Pierre O Bagnaninchi² and Jiabin Jia¹

¹School of Engineering, The University of Edinburgh, Edinburgh, UK, jiabin.jia@ed.ac.uk

²MRC Centre for Regenerative Medicine, The University of Edinburgh, Edinburgh, UK

Abstract: This paper reports the use of a miniature sensor with multi-plane electrode configuration for microporous polymer-based scaffold monitoring. Its improvement to 3D image reconstruction is verified by simulation showing the cell proliferation in a scaffold when the SNR is 50dB.

1 Introduction

3D cellular assays can better reflect the biological mechanisms of cell migration, differentiation and viability than traditional monolayer cell assays because 3D cell culture model is closer to in vivo like morphologies [1]. Previous studies demonstrate that EIT has the potential to real-time monitor the cell viability in a microporous polymer-based scaffold [2]. However, the planar electrode configuration has limited sensitivity to the conductivity variation on the top layers of the sensor, so it is only suitable to monitor the cells located on the substrate. In this study, we introduce the multi-plane electrode configuration [3] to the design of the miniature EIT sensor. Simulations have been performed to evaluate its spatial sensitivity and feasibility to monitor the cell proliferation in a microporous polymer-based scaffold.

2 Methods

2.1 Sensor design

The miniature EIT sensor was developed based on the structure of a 24-well plate. 32 rectangular electrodes (dimensions: $0.6 \times 0.8 \text{ mm}^2$) were evenly distributed on two layers at its boundary as shown in Fig.1 (a). The distance between two electrode layers is 2.5 mm.

2.2 Simulations

Simulations were performed to compare the performance of the sensor with multi-plane electrodes and the sensor with planar electrodes (Fig.1 (b)) [4]. 1 ml Dulbecco's Modified Eagle Medium (DMEM) culture medium (conductivity = 1.5 S/m) was added to the sensor to generate a liquid column at the height of 6 mm. Then, a cylindrical microporous polymer-based scaffold (diameter: 5 mm; height: 4.5 mm) seeded with cancer cells was introduced to the side of the sensor. The initial conductivity of the scaffold was 1.4 S/m and it dropped to 0.7 S/m when the cell concentration in the scaffold increased. Adjacent drive method with 1 mA stimulation current was used in the impedance measurement. The conductivity variations due to the cell proliferation are reconstructed using Tikhonov regularization.

3 Results

From the sensitivity field in Fig.2 (a), it can be seen that the sensor with multi-plane electrode configuration

generates a more homogenous sensitivity field along the vertical axis than the sensor with planar electrode configuration. With multi-planar electrode configuration, the sensor maintains more than 66% sensitivity at the top layers in comparison with the 1st layer. However, in the sensor with planar electrode configuration, the sensitivity field at 20th layer is four times smaller than that at the 1st layer. Therefore, the multi-plane electrode configuration allows the sensor to reconstruct the cell proliferation process in the whole scaffold (Fig.2 (b)) while the sensor with planar electrode configuration only sensitive to their changes at the bottom layers (Fig.3 (c)).

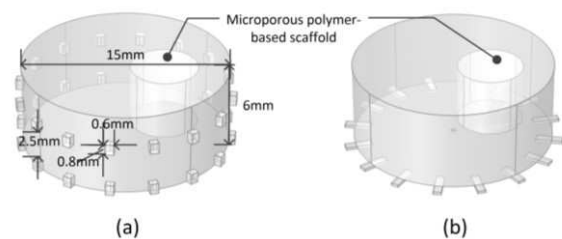


Figure 1: The miniature EIT sensor with (a) multi-plane and (b) planar electrode configuration.

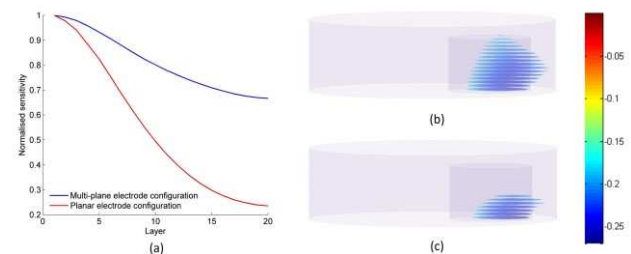


Figure 2: (a) The normalised sensitivity at $x=4\text{mm}$, $y=0$; and the reconstructed images for the 3D cell proliferation with (b) multi-plane and (c) planar electrode configuration.

4 Conclusions

Sensor with the multi-plane electrode configuration is more suitable for the 3D image reconstruction. It can monitor the conductivity variations inside the scaffolds and it has the potential to be applied in the real-time 3D imaging of the cellular activities in tissue engineering.

References

- [1] B. M. Baker and C. S. Chen, *J Cell Sci*, vol. 125, pp. 3015-3024, 2012.
- [2] H. Wu, Y. Yang, P. O. Bagnaninchi, and J. Jia, *IST2017*, pp. 1-5, Beijing, China, 2017.
- [3] Z. Hao, S. Yue, B. Sun, and H. Wang, *Computer Assisted Surgery*, vol. 22, pp. 326-338, 2017.
- [4] Y. Yang, J. Jia, S. Smith, N. Jamil, W. Gamal, and P. Bagnaninchi, *IEEE Sensors Journal*, vol. 17, pp. 514-523, 2017.

Integrating Circuit Simulation with EIT FEM Models

Alistair Boyle¹ and Andy Adler²

¹School of Electrical Engineering and Computer Science, University of Ottawa, Ottawa, Canada aboyle2@uottawa.ca

²Systems and Computer Engineering, Carleton University, Ottawa, Canada

Abstract: This work presents two methods of co-simulating the FEM-based EIT model and SPICE-based circuit models in impedance imaging.

1 Introduction

Integrating circuit simulation into the Finite Element Method (FEM) models used for Electrical Impedance Tomography (EIT) simulations may improve analysis of the complete electrical system. Combining these two models is possible because both linear circuits (at a fixed frequency) and EIT forward simulations use the same underlying numeric tools, the Cholesky decomposition (for symmetric matrices) and LU decomposition (for unsymmetric matrices), which are both incorporated into the left divide operation in Matlab. The combined matrix is block diagonal with one sparse block for the FEM model and one sparse block for the circuit model. Off-diagonal entries are used to connect the two models at the “wires” which are the individual nodes that would normally be driven by the input vector or have difference measurements calculated.

2 Modified Nodal Analysis in EIDORS

SPICE-based circuit simulation tools such as `ngspice` use Modified Nodal Analysis (MNA) to solve linear circuits [1]. Non-linear circuits require additional steps: a DC solution to determine the operating point, then a linearization of non-linear models at the operating point, and insertion of the linearized model into the matrix. Non-linear elements such as transistors and diodes have a variety of models associated with them (BSIM3, BSIM4, SIMSOI, PSP, HICUM, MEXTRAM). Linear elements are often enough to model complex circuit behaviour, for example op-amp frequency response.

As an initial implementation, only the linear circuit elements (resistors R , inductors L , capacitors C , ideal current I and voltage V sources, current $H F$ and voltage $E G$ controlled sources) have been integrated into EIDORS. A “standard”¹ SPICE netlist reader takes a SPICE netlist (Listing 1) and transforms it into a matrix using “stamps” which are similar in construction to FEM elements; a standard N -terminal element is mapped to global nodes. The nodes of the stamp are variables that hold the nodal voltages and branch currents of each circuit element. Each type of element has a different “stamp.” For linear elements, the Laplace representation gives a direct complex valued solution representing phase delay and voltage/current gain.

Listing 1: SPICE model of an ideal voltage controlled current source (`ec`) driving an electrode wire (RLC) into electrode #7 (`e7`)

```
Gs 6 0 ec 0 1.0
L4 5 6 4m
R1 e7 5 10
CL e7 0 250p
```

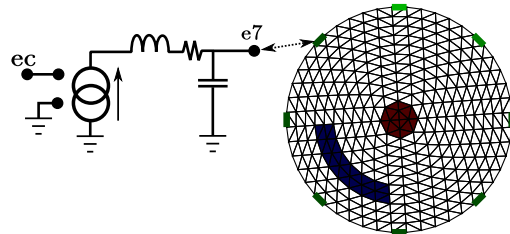


Figure 1: SPICE circuit model of wiring connected to the EIT forward model

3 Forward Modelling with SPICE

For a more complete forward model and stronger co-simulation capabilities, direct integration with SPICE would be preferable rather than re-implementing the feature-rich capabilities of a standard SPICE package. This integration is made challenging by Matlab’s `.mex` file protections which isolate sub-processes and are tied to non-system compilers. Using a model reduction of the FEM for a system matrix

$$\begin{bmatrix} \mathbf{V}_A \\ \mathbf{V}_D \end{bmatrix} = \begin{bmatrix} \mathbf{A} & \mathbf{B} \\ \mathbf{B}^T & \mathbf{D} \end{bmatrix}^{-1} \begin{bmatrix} \mathbf{0} \\ \mathbf{I}_D \end{bmatrix} \quad (1)$$

$$\mathbf{D}' = \mathbf{D} - \mathbf{B}^T \mathbf{A}^{-1} \mathbf{B} \quad (2)$$

$$\mathbf{V}_D = \mathbf{D}'^{-1} \mathbf{I}_D \quad (3)$$

the reduced matrix \mathbf{D}' can be converted to a mesh network of $n(n-1)/2$ resistors (for n electrodes). This mesh is loaded into a SPICE simulation as a subcircuit which enables the full facilities of a non-linear SPICE simulation when evaluating EIT hardware. More complete simulations are possible without making a quasi-static assumption [2], but this Partial Element Equivalent Circuit approach has not been implemented here.

4 Conclusions

Inverse problems could benefit from modelling the nonlinear behaviour of the circuits used to transmit and acquire signals in the system. This work presents two methods of co-simulating the FEM-based EIT model and SPICE-based circuit models in impedance imaging.

Integrated circuit/FEM modelling may reduce calibration effort and enable more graceful aging of equipment over its service life. SPICE does not have any specialized capabilities for inverse modelling except through manual controls to characterize circuits. A method that unites the Jacobian for the FEM model with an accurate model of the circuit Jacobian requires equations for each (non-linear) circuit stamp.

EIT-into-SPICE `eit_spice` and SPICE-into-EIT `spice_eit` implementations are available in the EIDORS repository (`solvers/forward/`).

References

- [1] T Quarles *PhD thesis*, UC Berkeley, 1989
- [2] A Ruehli *IEEE Trans. Microw. Theory Techn.* 22(3):216–221, 1974

¹There are many SPICE dialects, but the linear components generally use common prefixes amongst the many SPICE implementations.

Model based EIT signal estimation in the presence of transients: Experimental validation using 3D phantoms and *in vivo* trials

Wrichik Basu^{*1}, Michael G. Crabb², Peter M. Green¹, Paul Wright¹, and William R. B. Lionheart²

wrichik.basu@postgrad.manchester.ac.uk

¹School of Electrical and Electronic Engineering, ²School of Mathematics, University of Manchester, Manchester, UK

Abstract: Multiplexed excitation leads to the presence of significant switching transients in EIT signals. A recently proposed method using model based curve-fitting seeks to improve EIT signal measurement accuracy in the presence of transients. Results from experimental validation of the technique through advanced phantom studies and preliminary *in vivo* trials are presented and compared with standard alternative techniques.

1 Introduction

Biomedical EIT systems seek to determine the distribution of electrical impedance within a body through the injection and measurement of currents and voltages respectively at a set of electrodes positioned on the body. In a typical multiplexed biomedical EIT system [1], the current source is switched from one electrode pair to the next according to an injection pattern sequence while the voltage measurements are conducted on a subset of electrodes either sequentially or simultaneously. Due to the resistive-capacitive nature of the electrode-skin interface [2], a finite amount of charge is retained at each electrode at the end of a current injection pattern [3]. Voltage measurements on these electrodes after a switching event are then seen to be affected by transients due to the gradual dissipation of this retained charge (Fig 1).

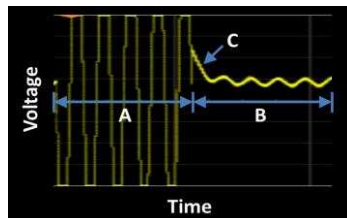


Figure 1: EIT signal with distinct transient component C, present in period B because of remnant charge from current injection in period A

The presence of such transients can affect the measurement accuracy of individual signals and subsequently, cause a reduction in image reconstruction accuracy unless an efficient mitigating strategy is adopted. This entails either waiting for the signal to settle adequately, thus incurring measurement delay, or deriving an estimate of the steady state value based on the transient affected measurements. A model based curve fitting technique to estimate EIT signal amplitude presented previously [3][4], is now validated experimentally through a succession of trials described in the next section.

2 Method

2.1 Experimental setup

The EIT system used for this experimental study is the 64 channel R3M instrument developed at the University of Manchester [5]. For the first set of experiments, a novel resistive phantom based on the wheel architecture [6] but expanded to include the effects of out-of-plane conduction and skin-electrode interface impedance is used. For the second set of experiments, the phantom used is a saline tank phantom with custom electrodes. The third and final set of data analysed in this study is from *in vivo* experiments performed on volunteers using commercially available ECG electrodes. The amplitude and frequency of excitation are chosen in accordance with typical values used in biomedical EIT applications. The duration of excitation is chosen so as to allow the recording of voltage signals for a significant period of time after the transient components have decayed to a negligible level. Due to limitations of bandwidth, only the demodulated versions i.e. in-phase and quadrature components of the measured voltage signals are stored and processed instead of the time-series of the measured samples.

2.2 Amplitude estimation

The model based estimation method presented in [4] is used to obtain estimates of the steady state values of the demodulated voltage signals. The estimates are then compared against the observed steady state signal values in order to quantify accuracy and precision of the estimation technique across a range of experimental conditions. Finally, the model based technique is benchmarked against standard alternative techniques to determine its relative merits and demerits.

3 Conclusions

The model based estimation method is seen to estimate amplitudes and time constants satisfactorily in both phantom as well as *in vivo* experiments. The impact of improved measurement accuracy on EIT images and its potential benefits to EIT based diagnostics need to be assessed next.

References

- [1] B H Brown, A D Seagar *Clin Phys Physiol Meas*, 8:A91-A97, 1987
- [2] YM Chi, T Jung, G Cauwenberghs *IEEE Rev Biomed Eng*, 3:106–119, 2010
- [3] Crabb M, Green P, Wright P, Lionheart W *Conf 16th ICEBI & 17th EIT*, p.110, Stockholm, Sweden, Jun 2016
- [4] Basu W, Crabb M, Green P, Wright P, Lionheart W *Conf 18th EIT*, p.26, Dartmouth, USA, Jun 2017
- [5] Wright P, Green P, Crabb M, Ouypornkochagorn T, McCann H, Lionheart W *Conf 16th ICEBI & 17th EIT*, p.134, Stockholm, Sweden, Jun 2016
- [6] H Griffiths *Physiol Meas*, 16: A29-A38, 1995

Biomedical Application of Capacitively Coupled Electrical Resistance Tomography (CCERT)

Yandan Jiang and Manuchehr Soleimani

Department of Electronics and Electrical Engineering, University of Bath, Bath, UK, M.Soleimani@bath.ac.uk

Abstract: Capacitively coupled electrical resistance tomography (CCERT) is a new kind of ERT that can realize contactless conductivity measurement. This work studies the basic performance of this new technique in biomedical application.

1 Introduction

Capacitively coupled electrical resistance tomography (CCERT) is proposed as a non-invasive ERT that can realize contactless conductivity measurement [1-2]. Its electrodes are not in direct contact with the medium, which means negative effects ((like electrode polarization and contamination in industrial application [2] and contact resistance in medical applications [3])) resulted from the contact measurement principle of conventional ERT [4] can be avoided and more broad applications may be available. This work is the first attempt concerning biomedical application of CCERT. First, mathematical model of a 12-electrode CCERT phantom was established to solve the forward problem and get the sensitivity matrix. Then, both measurements with only saline background and with a potato anomaly inside the background were obtained. Finally, image reconstruction was implemented with Tikhonov regularization method.

2 Measurement Principle

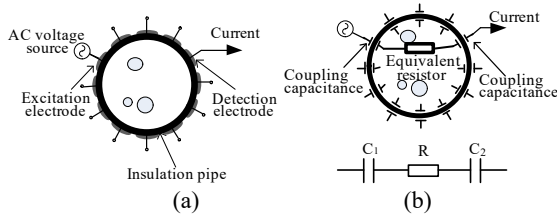


Figure 1: Measurement principle of CCERT. (a) Sensor. (b) Simplified equivalent circuit of an electrode pair.

As shown in fig.1, the electrodes of CCERT are mounted equidistantly around the outer periphery of the pipe. For each electrode pair, the two electrodes, the insulation pipe and the conductive medium inside the pipe form coupling capacitances C_1 and C_2 , and the conductive medium can be equivalent to a resistance R . So, with the excitation AC voltage applied, the current reflects the conductivity distribution between the electrode pair can be measured.

3 Forward Modelling

The model of CCERT can be described as

$$\begin{cases} \nabla \cdot ((\sigma(x, y) + j\omega\varepsilon(x, y))\nabla\phi(x, y)) = 0 & (x, y) \subseteq \Omega \\ \phi_a(x, y) = V_0 & (x, y) \subseteq \Gamma_a \\ \phi_b(x, y) = 0 & (x, y) \subseteq \Gamma_b \\ \frac{\partial\phi(x, y)}{\partial n} = 0 & (x, y) \subseteq \Gamma_c, (c \neq a, b) \end{cases} \quad (1)$$

where $\sigma(x, y)$, $\varepsilon(x, y)$ and $\phi(x, y)$ are the spatial conductivity, permittivity and potential distributions. $\omega=2\pi f$ is the angular frequency of the AC voltage source with the frequency f . Γ_n represent the boundaries of the i th electrode ($i=1, 2, \dots, 12$). \vec{n} is the outward unit normal vector. a , b and c represent excitation electrode, detection electrode and floating electrodes, respectively.

4 Research Results

4.1 Sensitivity matrix

Finite element method (FEM) is introduced to solve the forward problem [5] with 864 triangle meshes/elements. The inner diameter of the sensor is 102 mm and the electrode angle is 24° . The conductivity of the background and the object are $\sigma_0=0.05$ S/m and $\sigma_1=0.10$ S/m. For an electrode pair $a-b$, the sensitivity of the i th element is

$$S_{a-b}^i = \frac{R_{a-b}^i - R_{a-b}^0}{R_{a-b}^0(\sigma_1 - \sigma_0)} \quad (2)$$

where, R_{a-b}^0 represents the equivalent resistance between electrode pair $a-b$ when the pipe is full of background ($\sigma=\sigma_0$). R_{a-b}^i is the equivalent resistance between electrode pair $a-b$ when the conductivity of the i th element changes from σ_0 to σ_1 and the remaining elements still kept at σ_0 .

4.2 Image reconstruction

Experiments were carried out with saline (0.0575 S/m) and potato. Tikhonov regularization is introduced to implement image reconstruction. Fig. 3 shows the images reconstructed at three frequencies (400, 600 and 800 kHz).

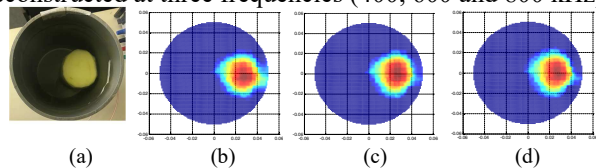


Figure 3: Reconstructed images. (a) Actual distribution. (b) 400kHz. (c) 600kHz. (d) 800kHz.

5 Conclusions

This work verifies the feasibility and potential of CCERT in further biomedical applications.

6 Acknowledgements

Financial support from China Scholarship Council (CSC) (No. 201706320268) is gratefully acknowledged.

References

- [1] BL Wang, et al. *IEEE Trans Instrum Meas*, 62(5): 1017-1024, 2013.
- [2] YA Wahab, et al. *Sens Actuators B: Chem*, 210: 602-617, 2015.
- [3] M Soleimani, et al *Physiol Meas*, 27(5): S103-S113, 2006.
- [4] BH Brown. *Meas Sci Technol*, 12(8): 991-996, 2001.
- [5] WRB Lionheart. *Physiol Meas*, 25(1): 125-142, 2004.

Noise Performance Assessment of a Wearable EIT System

Michaël Rapin^{1,2}, Fabian Braun¹, Josias Wacker¹, and Olivier Chételat¹

¹CSEM, Neuchâtel, CH, michael.rapin@csem.ch

²ETHZ, Laboratory for Orthopaedic Biomechanics, Zürich, CH

Abstract: Wearable EIT can enable novel clinical strategies for patients suffering from chronic diseases. From this observation, our research group has developed an EIT vest based on our dry-electrodes cooperative-sensor architecture. This work is a quantitative evaluation of the noise of this EIT system. The standard deviation measured on three different resistors is lower than 9 m Ω .

1 Introduction

Recently, telemonitoring of vital signs has gained a lot of interest, especially for patients suffering from chronic diseases [1]. Telemonitoring systems need to be highly integrated in order to minimize the comfort impact on patients. We have developed a wearable system which closely monitors physiological parameters (including EIT) using our patented electronic architecture which we have tailored for wearable EIT [2].

This architecture of so-called “cooperative sensors” is based on active sensors connected in a bus arrangement with two unshielded wires [3], reducing a lot the complexity of the electrical connections and of the cabling for any number of sensors in the system.

While this system was successfully tested on healthy volunteers and gave physiologically consistent results [2], a quantitative verification of its performance was missing. Here, we show the assessment of the system’s noise, one of the key performance indicators of EIT data acquisition systems.

2 Methods

Many EIT systems define their noise performances via the signal-to-noise ratio (SNR). However, SNR not only depends on the hardware quality, but also on the chosen stimulation and measurement patterns. Here, we used the test bench shown in figure 1 to focus on the assessment of the electronic circuits (i.e. current sources and voltage measurements). The setup contains one master sensor, two current injecting (type I) sensors, and two voltage measuring (type V) sensors. In each measurement, a current is injected between the type I sensors #1 and #2. This current flows through the calibration resistor R_{cal} , and the resulting voltage is measured by computing the difference between the voltages v_1 and v_2 (measured in the type V sensors #1 and #2). R_{cal} is set to three different values: 0 Ω (short circuit), 75 Ω and 150 Ω .

3 Results

Figure 2 shows a typical impedance measurement (with $R_{cal} = 150 \Omega$) during a 10 s period. In this case, the maximal

peak-to-peak noise is 51.9 m Ω and the standard deviation over the same period is 8.73 m Ω . Here, the bandwidth of the impedance measurement goes from DC to 20 Hz.

Table 1 shows the peak-to-peak noise and the standard deviation measured for the three different values of R_{cal} . The measured noise does not significantly depend on R_{cal} . Therefore, most of the noise comes from the voltage measurement (i.e. the type V sensors).

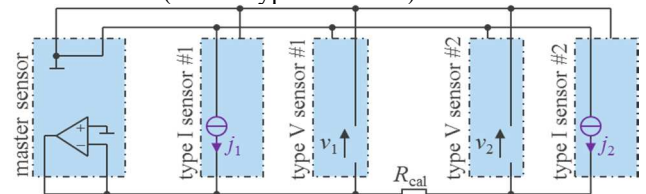


Figure 1: Test bench for noise performance assessment.

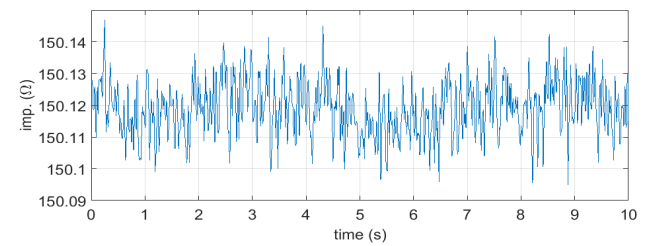


Figure 2: Noise measured on a 150 Ω resistor.

4 Conclusions

We have presented the assessment of the noise performance of our wearable EIT system. The standard deviation measured on three different resistors was 8.58 m Ω – 8.84 m Ω (measurement bandwidth: DC to 20 Hz). Since the noise is essentially the same for all resistor values, it mainly comes from the voltage-measurement (type V) sensors. Therefore, the global system performances can be enhanced by further improving the type V sensor electronics. For many EIT applications, the required bandwidth can be reduced, giving a lower noise amplitude without any modification of the sensor electronics.

5 Acknowledgements

This work was supported in part by the European Space Agency (grant 4000109393/13/NL/PA) and the European Commission (FP7-ICT-2013-10, project WELCOME).

References

- [1] B. G. Celler et al., *IEEE J. Biomed. Health Inf.*, 19:249–263, 2014
- [2] M Rapin et al., *EIT 2017*, proceedings, p. 24
- [3] M Rapin et al., *IEEE Tran. Biomed. Eng.*, 65:113–122, 2018

Table 1: Absolute measured value, peak-to-peak noise, and standard deviation measured for the three different values of R_{cal} .

R_{cal} value (Ω)	measured value (Ω)	peak-to-peak noise (m Ω)	standard deviation (m Ω)
0	0.0388	56.9	8.84
75	75.75	48.7	8.58
150	150.12	51.9	8.73

Low impedance multiple electrode array neural cuff for imaging peripheral nerve activity using Electrical Impedance Tomography (EIT)

Christopher A. R. Chapman^a, Kirill Aristovich^a, Matteo Donega^b, James Avery^a, Justin Perkins^c & David Holder^a

^a Department of Medical Physics and Biomedical Engineering, University College London, London, U.K.

^b Neural Interfacing Group, Bioelectronics R&D, GlaxoSmithKline, U.K.

^c Structure & Motion Laboratory, The Royal Veterinary College, U.K.

*christopher.chapman@ucl.ac.uk

Abstract: Here, we optimize electrode material coatings in order to achieve the best accuracy in EIT reconstructions. The testing of nanostructured electrode interface materials consisting of platinum, iridium oxide, or PEDOT:pTS in saline tank experiments demonstrated that the PEDOT:pTS coating used in this study leads to more accurate reconstruction dimensions along with reduced phase separation between recording channels.

1. Introduction

Avoidance of off-target effects in disease treatment by electrical stimulation of autonomic nerves with electroceuticals is possible with fast neural EIT^{1,2}. This was developed for brain imaging but has been adapted for imaging in nerve with a cylindrical cuff with 14 circumferential stainless-steel foil electrodes on silicone rubber, coated with platinum black, each 3 x 0.47mm. With this, compound action potentials were imaged in rat sciatic nerve with a resolution of 0.3 ms and < 200 μ m. However, image quality was limited by limited charge transfer, inconsistent electrode impedance and phase, as well as mechanical friability. The purpose of this study was to evaluate the properties of 3 new electrode materials, and test their performance in imaging fast neural activity in an *in vivo* setting.

2. Methods

Electrodes were made from laser cut 12.5 μ m-thick stainless-steel foil with silicone base and insulation to the above geometry. The electrode surfaces were laser ablated with 50 μ m pitch to roughen the foil and electrochemically plated with platinum, iridium oxide or PEDOT:pTS. Saline tank experiments were performed for validation of the electrode performance for each material. *In vivo* imaging of fast neural activity in the vagus nerve of an anaesthetized sheep was then done using the identified best electrode material.

3. Conclusions

Performance of the PEDOT:pTS coating was the best. The impedance at 1 kHz and charge storage capacity after 800 cycles, determined through impedance spectroscopy and cyclic voltammetry, were $297 \pm 1.04 \Omega$ and 89.39 mC/cm^2 compared to $340 \pm 1.02 \Omega/77.82 \text{ mC/cm}^2$ for iridium oxide and $377 \pm 1.02 \Omega/44.96 \text{ mC/cm}^2$ for platinum. Phase shift between electrode pairs during EIT recording with a current of 100 μ A and 9 kHz was significantly reduced for PEDOT:pTS at $0.49 \pm 0.06^\circ$ ($p < 0.05$) compared to $1.02 \pm 0.07^\circ$ and $0.93 \pm 0.08^\circ$ for iridium oxide, and platinum respectively. Reconstruction of EIT data taken from

the PEDOT:pTS and iridium oxide cuffs had improved shape accuracy while, PEDOT:pTS and platinum had improved size accuracy. PEDOT:pTS cuffs were then used to image compound action potentials of the recurrent laryngeal nerve from within the vagus nerve.

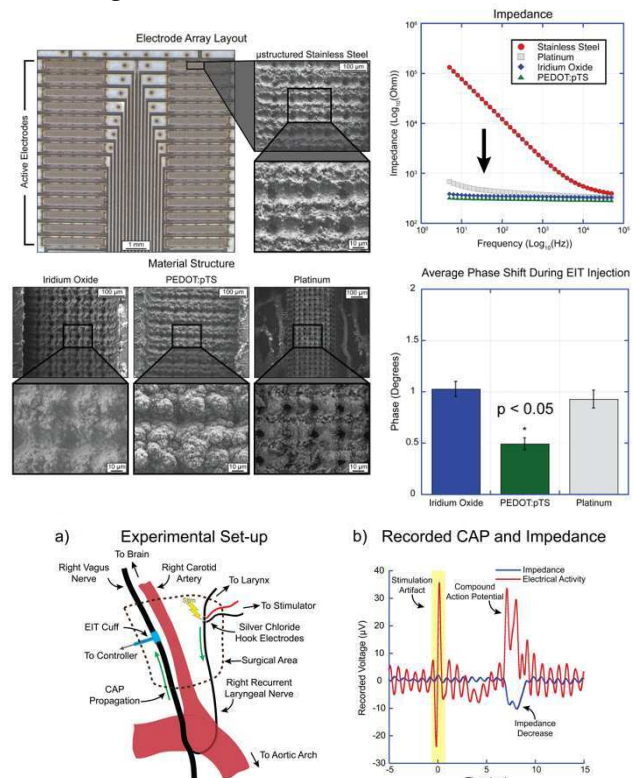


Figure 1 – Bright field image of electrode surface with low and high magnification images of the electrochemically deposited materials. Real impedance for each electrode material (including stainless-steel) on a 1.05 mm² area electrode opening. Quantification of phase differences between electrodes during EIT injection for each material. The experimental set-up for the *in vivo* experiment and the recorded compound action potential with overlaid measured impedance change.

References

1. Aristovich, K. Y., Dos Santos, G. S. & Holder, D. S. Investigation of potential artefactual changes in measurements of impedance changes during evoked activity: implications to electrical impedance tomography of brain function. *Physiol. Meas.* **36**, 1245–59 (2015).
2. Aristovich, K. Y. *et al.* Imaging fast electrical activity in the brain with electrical impedance tomography. *Neuroimage* **124**, 204–13 (2016).

Effect of intravenous fluid administration on end-expiratory lung impedance in critically ill adult patients

Tobias Becher¹, Anna Wendler¹, Christine Eimer¹, Norbert Weiler¹ and Inéz Frerichs¹

¹Department of Anaesthesiology and Intensive Care Medicine, University Medical Centre Schleswig-Holstein, Campus Kiel, Kiel, Germany.

tobias.becher@uksh.de

Abstract: End-expiratory lung impedance (EELI) can be influenced by changes in lung aeration as well as by changes in intrathoracic fluid content. We assessed the effect of a routine fluid administration on EELI in critically ill patients and found a highly significant and clinically relevant decrease in EELI.

1 Introduction

There is an increasing interest in thoracic EIT as a bedside monitoring tool for patients in intensive care units (ICUs). Clinically, differences between inspiration and expiration (tidal impedance difference, TID) are used to monitor ventilation distribution [1] whereas changes in EELI are sometimes used to monitor changes in end-expiratory lung volume (EELV) [2]. However, pulmonary bioimpedance may also be influenced by changes in intrathoracic fluid content [3]. We aimed to assess changes in TID and EELI during intravenous (iv) fluid administration according to routine clinical practice.

2 Methods

We performed a prospective observational clinical study including 25 mechanically ventilated ICU patients under monitoring with EIT (PulmoVista 500, Dräger, Lübeck, Germany) and transpulmonary thermodilution cardiac output (PICCO, Pulsion, München, Germany), who were clinically considered as requiring iv fluid administration. EIT and PICCO data were acquired 15 minutes before fluid administration (T1), from the start of fluid administration (T2) until the end of fluid administration (T3) and 30 minutes after fluid administration (T4). Fluid administration was performed by infusing 500 ml of crystalloid solution (Sterofundin ISO, Braun, Melsungen, Germany) over approximately 15 minutes. We assessed changes in EELI and TID globally and regionally for the ventral and dorsal image region. Changes in EELI were

assessed in comparison to T1 and normalized to the TID at T1. Statistical analysis was performed by Analysis of Variance (ANOVA) for repeated measures with Bonferroni post test.

3 Results

Before the beginning of fluid administration (T2), there was no significant change in EELI compared to T1. At T3, we found a change in EELI of -0.91 times TID at T1 ($p < 0.0001$) which persisted at T4 (-0.78 times TID at T1, $p < 0.0001$). These findings were similar for the ventral and dorsal lung regions. TID did not differ globally nor regionally between T1-T4. All values of TID and EELI are summarized in table 1.

Patients were ventilated with a mean tidal volume of 598 ± 133 ml (mean \pm standard deviation) which did not change significantly during the study period. During the study period, there were no differences in gas exchange or respiratory system mechanics.

4 Conclusions

Routine clinical fluid administration leads to a highly significant and clinically relevant decrease in EELI that cannot fully be explained by a loss in EELV. During fluid administration, monitoring of EELI may be unsuitable for monitoring changes in EELV.

References

- [1] Frerichs I, Amato MB, van Kaam AH et al. *Thorax*, 72:83-93, 2017
- [2] Mauri T, Eronia N, Turrini C et al. *Intensive Care Med*, 42:1576-1587, 2016
- [3] Bodenstern M, Wang H, Boehme S et al. *Physiol Meas*, 33:1225-1236, 2011

Table 1: Tidal impedance distribution (TID) and change in end-expiratory lung impedance (EELI) in arbitrary units (a.u.) for the time points T1 (15 minutes before start of fluid administration), T2 (immediately before start of fluid administration), T3 (immediately after end of fluid administration) and T4 (30 minutes after end of fluid administration). All values are given as mean \pm standard deviation. *, significantly different from T1.

	T1	T2	T3	T4	P
TID (a.u.)	2041 \pm 850	2223 \pm 1009	2007 \pm 980	2122 \pm 1079	n.s.
TID ventral (a.u.)	1248 \pm 576	1317 \pm 661	1221 \pm 613	1253 \pm 626	n.s.
TID dorsal (a.u.)	787,4 \pm 453	906 \pm 491	796 \pm 490	868 \pm 572	n.s.
EELI (a.u.)	318 \pm 215	385 \pm 333	-1023 \pm 428 *	-831 \pm 853 *	< 0,0001
EELI ventral (a.u.)	192 \pm 155	240 \pm 226	-685 \pm 318 *	-535 \pm 605 *	< 0,0001
EELI dorsal (a.u.)	126 \pm 133	144 \pm 193	-338 \pm 202 *	-297 \pm 518 *	< 0,0001

Effect of suctioning on chest EIT findings in neonates: preliminary results of a multicentre clinical study

Claas Strodthoff¹, Tobias Becher¹, Martijn Miedema², Merja Kallio³, Thalia Papadouri⁴,
Andreas Waldmann⁵, Louiza Sophocleous⁶, Rebecca Yerworth⁷, Richard Bayford⁸,
Anton van Kaam², Inéz Frerichs¹

¹Department of Anaesthesiology and Intensive Care Medicine, University Medical Centre Schleswig-Holstein, Campus Kiel, Kiel, Germany claas.strodthoff@uksh.de

²Department of Neonatology, Emma Children's Hospital, Academic Medical Centre Amsterdam, Amsterdam, The Netherlands

³PEDEGO Research Group, University of Oulu and Department of Children and Adolescents, Oulu University Hospital, Oulu, Finland

⁴Neonatal Intensive Care Unit, Arch. Makarios III Hospital, Nicosia, Cyprus

⁵Swisstom, Landquart, Switzerland

⁶KIOS Research Centre, Department of Electrical and Computer Engineering, University of Cyprus, Nicosia, Cyprus

⁷Medical Physics and Biomedical Engineering Department, University College London, London, UK

⁸Department of Natural Sciences, Middlesex University, London, UK

Abstract: We investigated EIT examinations of neonates and young infants taken in ICUs for effects of documented clinical and nursing interventions. Specifically we analysed endotracheal suctioning and found no significant difference of EIT findings before, during and after the intervention.

1 Introduction

The Continuous Regional Analysis Device for neonate Lung (CRADL) project is an EU-funded project that includes an observational study in which EIT technology is applied to neonates and young infants in multiple ICUs across Europe. 200 patients are planned to be included for up to 72 hours of recording time. Secondary endpoints of this study consider the effects of numerous documented events, such as intubation/extubation, suctioning, or posture changes, on regional lung ventilation as measured with EIT. Routine suctioning is a relatively common event which is expected to have an effect on these findings, as has been shown in adults[1].

2 Methods

The first step was the validation of the documented events based on the video log. For each suctioning intervention, the exact end of the intervention was noted along with the location (oral/nasal vs. tracheal) and the used suctioning system (open vs. closed). The EIT devices used were *BB*² (Swisstom, Landquart, Switzerland).

A breath detection algorithm optimised for neonatal use was applied to generate tidal images showing the differences between inspiration and expiration. From these tidal images, we assessed the ventrodorsal centre of ventilation, the ventilated area (defined as percentage of image pixels with impedance change ≥ 0.25 * maximum pixel impedance change in image), the global inhomogeneity index, the co-

efficient of variation and the tidal impedance variation[2].

These EIT findings were then compared in different time intervals before/during/after the validated events using *R* (Kruskal-Wallis test followed by Mann-Whitney U test against *before* interval). The used intervals lasted 5 min and started 10, 5, and 0 min before the validated end of event for the *before*, *during*, and *after* interval, respectively.

3 Results

For our preliminary analysis, we assessed data sets from 90 patients for tracheal suctioning interventions, which occurred 271 times in 22 of these patients (68% male, mean weight 1911g, mean post menstrual age 33 weeks). None of the mentioned EIT findings exhibited significant differences between the observed intervals (Table 1). These results hold true for suctioning with open and closed systems individually.

4 Conclusions

With this analytic approach no significant differences in EIT findings could be found between intervals before, during, and after routine endotracheal suctioning maneuvers. These results imply that regional ventilation is not significantly affected by suctioning. This finding may be due to the small catheter diameter resulting in low flow rates or due to leakage around the usually uncuffed tube.

5 Acknowledgements

This project has received funding from the European Union's Horizon 2020 research and innovation programme under grant agreement No 668259.

References

- [1] A Corley et al. *J Crit Care*, 27, 6:742.e1-7, 2012
[2] I Frerichs et al. *Thorax*, 72, 1:83-93, 2017

Table 1: Descriptive statistics and p-values for the observed EIT findings (preliminary results).

EIT finding	<i>before</i>	<i>during</i>	<i>after</i>	p-value
centre of ventilation %	51.60 (50.34-53.28)	51.61 (50.27-53.16)	51.95 (50.55-53.39)	0.55
ventilated area %	21.44 (17.67-25.17)	20.55 (17.89-25.19)	21.42 (18.29-25.03)	0.76
global inhomogeneity index	1.26 (1.19-1.46)	1.28 (1.20-1.46)	1.26 (1.20-1.51)	0.48
coefficient of variation	1.97 (1.80-2.37)	2.05 (1.81-2.41)	2.00 (1.80-2.39)	0.68
tidal impedance variation	0.40 (0.27-0.53)	0.41 (0.29-0.55)	0.36 (0.27-0.52)	0.29

Localisation of pixels representing the aorta in electrical impedance tomography images based on time and frequency domain features.

M. Elenkov¹, F. Thürk¹, AD. Waldmann², K. Wodack³, D. Reuter⁴, SH.Böhm⁴, E. Kaniusas¹

¹Institute of Electrodynamics, Microwave and Circuit Engineering, Vienna University of Technology, Vienna, Austria
martin.elenkov@student.tuwien.ac.at

²Swisstom AG, Research and Development Department, Landquart, Switzerland

³University Medical Centre Hamburg-Eppendorf, Hamburg, Germany

⁴University of Rostock, Department of Anaesthesiology and Intensive Care Medicine, Rostock, Germany

Abstract: Aortic pixels in electrical impedance tomography (EIT) images were detected in two pigs during apnoea periods using a novel algorithm. The locations were validated versus the aortic region segmented from computed tomography (CT) images of these pigs and the aortic region that was detected with the previously described peak prominence saline bolus injection method.

1 Introduction

Invasive peripheral catheterisation is currently the gold standard for clinical blood pressure (BP) measurement, although it is known that peripheral and central BP values can drift, in particular in critical illness [1]. Due to its fairly high sampling rate and non-invasiveness, EIT is a candidate technology for continuous, non-invasive monitoring of haemodynamic parameters like BP or stroke volume.

When using EIT, an accurate detection of the aorta is important for calculation of haemodynamic parameters. Once the aorta has been detected, the waveform can be analysed. In this work, a novel algorithm for the detection of aortic pixels in EIT images is presented.

2 Methods

2.1 Study protocol

The study was approved by the local authorities for animal care (approval no. 70/11). EIT (Swisstom, Switzerland) and ECG (BIOPAC, USA) measurements, as well as CT volume scans were performed in two anaesthetised and mechanically ventilated animals. Apnoea was induced during which a saline bolus (10 ml, 20 %) was injected into the descending aorta to increase regional conductivity contrast [2]. The EIT images were reconstructed with the GREIT reconstruction algorithm ($nf=0.7$, $wr=0.2$, $ts=0.02$) [3].

2.2 Aorta detection

The developed algorithm is based on a discrimination function. This function can be thought of as a map that

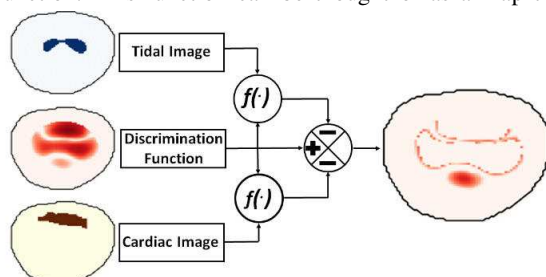


Figure 1. Schematic representation of the algorithm designed for aortic detection

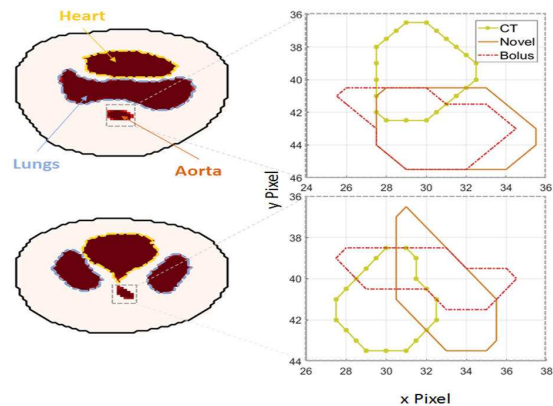


Figure 2. Left: The results of the discrimination function after applied threshold criterion. Right: the contours of the aortic region detected with three different methods.

holds a certain value for each image pixel roughly representing the likelihood of this pixel being a part of the cardiovascular system. The discrimination function is the result of a pixel wise multiplication of three maps. Map 1 represented the maximum of the cardiac waveform, Map 2 the maximum of its derivative and Map 3 represents the power spectral density exhibited by each pixel in a range of 0.75 to 1.5 times the cardiac frequency. For Map 1 and 2, ensemble averaging with ECG gating was used to obtain robust EIT time segments corresponding to cardiovascular modulations. Additionally, pixels closest to the border were penalised, because EIT is most sensitive in these regions leading to artefacts [4]. Finally, active regions from a tidal image and a cardiac image were excluded from the discrimination function (Figure 1).

3 Results and Conclusions

Figure 2 shows the results of the autonomous detection of the aortic region. A strong overlap between aortic regions detected by the novel algorithm presented in this work and by both reference methods, either CT-based (F1-score 0.2414 and 0.25) or by the injection of a saline bolus [5] (F1-score 0.8125 and 0.5128), compare Fig. 2. In future work, a larger sample size and the aorta specific stroke volume will be evaluated.

References

- [1] McDonald, D. A. Blood flow in arteries. London, 1974
- [2] Wodack, Karin H. et al. Accepted for "Physiological measurement (2018)
- [3] Adler, Andy, et al. "Physiological measurement 30.6 (2009): S35.
- [4] DS Holder *Electrical Impedance Tomography* IOP Publishing: Bristol, 2005
- [5] Thürk, F., et al. *Conf 16th ICEBI & 17th EIT*, p.121, Stockholm, Sweden, Jun 2

Phase-contrast functional EIT images

Andy Adler¹, Martijn Miedema², David Tingay³

¹Carleton University, Ottawa, Canada

²Academic Medical Center, Amsterdam, Netherlands

³University of Melbourne, Australia

Abstract: We describe a phase-contrast functional EIT measure which is useful for measurements on patients receiving HFOV. The measure calculates the regional phase offset, which appears to provide useful information on regional lung mechanics.

1 Introduction

High frequency oscillatory ventilation (HFOV) is a type of mechanical ventilation which uses rapid pressure oscillations (up to 15 Hz) around a constant distending pressure. Since rapid oscillations permit low tidal volumes, HFOV is understood to act as a lung protective mode of ventilation, and is therefore seeing increasing use, especially for the delicate lungs of preterm infants. One concern with HFOV is that the actual volume delivered to the patient is very difficult to monitor, and EIT has shown significant promise for this application [1], since modern EIT hardware is fast enough to capture the relevant volume changes.

Lung mechanics is typically characterized by parameters of compliance ($C = \frac{L}{\text{kPa}}$) and resistance ($R = \frac{\text{kPa}}{L \cdot s}$). EIT-derived measures of volume are mostly proportional to the dynamic compliance, but yield no information on R . Increases in tissue resistance reflects narrowing of airways and changes in parenchyma. The time constant $\tau = RC$ of tissue introduces a delay in the ventilation signal, which results in a change of phase in the regional EIT signal.

We describe a measure of the regional phase change and an algorithm to calculate it efficiently. We then show an analysis of phase change during pneumothorax [2].

2 Methods

Using phasor notation, measurable quantities correspond to the real component of signals. For a HFOV frequency $\omega = 2\pi f_{\text{HFOV}}$, ventilator pressure (Airways Opening) $P_{\text{AO}} = P_{\text{MAP}} + \Delta P e^{j\omega t}$. For an EIT image voxel v , $V_v - V_{\text{MAP}} = C_v \Delta P e^{j\omega(t-\tau_v)} = C_v \Delta P (e^{-j\omega\tau_v}) e^{j\omega t}$ (assuming appropriate calibration). Thus, EIT amplitude is proportional to the regional C_v , while EIT phase $e^{-j\omega\tau_v}$ is related to the regional time constant.

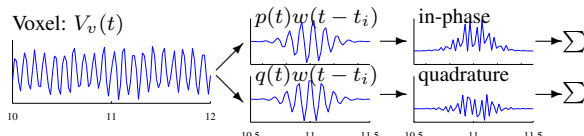


Figure 1: Phase detection: voxel waveform (left) multiplied by windowed p, q (centre) to produce (right) which are summed.

An EIT-phase fEIT image is calculated by processing EIT waveforms as follows (fig. 1).

- Calculate the HFOV frequency and phase, either from the ventilator or from the global EIT signal, from which in-phase ($p(t) = \cos \omega t$) and quadrature ($q(t) = \sin \omega t$) references are calculated.
- If the ventilator and EIT system are not perfectly synchronized, we recommend detecting $p(t)$ via a

narrow-band filter, and $q(t) = H(s(t))$ via the Hilbert transform, $H(\cdot)$.

- A window $w(t - t_i)$ is chosen (triangular with 1 s width); at each time of interest t_i , calculate: $p_w = w(t - t_i)p(t - t_i)$ and $q_w = w(t - t_i)q(t - t_i)$
- For EIT voxel v with waveform V_v , $P(t_i) = \int p_w(t - t_i)V_v(t)dt$, and $Q(t_i) = \int q_w(t - t_i)V_v(t)dt$.
- $v(t_i)$ has amplitude and phase of $P(t_i) + jQ(t_i)$.

Phase is not calculated (set to zero) for low amplitude voxels. This approach may be accelerated in the frequency domain, using the relationship $P(t_i) = \int p_w(t - t_i)V_v(t)dt = p_w \otimes V_v$, which can be represented as the multiplication of Fourier transforms. Thus $P(t_i), Q(t_i)$ are samples of a windowed narrow-band filter of V_v .

3 Results and Discussion

Fig. 2 analyses the data of [2] to calculate functional images before and after the onset of pneumothorax. As expected, a large volume of air enters the thorax, as shown in the *Aeration* image. The distribution of ventilation, *Compliance*, shows small changes. Interestingly, there is a contrast in the *Phase* image before the onset of pneumothorax, in a location which predicts the eventual gas buildup.

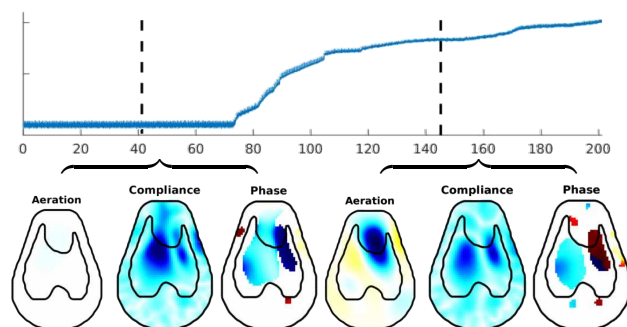


Figure 2: Functional EIT images from data of [2]. *Top:* global EIT signal vs. time (s). Vertical bars indicate time points at which fEIT images are calculated (each scaled individually to maximum value). *Aeration:* Δ EIT with respect to $t = 0$; *Compliance:* Amplitude $\|P + jQ\|$; *Phase:* Phase of $P + jQ$.

In summary, we describe the calculation of phase functional EIT images from EIT data during HFOV ventilation. Such images promise additional information on the distribution of lung mechanical properties. Our example shows a promising application, which we are pursuing in a larger set of data.

A number of engineering challenges to this analysis remain, such as the phase unwrapping of EIT-phase signals, since phase must be consistent across a boundary. We currently do not unwrap phase, since our attempts to use classic approaches did not yield useful images.

References

- [1] GK Wolf *et al*, *Ped Crit Care Med*, 11:610–615, 2010
- [2] Miedema M *et al*, *Am J RCCM*, 194:116–118, 2016.

Ion diffusion measurement using DT-MREIT

Munish Chauhan¹, Magdoom Kulam², Alec Brown², Thomas H Mareci², and Rosalind J Sadleir¹

¹SBHSE, Arizona State University, rosaland.sadleir@asu.edu

²Dept. of Biochemistry & Molecular Biology, University of Florida

Abstract: The ability to detect changes in tissue conductivity over time could provide novel diagnostic information. In this study, we used Diffusion Tensor Magnetic Resonance Electrical Impedance Tomography (DT-MREIT) to monitor temporal changes in the conductivity distribution of two different agarose gel phantom.

1 Introduction

Magnetic resonance electrical impedance tomography (MREIT) studies have focused primarily on reconstructing static and isotropic-conductivity distributions [1]. Recently devolved DT-MREIT methods can be used to reconstruct anisotropic conductivity tensors using MREIT and diffusion weighted images gathered from a subject [2]. In this study, we assess the ability of DT-MREIT to monitor temporal changes in the conductivity distribution of two different agarose gel phantom, using 1.5 mA imaging currents.

2 Methods

Imaging experiments were conducted on two cylindrical phantoms with a 10 cm diameter and 12 cm height. The first phantom (Phantom A) consisted of an annulus of agarose gel background material (~ 0.5 S/m), and agarose gel central cylindrical inclusion (~ 1.6 S/m). The second phantom (Phantom B) consisted only of the agarose gel background material (~ 0.5 S/m). Both phantoms were imaged in a Philips 3T MRI scanner during external MREIT current injection. A current intensity of 1.5 mA with a frequency of ~ 10 Hz was applied to the surface of gel via carbon electrodes (~ 36 cm²) for two independent and orthogonal directions. T1-weighted, MREIT and DWI data were obtained in the same imaging session following [3] and co-registered for image reconstruction. Multiple MREIT runs were performed on each phantom to investigate ion diffusion. Reconstructed conductivities were compared with four-terminal conductivity measurements (HP 4192A) performed on separate bulk samples of each phantom material. The measured mean conductivity of inclusion and background material were 1.6 S/m and 0.5 S/m, respectively.

DWI data was processed to diffusion tensors using FSL. Calculation of J^p was recovered from MREIT B_z by following [4] and was used to calculate diffusivity ratio [2], η . Finally, the conductivity tensor was obtained by multiplying the diffusion tensor by the η distribution. Reconstructed mean conductivities (MC) in each image

were computed via $MC = (\lambda_1 + \lambda_2 + \lambda_3)/3$, where λ_1 , λ_2 and λ_3 were principal conductivity eigenvalues.

3 Results

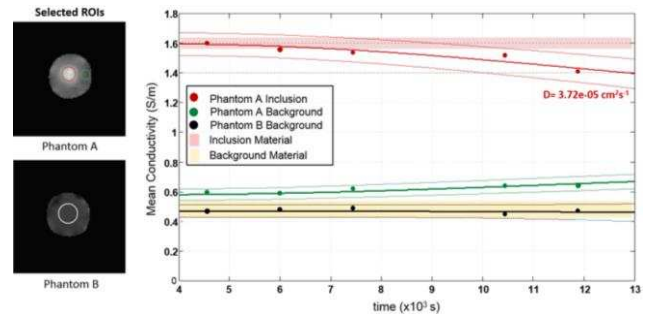


Figure 1: Plot of independently determined mean conductivities and 95% confidence intervals for background (yellow shading) and inclusion (red shading) materials, compared with MC value 95% confidence intervals in reconstructed ROIs of Phantoms A and B. Left figure shows locations of inclusion (red) and background (green) ROIs in Phantom A (left) and background material ROI in Phantom B (right). The conductivity of the inclusion decreased from around 1.6 S/m to 1.4 S/m over the course of the experiment and background material ROI increased from 0.6 S/m to 0.64 S/m.

The peak concentration C was located at the centre of the disc, and can be described for time $t > 0$ using the expression $C = C_0(1 - \exp(-a^2/4Dt))$ [5]. We fitted MC values to this equation, and found an experimental diffusion constant of 3.7×10^{-5} cm²sec⁻¹ for the central inclusion, which is higher than the value of 1.88×10^{-5} cm²sec⁻¹ calculated from the DWI data. Also, this value was higher than the previously reported measurements of 1.4×10^{-5} cm²sec⁻¹ [6] and 5.8×10^{-6} cm²sec⁻¹ [5]. Perhaps the large diffusion value we observed results from the short time we allowed for diffusion mixing and/or because our phantom was larger overall than the materials used previously [5, 6].

4 Conclusions

We reconstructed mean conductivities for two phantoms using DT-MREIT technique. The results indicate that DT-MREIT could monitor the changing conductivity distribution resulting from the diffusion of ions within the agarose gel phantom.

References

- [1] JK Seo & EJ Woo *Physiol Meas*, 29; R1–R26, 2008
- [2] OI Kwon et al. *IEEE Trans Biomed Eng*, 63(1);167–75, 2015
- [3] AK Kasinadhuni et al. *Brain Stimul*, 10(4);764–772, 2017
- [4] C Park et al. *Phys Med Biol*, 52; 3001–3013, 2007
- [5] MJ Hamamura et al. *Proc Intl Soc Mag Reson Med*, 3386. 2006
- [6] EJ Schantz & MA Lauffer *Biochem*, 1;658–63. 1962.

Comparison of reconstructed in-vivo current densities for F3-RS and F4-LS electrode montages

Saurav Z K Sajib¹, Munish Chauhan¹, Aprinda Indahlastari¹, Aditya Kumar Kasinadhuni²,
Magdoom Kulam², Thomas Mareci², R J Sadleir¹

¹School of Biological and Health Systems Engineering, Arizona State University, Tempe, USA

²Biomedical Engineering, Biochemistry, University of Florida, Gainesville, USA rsadleir@asu.edu

Abstract: MR-based current density imaging (MR-CDI) techniques aim to measure current density vectors produced by external current injection throughout a tissue volume. Previous work used MR-CDI to measure the current flow between the T7-T8 and Fpz-Oz electrode montages during tDCS [2]. In this work, we compare current flow for F3-RS and F4-LS montages using a recently developed iterative technique for MR-CDI reconstruction.

1 Introduction

Transcranial direct current stimulation (tDCS) is a new neuro-modulatory technique. Success of tDCS treatment depends on the current flow inside the brain region. Many computational simulations have been performed using estimated conductivity distributions [1]. However, until recently, direct measurements of current distributions have not been possible. Recent work from Kasinadhuni *et al.* [2] demonstrated measured current density distribution for T7-T8 and Fpz-Oz electrode montages. These montages involve ‘in-plane’ current flow, but it is unclear how results may be affected by current flow out of the image plane. In this paper, we report experimental CDI results in human subjects for F3-RS and F4-LS electrode montages. We compared model-predicted current densities derived from subject-specific anisotropic volume conductor model obtained from T1 and DT-MRI scans with measured magnetic flux density data [3].

2 Methods

2.1 Human imaging experiment

Two healthy human subjects were recruited for this study. All imaging experiments were performed in the same session using 3T Phillips Achieva scanner installed at UF McKnight Brain Institute. To build subject specific volume conductor models, T1-weighted MR images were acquired using 3D FLASH gradient echo sequence with FOV 240 x 240 x 160 mm³ and 1mm³ isotropic resolution. A subsequent, DT-MRI scan was also performed using HARDI protocol with 2 mm³ isotropic resolution. We also measured magnetic flux density data for three slices using a multi-gradient echo pulse sequence and a resolution of 2.24 x 2.24 x 5 mm³. A detailed description of data acquisition and the volume conductor model generation can be found in [2].

2.2 Reconstruction of current density image

To reconstruct current density images, at the beginning we solve the Laplace equation and determine the model predicted current and magnetic flux density. In this step we assume that, the conductivity tensor is a scalar multiple

of water diffusion tensor. We then iteratively updated the internal current density distributions by subtracting the measured and computed magnetic flux densities as [3],

$$\mathbf{J}^{n+1} = \mathbf{J}^n + \frac{1}{\mu_0} \left(\frac{\partial(B_z^e - B_z^n)}{\partial y}, -\frac{\partial(B_z^e - B_z^n)}{\partial x}, 0 \right) \quad (1)$$

where B_z^e is the experimentally obtained magnetic flux density data and \mathbf{J}^n, B_z^n are the n -th computed current density vector and z -component of magnetic flux density data at n^{th} iteration, respectively.

3 Results

Figure 1(a) shows MR magnitude image obtained during MREIT session. Magnitude of reconstructed current density distributions at the three slice positions (5th iteration) for F3-RS and F4-LS electrode montages are displayed in figure 1(b) and (c) respectively. The normalized arrows on figs 1(b) and (c) indicate current flow directions

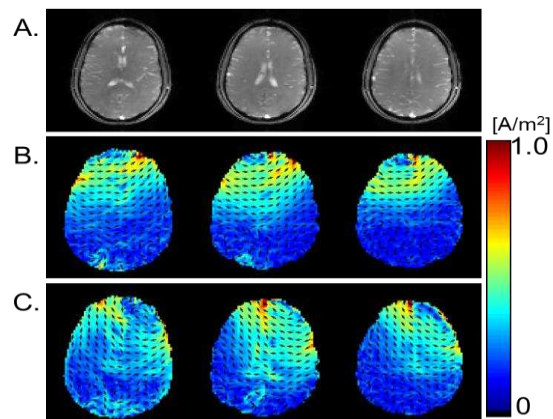


Figure 1: MR magnitude (A) and 5th iteration of reconstructed current density map inside the brain region for (B) F3-RS and (C) F4-LS montages at three slice locations (left to right).

4 Conclusions

Success of tDCS treatment depends on the current density distribution relative to brain anatomical structures. Our results shows that we can quantitatively visualize the current density distribution for off-plane distributions. We anticipate that quantitative visualization of the current density distribution in the brain will play an important role in monitoring tDCS treatments.

References

- [1] R J Sadleir *et al.* *NeuroImage*, 51:1310-8, 2010.
- [2] Kasinadhuni *et al.* *Brain Stimulation*, 10:764-72, 2017.
- [3] Kwon *et al.* *IEEE Trans Biomed Eng.*, 63:168-75, 2016

Comparison of in-vivo DT-MREIT scaling factor images for in- and off-plane current administration of transcranial AC stimulation.

Saurav Z K Sajib¹, Munish Chauhan¹, Aprinda Indahlastari¹, Aditya Kumar Kasinadhuni², Magdoom Kulam², Thomas Mareci², R J Sadleir¹

¹School of Biological and Health Systems Engineering, Arizona State University, Tempe, USA

²Biomedical Engineering, Biochemistry, University of Florida, Gainesville, USA rsadleir@asu.edu

Abstract: Diffusion tensor magnetic resonance electrical impedance tomography (DT-MREIT) aims to measure the anisotropic electrical conductivity distribution inside the human body. Previous work used DT-MREIT to measure the anisotropic conductivity distribution inside the brain using the current flows between approximately in-plane T7-T8 and Fpz-Oz electrode montages. In this work, we compare the anisotropic conductivity distribution found for these montages and non-coplanar F3-RS and F4-LS electrode montages using a realistic head model.

1 Introduction

DT-MREIT combines DTI and MREIT to produce images of anisotropic electrical conductivity tensors of body tissues. It is based on the assumed linear relationship between the conductivity (\mathbf{C}) and water diffusion tensor (\mathbf{D}) [1]. DT-MREIT reconstructions determine the scaling factor (η) images relating water diffusion tensors to measured magnetic flux density (B_z) data [2]. Recent work from Chauhan *et al.* [3] demonstrated anisotropic conductivity distribution reconstructed using pairs of surface electrodes attached to the head at EEG locations T7-T8 and Fpz-Oz configuration (in-plane). A remaining question in DT-MREIT is how results are affected by changes in electrode location, especially ‘off-plane configurations’. To answer this, we have numerically compared reconstructed scale factors and conductivity tensors for both types of electrode montage.

2 Methods

We constructed realistic computational head models from T1-weighted MR images of 160 slices with 1mm³ isotropic resolution. High angular resolution (HARDI) brain tissue anisotropy data was acquired using a subsequent DT-MRI scan. Eight tissue regions: skin, bone, muscle, fat, eyeball, grey matter (GM), white matter (WM) and cerebrospinal fluid (CSF) were segmented semi-automatically using FSL [3]. Two pairs of surface electrodes were attached to models at the T7-T8, and Fpz-Oz locations. Another model was constructed to simulate the F3-RS, F4-LS electrode montages.

We assigned isotropic conductivity values to skin (0.43 S/m), bone (0.015 S/m), muscle (0.20 S/m), fat (0.01 S/m) and eyeball (0.50 S/m) regions. For the brain tissues (GM, WM, CSF), we used experimentally obtained diffusion tensor data [3] and scaled water diffusion data to approximate electrical conductivity tensors, using scale factor values of (GM-0.37, WM-0.57 and CSF-0.32 S.sec/mm³). We then solved the Laplace equation for current densities, and generated simulated B_z data at five slice positions in the mid-brain using the Bio-Savart law.

In order to reconstruct scale factors η from simulated B_z data, we first recover the current density data as in [4],

$$\mathbf{J}^{n+1} = \mathbf{J}^n + \frac{1}{\mu_0} \left(\frac{\partial(B_z - B_z^n)}{\partial y}, -\frac{\partial(B_z - B_z^n)}{\partial x}, 0 \right) \quad (1)$$

where, \mathbf{J}^n, B_z^n are the computed current density vector and z-component of magnetic flux density data at n^{th} iteration. Using the iteratively updated current density data we then recovered scale factor images as in [2],

$$\nabla \ln \eta \times (\mathbf{D}^{-1} \mathbf{J}^{n+1}) = \nabla \times (\mathbf{D}^{-1} \mathbf{J}^{n+1}) \quad (2)$$

3 Results

Figure 1(a) and (c) display reconstructed scale factor images for the first slice position for T7-T8-Fpz-Oz and F3-RS-F4-LS electrode montages respectively. The respective diagonal components of the conductivity tensor are shown in figure 1(b) and (d). The relative L_2 error for the same slice position was found to be 0.121 for T7-T8-Fpz-Oz electrode montages whereas, for the F3-RS-F4-LS electrode montage this value was found 0.145.

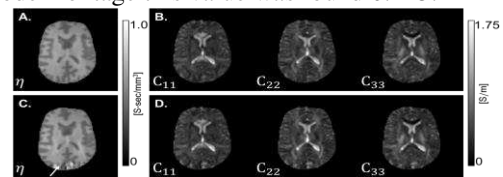


Figure 1: Reconstructed scale factor and diagonal components of reconstructed conductivity tensors relative to lab. frame for (top) in-plane and (bottom) off-plane montages.

4 Conclusions

Using numerical simulations, we found it is possible to reconstruct the conductivity tensor image for either in- or off-plane current injections. We also observed that the quality of reconstructed scale factor image deteriorated near boundaries (Fig. 1c). Because this study used a Harmonic- B_z type reconstruction algorithm [3], we speculate that this was due to the violation of the independence condition for the two current administrations. Practical considerations such as signal-to-noise ratio in imaged planes with different montages must also be considered. Moreover, while DT-MREIT can reconstruct conductivity tensor images, it requires two current injections. For practical application such as tDCS, DBS, or electroporation it may be desirable to develop method using one current injection only.

References

- [1] D S Tuch *et al.* *Proc. Nat. Acad. Sci.*, 98:11697-701, 2001.
- [2] O I Kwon *et al.* *Phys. Med. Biol.*, 59:2955-74, 2014.
- [3] M Chauhan *et al.* *IEEE Trans. Med. Imaging*, in press.
- [4] Kwon *et al.* *IEEE Trans Biomed Eng.*, 63:168-75, 2016.

Functional Magnetic Resonance Electrical Impedance Tomography of Salamander Retina

Fanrui Fu, Munish Chauhan, Rosalind Sadleir

Arizona State University. Email: rosaling.sadleir@asu.edu

Abstract: Functional Magnetic resonance electrical impedance tomography (fMREIT) is a potentially innovative technique for imaging neural activity. We tested fMREIT using a salamander retina as a neuronal activity source. We compared phase differences in MREIT imaging with and without light stimulation.

1 Introduction

Functional Magnetic resonance electrical impedance tomography (fMREIT) is a novel neural activity imaging technique [1-2] that involves application of small electrical currents to tissue. Conductivity changes in cell membranes during neural activity should be reflected in current flow patterns, causing differential phase accumulation in MR images. The salamander retina was used as a neural activity source in this study. We performed experiments where currents were applied synchronously with a light stimulus and compared these images with those collected without light stimulus, to determine if this activity could be detected in fMREIT phase images. A microelectrode array (MEA) was used to record the neuronal activity levels in between MREIT imaging protocols.

2 Methods

The retina was placed on a flexible multi-electrode array within a 3D-printed sample chamber. The sample chamber was then placed into an MR imaging probe within a small-bore 18.8T magnet. MREIT currents were introduced via 4 equally-spaced circular carbon electrodes attached to the wall of the sample chamber. Currents were applied using constant current source during the experiment, at an amplitude of $200\mu\text{A}$ and total pulse width of 18ms, between opposing pairs of electrodes. During data acquisition, current injection was synchronized with a multi spin echo MRI sequence [2] (figure. 1). A white LED was used for light stimulation. LED control signals were synchronized to the current source. Experiments were split into two sets — the first involving light stimulation, and the second without light. MREIT phase images for each experiment were obtained by complex dividing positive and negative current MRI data. A homogeneous area within the retinal tissue was chosen as region of interest (ROI). Standard deviations in phase data within the ROI were calculated and compared.

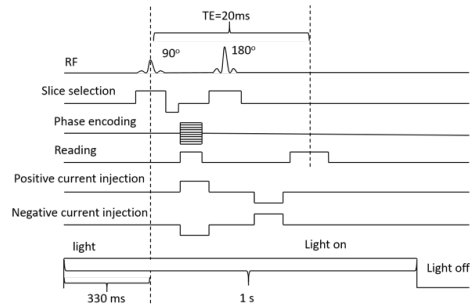


Figure 1: Spin-echo based MREIT sequence. The first 4 lines show the standard sequence and the following two lines represent MREIT current injections.

3 Result

The standard deviation of phase difference was found in the experiments (figure. 2), which could be caused by conductivity changes in retinal cell membranes.

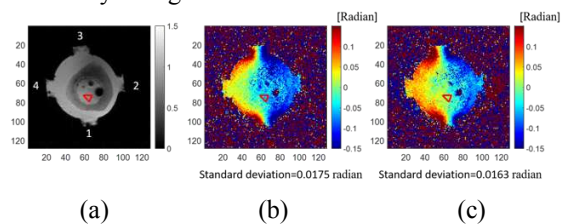


Figure 2: fMREIT imaging results. (a) Magnitude image showing retina in sample chamber. Electrode numbers are overlaid on the image. (b) Subtracted phase image with current injection via electrodes 1 and 3 with and (c) without light stimulation. ROIs used to calculate standard deviations are shown as red triangles.

4 Conclusion

MREIT is potentially useful for functional analysis since its contrast directly relates to neuronal activity. The application of current injection makes it an advanced method for studying effects of brain stimulation caused by neuromodulation techniques such as transcranial direct-current stimulation (tDCS) or deep brain stimulation (DBS).

References

- [1] Sadleir RJ, Grant S, Woo EJ. Can high-field MREIT be used to directly detect neural activity? Theoretical considerations. *NeuroImage* 2010;52(1):205-216.
- [2] Seo JK, Woo EJ. Magnetic resonance electrical impedance tomography (MREIT). *SIAM review* 2011;53(1):40-68.

Red Blood Cells Aggregability Measurement with Multiple-frequency Electrical Impedance Spectroscopy

Jianping LI¹, Daisuke Kikuchi¹, Madoka Koishi¹, Kiet Anh Tran¹, Achyut Sapkota², Masahiro Takei¹

¹Graduate School of Mechanical Engineering, Division of Artificial System Science, Chiba University, 1-33 Yayoi, Inage, Chiba, 263-8522 Japan; Email address: jianpingli2013@gmail.com

²Department of Information and Computer Engineering, National Institute of Technology, Kisarazu College, 2-11-1 Kiyomidai-Higashi, Kisarazu, Chiba, 292-0041 Japan

Abstract: Multiple-frequency electrical impedance tomography (EIS) is applied for the detection of red blood cells (RBCs) aggregability in blood extracorporeal circulation systems. RBCs aggregability is obtained in the pulsatile blood flow based on the multiple-frequency parameter (relaxation frequency f_c) from the Cole-Cole plot. From the experimental results, RBCs aggregability index A_G in coagulation blood is found to decrease during thrombus formation.

1 Introduction

Blood extracorporeal circulation systems, such as left ventricular assist devices (LVAD), extracorporeal membrane oxygenation systems (ECMO), are widely utilized in medical science. However, due to the application of artificial pumps and tubes, patients are always facing the critical threat of thrombosis [1]. Recently, RBCs aggregability has been reported to be related to thrombus formation, since RBCs are involved in the coagulation process by the presence of phospholipids on their surfaces, activating the factor IX and so on [2].

In this study, multiple-frequency electrical impedance spectroscopy is applied to monitor the RBCs aggregability in the blood extracorporeal circulation system. Relaxation frequency f_c is achieved from the Cole-Cole plot with the pulsatile flow, which is used to obtain the RBCs aggregability index A_G .

2 Methods

2.1 Experimental setup

The experimental setup is composed by one blood reservoir, one centrifugal blood pump, two pressure sensors, one impedance analyzer with four-terminal probes, one personal computer (PC), two electrodes, sampling ports, a syringe pump, a flow meter and blood circulation tubes. The impedance analyzer is connected with two stainless steel electrodes by four-terminal probes to measure the impedance of blood pulsatile flow. The PC is used to control the electrical impedance measurement system and save the data.

2.2 Experimental conditions

Fresh porcine blood with 1/10 tri-sodium citrate solution (3.28%) was used for the experiments. Calcium chloride solution (CaCl_2) was added to the extracorporeal circulation system to form the thrombus. Pulsatile blood flow was generated by changing the rotational speed of the centrifugal blood pump with a pulsatile period of 40 s. Flow rate was kept at 2.70 L/min during 24 s, and after that blood flow was suddenly stopped and maintained at 0 L/min for the remaining 16 s. The excitation current i was fixed at 0.1 mA. The impedance Z^* and shift phase θ

under the multiple-frequency from $f_1=100$ kHz to $f_2=300$ MHz (101 points, log scale) were measured continuously during the experiment. The relaxation frequency f_c was calculated by Cole-Cole plot using Z^* and θ data, according to our previous research [3].

3 Results and Conclusions

Fig. 2 shows the experimental results of relative relaxation frequency f_{cr} during thrombus formation. The relative relaxation frequency f_{cr} increases with the flow rate at the beginning, and it falls down in the case that flow stops. RBCs aggregability index A_G is defined as the ratio of relaxation frequency f_{cr} under $t_p=26$ s and $t_p=30$ s during the flow stop. RBCs aggregability index A_G of porcine blood is found to decline gradually from $A_G=1.13$ to $A_G=1.12$.

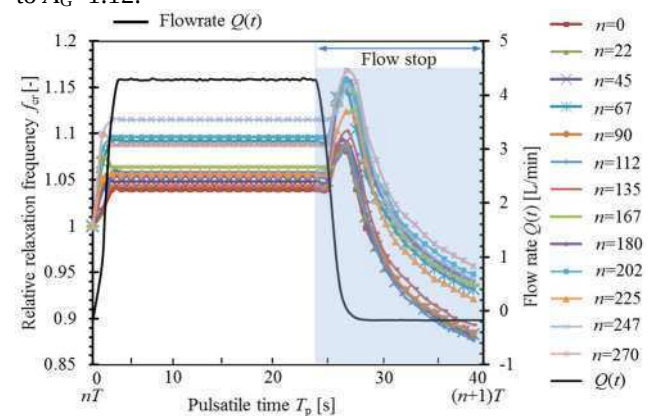


Figure 2: Experimental results of porcine blood with CaCl_2 solution

This study confirms the feasibility to the detection of RBCs aggregability using relaxation frequency decrement, and brings new insights for the development of on-line thrombus monitoring technology.

4 Acknowledgements

The work was supported by the Grant in Aid-For Scientific Research-A(16H02312), Grant in Aid-For Scientific Research for Young researchers (16K16394), JKA Ring-Ring Project, JSPS Bilateral Program for Japan-Vietnam and a research grant from Asahi Glass Foundation.

References

- [1] D. N. Huu, D. Kikuchi, O. Maruyama, A. Sapkota, M. Takei *Flow Measurement and Instrumentation*, 53: 172-179, 2017.
- [2] Copeland, Hannah, et al. "A method for anticoagulation of children on mechanical circulatory support." *Artificial organs* 35.11, 1018-1023, 2011.
- [3] Huu, D. Nguyen, et al. "Cole-cole analysis of thrombus formation in an extracorporeal blood flow circulation using electrical measurement." *Flow Measurement and Instrumentation*, 2016.

Biological specimen experimental results of an EIM system

Xiao-Qian Chen, Min Xu, Gerald Sze and Wei Wang

Micro Image Biotech Ltd, Cambridge, UK, w97wang@yahoo.co.uk

Abstract: This paper demonstrates the biological specimen experimental results that acquired from the MI-EIM-V1A system that adopts the planar electrode configuration. We have measured different number of quail eggs objects inside an agar phantom with a fixed depth of saline in 24 mm. Absolute and dividing image method have been used to demonstrate resulting reconstructed images.

1 Introduction

The MI-EIM-V1A system has been developed for breast cancer detection. Biological object experiment has been set up to demonstrate the abilities of distinguishing of different substances with different electrical properties.

2 Methods

2.1 Experimental setup

Setup of hardware system is listed as below:

- 85 planar electrodes configuration
- Injecting current in 20 kHz and 50 kHz
- Testing tank diameter is 159.5 mm with 24 mm depth, filled with test solution

2.2 The phantom

Quail eggs have been chosen as the testing objects, and the eggs are containing inside a concave agar breast model phantom. The phantom has been designed as below:

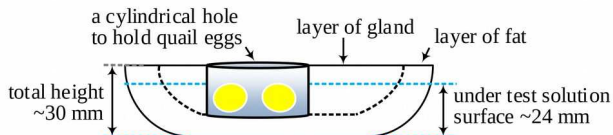


Figure 1: Side view image of agar breast model with quail eggs inside. Conductivities of testing solution is 500 $\mu\text{S}/\text{cm}$, fat and gland layers are 500 and 800 $\mu\text{S}/\text{cm}$ respectively, and whole quail egg object (egg white and yolk) is $> 2000 \mu\text{S}/\text{cm}$ at 50 kHz.

There are 3 different models set up for inserting the eggs into the agar phantom:

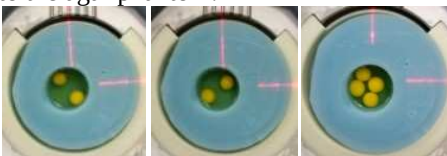


Figure 2: Top view of models from left to right: 01, 02 and 03.

2.3 3-D image reconstruction

The mesh for image reconstruction has 4 layers, and height of each layer is 6 mm. The actual position of the quail eggs should be laid between the second and fourth layers.

Images are reconstructed using in-house developed image reconstruction software with single-step method [1].

3 Results

The reconstructed images are analysed with two different methods: Absolute image in single frequency and dividing imaging by image-based frequency difference calculation. We expect to distinguish biological substances (corresponding to yolk which is a single, alive cell) from the non-biological substances (including egg white and agar container) in dividing imaging.

3.1 Reconstructed absolute conductivity images

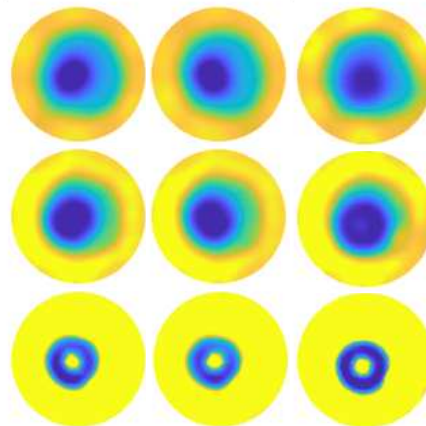


Figure 3: Top 3 layers (out of 4) of reconstructed absolute images in 50 kHz. Top layer is closest to testing tank surface. Models from left to right: 01, 02 and 03. Yellow indicates lower conductivity, while blue is higher. It can be seen that egg white has highest conductivity, while the centre of the object in second layer is considered as lower conductivity from absolute images.

3.2 Dividing imaging

Dividing image is calculated by dividing the reconstructed absolute conductivity values between two different frequencies pixel by pixel:

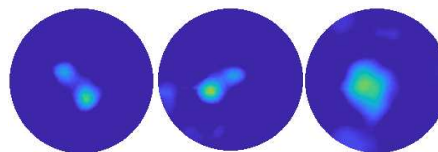


Figure 4: Dividing images of 20 kHz / 50 kHz from left to right: 01, 02 and 03; Layer being shown here is the 3rd layer from top.

The quail eggs could be separated from the dividing images while they are hidden in absolute images.

4 Conclusions

This paper presents basic diagnostic function of the MI-EIM-V1A system by using 2 frequencies in lower range. To realize human tissue diagnostic ability, the system is expected to measure impedance in higher frequency such as 5 MHz in order to extract individual tissues electrical properties.

References

- [1] G Sze, *Dissertation*, Univ. Sussex, 2012.

Investigation of Liver Fat Content Using a Bioimpedance Spectrum Measurement Method

Attila Toth¹, Zoltan Vizvari², Robert Adrian Gal^{1,3}, Andras Vereczkei³, Zoltan Karadi¹

¹University of Pécs, School of Medicine, Institute of Physiology, ²University of Pécs, Faculty of Engineering and Information Technology, Smart Technology Group, ³University of Pécs, Clinical Centre, Surgery Clinic

Abstract: Due to the lack of therapies for non-alcoholic fatty liver disease (NAFLD), there is a need for robust measurement for successful target identification, validation and assessment of therapies. Bioimpedance Spectrum (BIS) measurement is an excellent technique for early detection of NAFLD.

1 Introduction

Non-alcoholic fatty liver disease (NAFLD) is rapidly increasing in the general population of Western countries (NAFLD prevalence is 20-30%) and it is becoming the most common liver disease worldwide. It would be extremely important to develop a method for easy performance at the bedside or in the outpatient ward for evaluation of the risk of liver disease. Now the only technique that is generally used in the population is the liver ultrasonography, but it is known to underestimate the prevalence of fatty liver.

2 Methods

Liver BIS measurements were performed with four-electrode data collecting technique. Fig. 1. shows the self-developed data acquisition method, which includes the voltage generator, the reference resistor (10 kΩ) and a four channel voltage measurement device (lock-in amplifier). The application of this measurement method allows us to calculate the contact impedance (Z_{cont}) (1) and the bioimpedance (Z_x) (2). The frequency range of BIS measurements was 20 mHz – 90 kHz. Fig. 2. shows BIS data, which can be evaluated using the Cole-Cole model [1]. Although in higher frequency range ($f > 10$ Hz) our BIS results are consistent to the theoretical model, in lower frequency range the Cole-Cole model is inappropriate for modelling the BIS data.

2.1 Figures

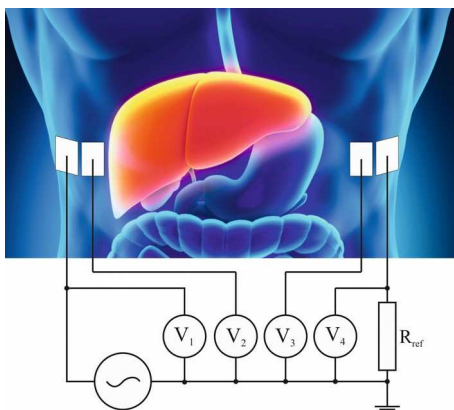


Figure 1: Measurement setup; electrodes placed on

the patient body

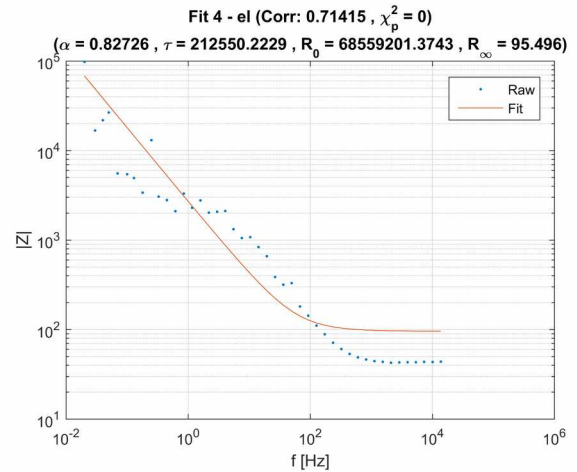


Figure 2: BIS measurement results

2.2 Equations

Calculation of contact impedance:

$$Z_{cont} = R_{ref} \cdot \frac{V_1 - V_4}{V_4} \quad (1)$$

Calculation of bioimpedance:

$$Z_x = R_{ref} \cdot \frac{V_2 - V_3}{V_4} \quad (2)$$

Cole-Cole equation:

$$Z(j\omega) = R_\infty + \frac{R_0 - R_\infty}{1 + (j\omega\tau)^\alpha} \quad (3)$$

where

τ is the time constant,

R_∞ is the resistance if $f \rightarrow \infty$,

R_0 is the resistance if $f \rightarrow 0$,

$\omega = 2\pi/f$

3 Conclusions

In our research work, we investigated liver fat content using BIS. It can be seen in Fig. 2. that the Cole-Cole model is less applicable to evaluate the BIS data. Thus, in order to achieve reliable measurements for the whole frequency spectrum, recently we are working on the modification of the theoretical model.

References

- [1] Cole, K., and Cole, R.: 'Dispersion an absorption in dielectrics', J. Chem. Phys., 1941,9, pp. 341–351

Effect of dispersion in nerve on impedance change: a modelling study

Ilya Tarotin^{*1}, Kirill Aristovich¹ and David Holder¹

¹Dept of Medical Physics and Biomedical Engineering, University College London, London, UK,
ilya.tarotin.14@ucl.ac.uk

Abstract: 3D Hodgkin-Huxley and C nociceptor 50-fibre nerve models with normally distributed propagation velocities were developed to characterise dispersion over distance of impedance (dZ) during action potential (AP) propagation. The area of compound APs decreased with distance due to their biphasicity, but that of dZ did not.

1 Introduction

EIT allows imaging fast impedance changes during neural depolarization in brain or nerves [1]. In peripheral nerve, recording more than 10cm from excitation is hindered by dispersion and phase cancellation of the externally recorded biphasic compound AP, as fibre conduction velocities vary. In contrast, dZ due to ion channel opening is only a monotonic decrease and so might be expected not to disperse with distance. The purpose of this study was to develop a model of multiple unmyelinated fibres with distributed propagation velocities to simulate the effect of dispersion on a dZ over frequency.

2 Methods

Nerve fibres were modelled as 1D cables in a 3D space using FEM. Each fibre contained active ion channels modelled via Hodgkin-Huxley (HH) [2] or HH-type C-fibre equations [3]. Membrane potential and external field were simulated simultaneously using the feedback coupling system so that extracellular APs could be recorded together with the intracellular ones. Current injection and recording of the electric field were undertaken through external electrodes. The main equations used in the model can be found in [4]. 50-fibre HH and C-fibre nerves were modelled; fibres were uniformly distributed in a cylinder with a diameter of 2.4 cm for HH axons and 0.01 cm for C fibres. Velocities of the fibres were randomized with normally distributed intracellular resistances. For C fibres, the mean r_i value was 0.0354 kOhm·cm and standard deviation of 0.005 kOhm·cm; for HH axons these values were 0.05 and 0.02 kOhm·cm respectively. The integral areas under the compound action potential and dZ curves were calculated at 10, 19, 25, 35, 45 cm for HH and 0.4, 0.8, 1, 1.4 cm for C fibre nerves from the AP initiation point

3 Results

The amplitudes of compound APs and dZs fell with the distance along the fibre (Fig. 1a-d) for both HH and C-fibre nerves as the separate action potentials spatially spread along the fibre. However, the area under the absolute values of the AP curve was found to decrease with distance due to cancellation as the AP is bipolar (Fig. 1e,f, blue dashed line). Conversely, the area under the dZ curve was constant although the amplitude fell similarly to the AP case (Fig. 1e,f, red solid line).

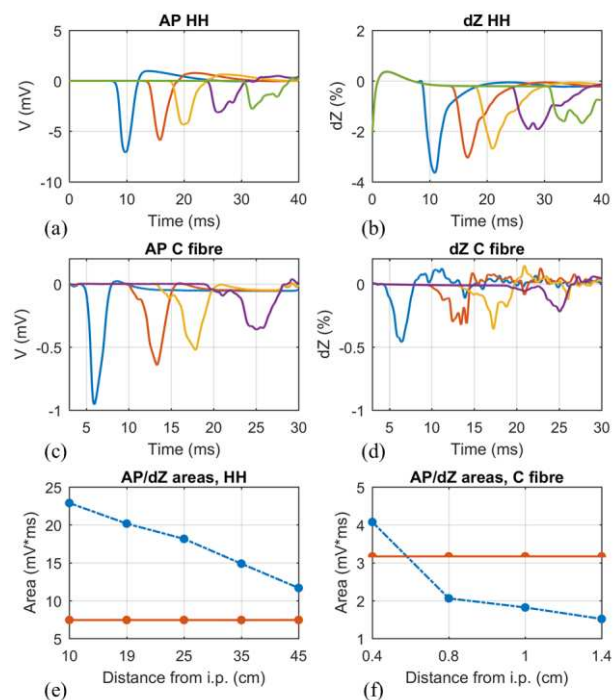


Figure 1: Compound APs and associated dZs of nerve consisting of 50 HH axons (left column) or 50 C fibres (right column) measured at different distances from the AP initiation point (HH: 10, 19, 25, 35 and 45 cm; C: 0.4, 0.8, 1 and 1.4 cm). (a), (c) – CAPs; (b), (d) – dZs; (e), (f) – integral areas under the CAPs (blue dashed lines) and dZ (red solid lines) vs distance from the AP initiation point (i.p.).

The CAP amplitude in the HH nerve fell by ~60% along 35 cm, but dZ fell by ~50%; the same was true for the C fibre: around 60% and 50% along 1 cm. This indicates that dZ is visible at greater distances from the initiation point than CAPs.

4 Conclusions

Dispersion of the evoked CAP in nerve provides a technical obstacle to recording activity at distances greater than a few cm for unmyelinated, and a few tens of cm for large myelinated fibres. This study confirms the expectation that the evoked impedance changes could be measured, or imaged with EIT, at greater distances than possible with CAP recording. This appears to be mainly because the impedance change is largely monophasic and so does not cancel as changes from individual nerves desynchronise.

References

- [1] K Aristovich et al. *Neuroimage*, 124:204–213,2016
- [2] AL Hodgkin, AF Huxley *J. Physiol* 117.4:500, 1952
- [3] J Tigerholm et al. *J Neurophysiol*, 111.9: 1721-1735, 2014
- [4] I Tarotin et al. *Conf 18th EIT*, p.43, Dartmouth University, Hanover, USA, June 2017

A modulated physical model for simulating regional ventilation with EIT

Christin Wenzel, Matthias Schneider, Sabrina Neugart, Stefan Schumann

Department of Anesthesiology and Critical Care, Medical Center – University of Freiburg, Faculty of Medicine, University of Freiburg, Germany, Christin.Wenzel@uniklinik-freiburg.de

Abstract: Aiming for simulating regional ventilation signals we have developed a physical modulated thorax model of conductible silicone including pressurizable chambers for modulation of the regional impedance. Such model could provide standard test conditions for EIT-algorithms.

1 Introduction

The major advantages of EIT over most other imaging methods in medicine are that EIT is i) applicable at the bedside, ii) radiation-free and iii) predestinated for imaging of the lungs. Consequently, thoracic EIT gives increasingly advanced insights into lung physiology during spontaneous breathing and mechanical ventilation. To our knowledge there are so far no physical models available for simulating regional with this technique. Aiming at simulating regional ventilation signals for EIT, we have developed a modulated physical model of the thoracic impedance. We hypothesized that this model allows simulating various conditions of regional ventilation with functional EIT.

2 Methods

The body of our physical model was manufactured of conductible silicone, consisting of base resin, conductive resin and diluting agent (Lianhuan Group, Shenzhen, China). The components were thoroughly mixed and the resulting compound filled into an oval form of 32 cm and 15 cm diameter. To model a reasonable ‘lung region’ by in the final form, open chambers were placed inside the non-cured silicone compound. After complete polymerization, the body of the model was taken from the form and the edges were carefully cut.

The holes in the ‘lung region’ were filled with elastic tubes of non-conductible silicone that were sealed on the one end and contained a connector for allowing pressure application on the other end. This way, by applying pressure to the elastic tubes, a certain force is applied to the material surrounding the respective hole, resulting in regional impedance changes. By connecting or disconnecting single holes from the respective pressure application, different regional behaviour could be generated. Data were collected at 20 frames per second.

2.1 Simulating shift in regional

By pressurizing subsets of the pressure tubes, we simulated various positions of regional ventilation. For generating the required regional impedance changes, the pressure tubes were connected to a piston pump.

3 Results

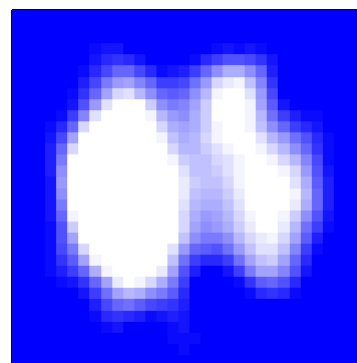


Figure 1: Simulated EIT image of bilaterally ventilated lung.

Simulations of regional lung ventilation (Fig. 1) could be generated using the model. Further, shifts in regional ventilation (lateral and ventral) and realistic global impedance curves during spontaneous breathing (Fig. 2) could be simulated with our model.

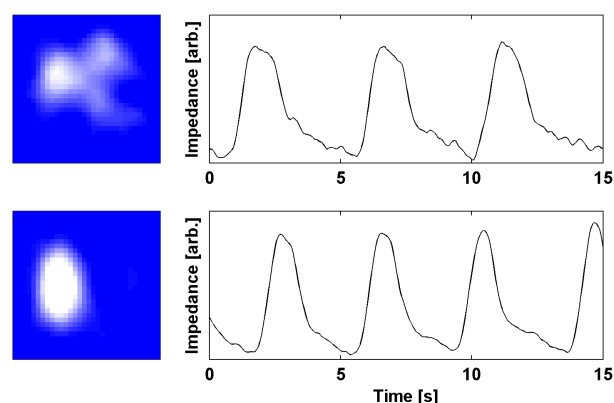


Figure 2: Regional ventilation (left) and global impedance curves during simulated ventrally shifted (top) and single-sided (bottom) ventilation.

4 Conclusions

The proposed model of the thoracic electrical impedance allows simulating various conditions of regional ventilation in the respiratory system. Such model could be utilized for generating standard test conditions for EIT-algorithms.

Intramuscular electrical impedance imaging using a needle device

Hyeuknam Kwon¹, Seward Rutkove¹, Benjamin Sanchez¹

¹Beth Israel Deaconess Medical Center, Boston, MA, USA, {hkwn1, bsanchez}@bidmc.harvard.edu

Abstract: We developed an “inside-out” static image reconstruction method from impedance measurements of human anisotropic muscle at rest using a needle device. We were able to discriminate healthy from neurogenic and myopathic muscle.

1 Introduction

Recent developments in magnetic resonance imaging (MRI) and ultrasound (US) techniques have enhanced the diagnosis and evaluation of neuromuscular disorders (NMD). However, both MRI and US have practical limitations. For example, MRI is time-intensive to complete and costly. US, on the other hand, requires considerable examiner experience to perform adequately.

One modality well-suited for evaluating muscle at rest is electrical impedance imaging (EII). However, perturbations in electrode position and boundary errors can cause image artifacts, and the resolution to detect internal structures in the muscle from surface recordings is limited at best (i.e. “outside-in” approach).

Here, we develop an “inside-out” EII reconstruction approach in which the electrodes are embedded within a needle device that is inserted into a muscle (fig. 1 A). The method consists of estimating the impedivity of anisotropic muscle to obtain the actual impedivity distribution. Then, the EII represents a volume surrounding the needle device and could potentially detect intrusions of fat deposition, connective tissue or regions of inflammation.

2 Methods

We developed a two-step EII reconstruction algorithm to visualize the impedivity distribution of muscle. The first step consists of estimating the longitudinal (L) impedivity $\hat{\kappa}_L := \hat{\alpha} \hat{\kappa}_\alpha$ (Ω m) and transverse (T) impedivity $\hat{\kappa}_T := \hat{\kappa}_\alpha / \hat{\alpha}$ (Ω m) of anisotropic muscle from vertical impedance measurements (fig. 1 B), where $\hat{\kappa}_\alpha$ and $\hat{\alpha}^2$ are the estimated geometric mean impedivity (Ω m) and the estimated anisotropy ratio (dimensionless) of muscle, respectively, defined as

$$\begin{cases} \hat{\kappa}_\alpha := \frac{1}{D} \sum_{n=1}^D Z_n K d \\ \hat{\alpha}^2 := \frac{1}{D} \sum_{n=1}^D \frac{1}{\cos^2 A_n} \left[\frac{(2\hat{\kappa}_\alpha d_e)^2}{4r^2 \sin^2 B(Z_n K d + 2\hat{\kappa}_\alpha)^2} - \sin^2 A_n \right], \end{cases}$$

with Z_n the measured impedance (Ω) using the n th electrode configuration, $K = 4\pi$ is a scaling factor (dimensionless), d_e is electrode depth distance (m), D is the number of electrodes within the same plane, r is the needle radius, $A_n := (\theta_n + \theta_{n+1})/2$ and $B := (\theta_n - \theta_{n+1})/2$.

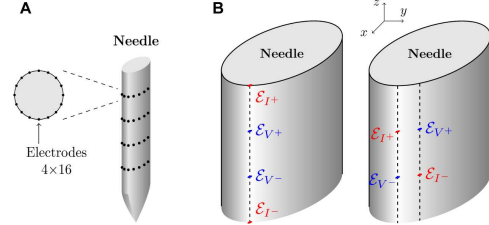


Figure 1: Rendering of a needle device with 4×16 electrodes on the shaft. $\mathcal{E}_{I\pm}$ and $\mathcal{E}_{V\pm}$ denote the current (red) and voltage (blue) electrodes, respectively.

In the second step, we measure the impedance data using the conventional rotation scheme. Finally, image reconstruction is then formulated as a linear least-squares model-fitting problem.

3 Simulation results

We validate our method using numerical simulations using Comsol Multiphysics (Comsol, Inc., Burlington, MA, USA). We evaluated both muscle with chronic neurogenic disease (CND) with associated fat deposition (fig. 2 A) and acute inflammatory myositis (IM) with scattered inflammatory infiltrates in the muscle (fig. 2 B). In CND muscle, fat deposition was simulated with less conductive regions as compared to areas of healthy muscle tissue. Pockets of inflammation in IM muscle were simulated with intrusions of more conductive regions in the muscle, whereas the surrounding tissue was simulated as healthy muscle [1, 2].

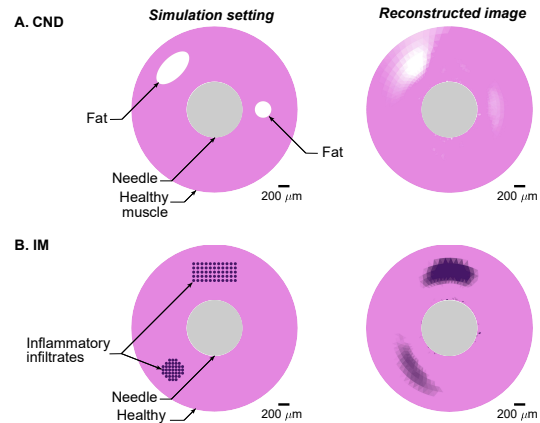


Figure 2: Impedance image for muscle with chronic neurogenic disease (CND) (A) and inflammatory myositis (IM) (B).

4 Conclusions

Static EII using a needle device can detect microscopic alterations in muscle composition, thus having potential for evaluation of NMD.

References

- [1] D Andreuccetti, R Fossi, C Petrucci *IFAC-CNR, Florence (Italy)*, 1997 (Available: <http://niremf.ifac.cnr.it/tissprop/>)
- [2] H Kwon, J Nagy, R Taylor, S Rutkove, B Sanchez *Phys. Med. Biol.*, 62(22):8616–8633, 2017

A Coupled US/EIT System for Assessing Muscle Health

Ethan K. Murphy¹, Joseph Skinner¹, Maria Martucci², Seward Rutkove² and Ryan Halter^{1,3}

¹Thayer School of Engineering, Dartmouth College, Hanover, NH, ethan.k.murphy@dartmouth.edu

²Beth Israel Deaconess Medical Center, Boston, MA, USA srutkove@bidmc.harvard.edu

³Geisel School of Medicine, Dartmouth College, Hanover, NH, USA

Abstract: Our initial patient study of a combined ultrasound (US) and Electrical Impedance Tomography (EIT) system on a small cohort of patients has shown significant differences between longitudinal and transverse muscle fibre conductivity reconstructions – *an important validation test* – and has shown a capability to distinguish healthy from diseased tissue.

1 Introduction

Electrical Impedance Myography (EIM) has shown significant promise as a diagnostic tool capable of distinguishing healthy from diseased muscle tissue in a number of neuromuscular diseases [1]. Electrical Impedance Tomography (EIT) has the potential to enhance EIM and improve the clinical value by providing reconstructions that spatially map the EIM signatures and specifically 1) properly account for variations in skin/subcutaneous fat layers across patients and 2) differentiate contributions from different muscles within the tissue volume interrogated. This study presents a coupled ultrasound (US) and EIT system used to record data from a small cohort of patients.

2 Methods

A combined US/EIT system (Fig. 1A-B) was used to record measurements on both legs from a small cohort of patients (4) who had a neuromuscular disorder affecting at least one side. Repeated, longitudinal and transverse data were acquired from a total of nine sites. Data corresponding to each measurement consisted of the US image and EIT voltages. Segmented tissues from the US images were used to construct Finite Element Method (FEM) meshes and the regularization matrix of the forward and inverse problems, respectively.

The inverse algorithm relied on a standard Gauss-Newton approach employing generalized Tikhonov regularization. The error function is given by

$$E(\delta\sigma) = \|\mathbf{J}\delta\sigma - \Delta\mathbf{v}\|_2^2 + \lambda\|\mathbf{L}(\sigma_0 + \delta\sigma - \sigma_{REF})\|_2^2 \quad (1)$$

where $\delta\sigma$ is the conductivity update, \mathbf{J} is the Jacobian, \mathbf{L} is the regularization matrix, λ is the Tikhonov regularization factor, σ_{REF} is a reference conductivity, and $\Delta\mathbf{v}$ is the vector difference between measured, \mathbf{v}_{Meas} , and simulated voltages, $\mathbf{v}_{Sim}(\sigma_0)$. Soft-regularization is implemented by assigning muscle, skin/subcutaneous fat, and US gel conductivity values (from literature) of σ_{REF} based on the location of each component. The \mathbf{L} -matrix was diagonal with entries equal to the sensitivity of each inverse voxel. Absolute reconstructions were performed using 5 iterations and Tikhonov parameter of $1e5$ on frequencies of 10, 20, 40, and 80 kHz. The regularization approach is similar to that used in [2].

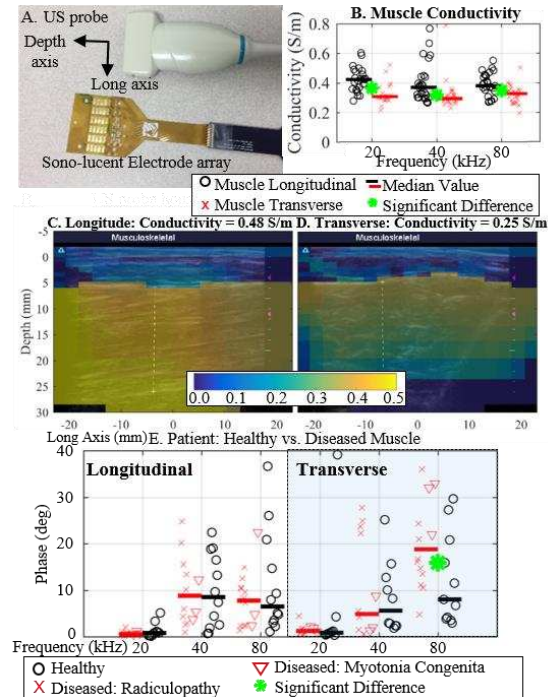


Figure 1: The combined system was composed of the A. the US probe and sono-lucent electrode array. B. Longitudinal reconstructions were found to be larger (with significance) than transverse (example C-D). E. The phase at 80 kHz showed an ability to distinguish healthy from diseased tissue.

Significant differences between longitudinal and transverse muscle reconstructions were found at frequencies of 20, 40, and 80 kHz (Fig. 1B). Example longitudinal and transverse EIT reconstructions from a single site overlaid on their respective US images (Fig. 1C-D) shows the expected result of a larger conductivity in the longitudinal direction. Significant differences between healthy and diseased tissue were observed at 80 kHz for permittivity and phase values of the transverse cases (Fig. 1E).

3 Conclusions

This is the first study of a combined US/EIT system showing an ability to obtain clinically relevant information on muscle condition. We hope to make minor modifications to the system and perform a larger clinical study.

4 Acknowledgements

This work was supported in part by the DoD CDMRP Grant W81XWH-15-1-0102.

References

- [1] Rutkove, *Muscle and Nerve*, 40(6): 936–946, 2009
- [2] Brooksby, et al *IEEE J Sel Top Quantum Electron*, 9(2): 199-209, 2003

EIT Image-Based Bladder State Classification for Nocturnal Enuresis

Eoghan Dunne, Adam Santorelli, Brian McGinley, Martin O'Halloran,
Geraldine Leader and Emily Porter

Translational Medical Device Lab, National University of Ireland Galway, e.dunne13@nuigalway.ie

Abstract: In this paper, we propose the use of electrical impedance tomography (EIT) to support children with nocturnal enuresis. We perform the first image-based threshold classification for determining the bladder state of 'not full' or 'full'. The results demonstrate the strong promise for EIT as an aid for nocturnal enuresis.

1 Introduction

Nocturnal enuresis (also known as bedwetting or NE) is a common childhood condition with an overall prevalence between 9-12 % [1]. Where the condition is associated with daytime lower urinary tract symptoms, NE can constitute up to 40 % of paediatric urology clinic visits [2]. The impact of NE on the child is both medical and psychological, severely degrading a child's quality of life [3].

Common treatments include pharmacological therapies and devices that alert after urination has occurred [4]. These treatments are reactive and have high relapse or discontinuation rates [4, 5].

Electrical impedance tomography (EIT) is a low-cost, portable, and non-invasive medical technology that can be used to determine the bladder volume of patients [6]. The technology offers the potential to proactively treat nocturnal enuresis in children.

Image-based classification allows the bladder volume to be determined. Image segmentation [7] and metrics such as the average conductivity index [8] and global impedance [7] have been previously related to bladder volume using EIT. However, for NE, the exact bladder volume does not need to be determined; it is only necessary to detect when the bladder is nearing full. In this paper, we perform the first image-based threshold classification in bladder monitoring using EIT to determine the bladder state of 'full' or 'not full'.

2 Methods

The electrical impedance dataset from Dunne *et al.* [9], with varying signal-to-noise ratio (SNR) and bladder volume, formed the basis for the image dataset in this paper. Using a SNR of 40 dB (one of the lower SNRs for existing EIT hardware [10]) and the GREIT image reconstruction algorithm [11], 99 2D noisy images were formed with a non-noisy reference image of an empty bladder (40 ml bladder). The bladder volumes used were {60:40:260, 280, 300:20:420} ml. The boundary between full and not full bladder volume was taken as 300 ml. The mean pixel intensity was then calculated for each image.

3 Results & Discussion

The bladder states of full and not full can be separated based on the mean pixel intensity alone, as shown in Figure 1. While some overlap is present in the distributions, multiple thresholds may be used to refine the

certainty of predicting full or not full bladders. Probabilistic machine learning may then be used within the uncertainty region to improve performance. The performance of the mean pixel intensity for threshold classification is shown in the receiver operating characteristic (ROC) curve in Figure 2, demonstrating that a good trade-off between true positive and false positive rates can be achieved.

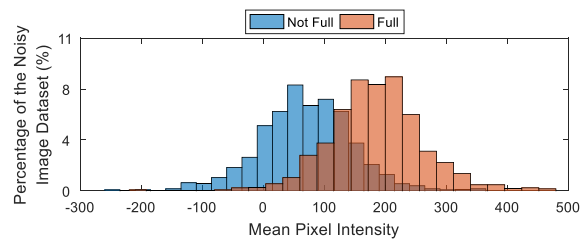


Figure 1: A histogram comparing the mean pixel intensity of each image for the two types of classifications: a not full bladder (blue) and a full bladder (orange).

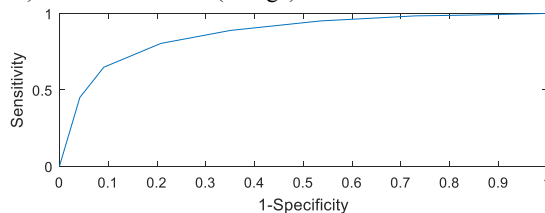


Figure 2: ROC curve for threshold classification using the mean pixel intensity of the reconstructed images.

4 Conclusions

This paper has proposed the use of EIT for support of nocturnal enuresis, and has shown that simple threshold classification based on reconstructed bladder images can be used to predict the bladder state of 'full' or 'not full'.

5 Acknowledgements

This research was supported by the European Research Council under the European Union's Horizon 2020 Programme/ ERC Grant Agreement BioElecPro n. 637780 and the charity RESPECT and the People Programme (Marie Curie Actions) of the European Union's Seventh Framework Programme (FP7/2007-2013) under REA Grant Agreement no. PCOFUND-GA-2013-608728.

References

- [1] H Sarici, *et al. J. Pediatr. Urol.* 12(3): 159:e1-e6, 2016.
- [2] W Farhat, *et al. J.Urol.* 164(3):1011-5, 2000.
- [3] J P Norgaard, *et al. BJU* 79(6):825-836, 1997.
- [4] N Tu and L Baskin *UpToDate* 1-13, 2016
- [5] S Thompson and J Rey *J. Am. Acad. Child. Adolesc. Psychiatry* 34(3):266-271, 1995
- [6] S Leonhardt, *et al. Biomed. Eng.*56(6):301-7, 2011.
- [7] T Schlebusch, *et al. Physiol. Meas.* 35(9):1813-23, 2014.
- [8] R Li, *et al. J. Med. Biol. Eng.* 36:71-9, 2016.
- [9] E Dunne, *et al. Sci. Rep.* 8:1-12, 2018
- [10] A McEwan, *et al. Physiol. Meas.* 28(7):S197:S215, 2007.
- [11] A Adler, *et al. Physiol. Meas.*, 30(6):35-55, 2009.

3D cell spheroids drug response monitoring using electrical impedance tomography

Hancong Wu¹, Yujie Yang¹, Pierre O Bagnaninchi² and Jiabin Jia¹

¹School of Engineering, The University of Edinburgh, Edinburgh, UK, jiabin.jia@ed.ac.uk

²MRC Centre for Regenerative Medicine, The University of Edinburgh, Edinburgh, UK

Abstract: This work explores a novel electrical impedance imaging technique to monitor the drug responses of 3D cell spheroids in real-time. Reconstructions were compared between the cell culture with and without drug for the visualization of cell mortality.

1 Introduction

3D cell spheroids provide more convincing testing data than the 2D monolayer cells in the anticancer drug discovery and development [1]. However, current methods for 3D drug response monitoring are limited and they are either destructive or time-consuming. The miniaturised electrical impedance tomography (EIT) method is proposed that can non-invasively reconstruct the drug response of a cell spheroid in real-time. Previous work has demonstrated its feasibility in the image reconstruction of small spheroids [2]. The objective of this work is to demonstrate the application of EIT in the real-time monitoring of drug responses in 3D cell spheroids and its potential in drug evaluation.

2 Methods

2.1 Experiment design

The MCF-7 breast cancer cell spheroids with 1.2 mm radius were cultured and formed as the objects under test using the liquid overlay method. Triton X-100 lysis buffer was added to the culture medium composed of Dulbecco's Modified Eagle Medium (DMEM) and fetal bovine serum (FBS) to prepare the 2% Triton X-100 solution, which can cause cell death in a short time by solubilizing the cell membrane proteins. Two experimental groups were set in this study. Two miniature circular EIT sensors with 7.5 mm radius filled with 2% Triton X-100 solution and culture medium separately. The MCF-7 spheroids were introduced to both sensors simultaneously and the boundary voltage variations were recorded for 30 minutes continuously with the biomedical EIT system developed at the University of Edinburgh [3].

2.2 Image reconstruction and data analysis

In order to evaluate the effect of the drug to the spheroids, reference for the image reconstruction was taken at the time when the spheroids were introduced to the sensor. Since the spheroid is small, the iterative Basis Pursuit Denoise model [4] was adopted in the image reconstruction to improve the image quality. Figure 1 shows the conductivity variation of the spheroid over 30 minutes after it was placed into the drug. It can be seen that the conductivity of the spheroid in the 2% Triton X-100 solution increased over time while the conductivity of the spheroid in the normal culture medium remained unchanged during the experiment. It means that the conductivity of the spheroids does not have a significant change in the culture medium. Whereas, the Triton X-100 solution caused the destruction of the low conductive cell membranes. The increase of the spheroid conductivity continues for 20 minutes. Hence, it can be concluded that the drug response lasted for 20 minutes until all the cells in the spheroid lost their viability.

3 Conclusions

A drug response experiment with the tumour spheroids was conducted and monitored by the EIT in real-time. EIT can reconstruct images of the delicate conductivity variation in the small spheroids and it also provides the temporal information of the cell drug response. Therefore, it has the potential to be applied to the real-time non-invasive 3D monitoring in drug discovery applications.

References

- [1] V. Koshkin, L. E. Ailles, G. Liu, and S. N. Krylov, *Journal of cellular biochemistry*, vol. 117, pp. 59-65, 2016.
- [2] Y. Yang, H. Wu, and J. Jia, *Conf 18th EIT*, Dartmouth, Hanover, New Hampshire, USA, 2017.
- [3] Y. Yang and J. Jia, *Review of Scientific Instruments*, vol. 88, p. 085110, 2017.
- [4] E. Van Den Berg and M. P. Friedlander, *SIAM Journal on Scientific Computing*, vol. 31, pp. 890-912, 2008.

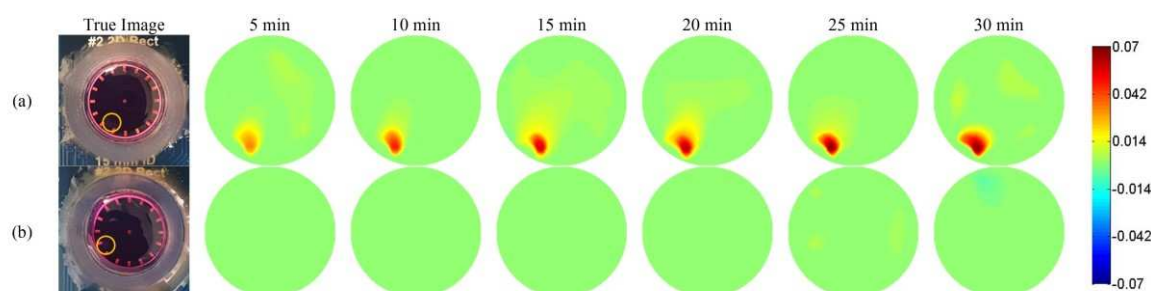


Figure 1: Reconstructed images for the spheroids in (a) 2% Triton X-100 solution and (b) culture medium.

Development of Multiple Electrodes based Impedance Spectroscopy for Screening of Cervical Dysplasia and Cervical Cancer

Tong In Oh^{1,2}, You Jeong Jeong², Hyun Tae Choi², and Eung Je Woo^{1,2}

¹School of Medicine, Kyung Hee University, Seoul, Republic of Korea, tioh@khu.ac.kr

²Department of Medical Engineering, Graduate School, Kyung Hee University, Seoul, Republic of Korea

Abstract: The probe with a circular array of electrodes and impedance spectroscopy system were developed to show the feasibility of screening tool for high grade cervical intraepithelial neoplasia (CIN) in women. Excised four CIN3 cervical tissue samples and two normal samples had difference in the reconstructed resistivity.

1 Introduction

Cervical cancer is the second most common cancer among women in the world. In Korea, it was ranked 7th among female cancer patients (15.1 per 100,000 population, 2009), but it was much higher than in G20 countries [1]. Korean government recommends the cervical cancer screening every other year for women over 20 years old. However, current diagnostic methods such as PAP smear, biopsy, colposcopy and conization have limitations for simply examination, non-invasively. Since the highly stratified structure of cervical epithelium is changed as the cervical dysplasia progresses, the impedance spectrum will be different shape depending on the CIN grades. Previously, Brown *et al.* presented the potential of cervical impedance spectrometry as screening tool when doing colposcopy examinations [2]. In this study, we developed the new impedance spectroscopy with multiple electrodes and applied the localized electrical energy concentration algorithm to reconstructed resistivity in the probing region [3,4].

2 Methods

In order to reduce the negative sensitivity induced by the four-electrode measurement method and the influence of the surrounding tissue due to the current diffusion, we used multiple small electrodes on the surface of probe with localized energy concentration algorithm. Fig.1 shows the developed impedance spectroscopy system with 10 mm probe including 16 small electrodes which arranged at regular intervals on two circles except of the reference electrode located at the centre. To select any four electrodes among the multiple electrodes, the measurement system consists of switching module and two IMM modules including one ground-type constant current source and a differential voltmeter.



Figure 1: Impedance spectroscopy with multiple electrode probe and excised cervical tissue (normal case).

We evaluated the feasibility of developed impedance spectroscopy system as a tool for the examination of cervical dysplasia and cervical cancer with the excised cervical tissue during conization. After conization, the impedance spectrum in the frequency range of 1-100 kHz was measured by injecting a current of 85-305 μ A. Also, the extracted tissue was examined by pathology to confirm the CIN grade. The difference of the reconstructed resistivity spectrum as shown in Fig. 2 was obtained by measurements for two normal subjects and four CIN 3 grade patients.

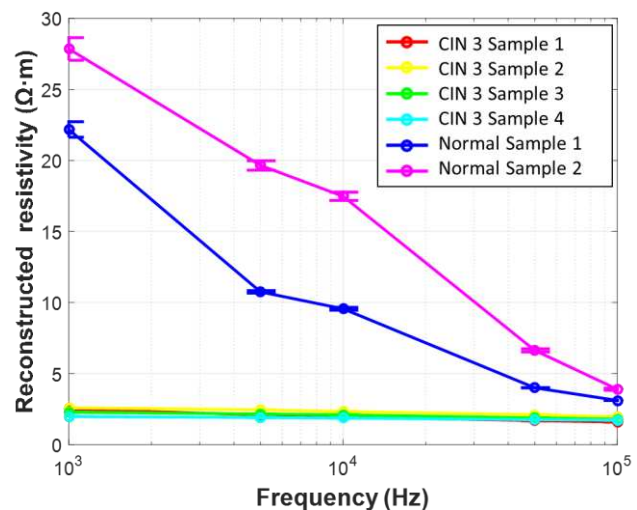


Figure 2: Reconstructed resistivity for four CIN3 samples and two normal samples (@ 1 – 100 kHz).

3 Conclusions

We developed the new impedance spectroscopy with multiple electrodes probe for examining the state of cervical tissue. The impedance spectral measurements from the excised female cervix in CIN3 and normal subjects corresponded with the predictions from the numerical simulations [5].

4 Acknowledgements

Research supported by Kyung Hee University, Republic of Korea (20170836).

References

- [1] Korea Central Cancer Registry, Ministry of Health and Welfare, Republic of Korea, 2009
- [2] BH Brown, P Milnes, S Abdul, JA Tidy *BJOG: An International Journal of Obstetrics & Gynaecology* 112.6: 802-806, 2005
- [3] H Kwon, H Wi, B Karki, EJ Lee, A McEwan, EJ Woo, B Harrach, JK Seo, TI Oh *Electronics letters* 48.20: 1253-1255, 2012
- [4] B Karki, H Wi, A McEwan, H Kwon, TI Oh, EJ Woo, JK Seo *Measurement Science and Technology* 25.7: 075702, 2014
- [5] L Balasubramani, BH Brown, J Healey, JA Tidy *Gynecologic oncology* 115.2: 267-271, 2009

Accelerating Space-Time Regularized Reconstructions

Andy Adler¹ and Kirill Aristovich²

¹Carleton University, Ottawa, Canada

²University College London, UK

Abstract: Most modern reconstruction algorithms for EIT use regularization, using a penalty to impose spatial smoothness. Several approaches exist to also impose temporal smoothness. Here, we formulate spatio-temporal reconstruction in a simpler way that helps clarify the impact of parameter choices.

1 Introduction

First, we introduce notation for spatial and then spatio-temporal (S-T) regularized time difference EIT reconstruction. S-T reconstruction can be formulated in (a) two stages (spatial then temporal) [3], (b) via an augmented S-T matrix [1], or (c) as a Kalman smoother [2]. Here we extend (b) to provide a simplified and efficient calculation.

Regularized time-difference EIT image reconstruction, seeks \hat{m} , an optimum image m , to minimize the norm

$$\|d - Sm\|_{\Sigma_n^{-1}} + \|m - m_0\|_{\Sigma_x^{-1}} \quad (1)$$

for data d , and sensitivity matrix S . Measurement noise is Gaussian $\sim \mathcal{N}(0, \Sigma_n)$, and the image $\sim \mathcal{N}(m_0 = 0, \Sigma_x)$.

Using $\Sigma_n^{-1} = W^t W$, and $\Sigma_x^{-1} = \lambda L^t L$, we introduce auxiliary (“whitened”) data, y , and image, x .

$$\hat{m} = L^{-1} \hat{x}, \quad \hat{x} = (J^t J + \lambda I)^{-1} J y, \quad y = W d \quad (2)$$

where $S = W^{-1} J L$. This may be seen from the solution to (1), $\hat{m} = (S^t \Sigma_n^{-1} S + \Sigma_x^{-1})^{-1} S^t \Sigma_n^{-1} d$, and thus $\hat{x} = L [L^t (J^t W^{-t} \Sigma_n^{-1} W^{-1} J + \lambda I) L]^{-1} L^t J^t W^{-t} \Sigma_n^{-1} W^{-1} y$.

A matrix formulation of S-T regularization solves an augmented-matrix forward problem, $\tilde{y} = \tilde{J} \tilde{x}$,

$$\tilde{x} = \begin{bmatrix} x_f \\ x_c \\ x_p \end{bmatrix}, \quad \tilde{y} = \begin{bmatrix} y_f \\ y_c \\ y_p \end{bmatrix}, \quad \tilde{J} = \begin{bmatrix} J & 0 & 0 \\ 0 & J & 0 \\ 0 & 0 & J \end{bmatrix} = I \otimes J, \quad (3)$$

where f, c, p are future, current and past frame values, with respect to the reconstruction frame of interest. Here $\tilde{\Sigma}_n = I \otimes \Sigma_n$ (since noise is independent between frames) and $\tilde{\Sigma}_x = \Gamma \otimes \Sigma_x$, where Γ is symmetric with diagonal 1 and decreasing off-diagonal values. For example

$$\Gamma = \begin{bmatrix} 1 & \gamma & \gamma^2 \\ \gamma & 1 & \gamma \\ \gamma^2 & \gamma & 1 \end{bmatrix}, \quad \Gamma^{-1} = \frac{1}{1-\gamma^2} \begin{bmatrix} 1 & -\gamma & 0 \\ -\gamma & 1+\gamma^2 & -\gamma \\ 0 & -\gamma & 1 \end{bmatrix} \quad (4)$$

where $0 \leq \gamma < 1$ represents the correlation between frames, and Γ^{-1} is tri-diagonal. The S-T reconstruction is thus

$$\tilde{x} = (I \otimes J^t J + \Gamma^{-1} \otimes \lambda I)^{-1} (I \otimes J^t) \tilde{y} = \tilde{R} \tilde{y}, \quad (5)$$

where \tilde{R} is the augmented S-T reconstruction matrix. This S-T inverse matrix grows large with the number of frames.

2 Spatio-temporal inverse

The relation $(I + \delta)^{-1} = I - \delta + \delta^2 \dots$ (valid when the largest eigenvalue of δ is < 1) may be used to simplify (5).

$$\begin{aligned} \tilde{R} &= (I \otimes (J^t J + \lambda I) + (\Gamma^{-1} - I) \otimes \lambda I)^{-1} (I \otimes J^t) \\ &= (I \otimes M^{-1} + D \otimes \lambda I)^{-1} (I \otimes J^t) \\ &= ((I \otimes M^{-1})[I + (I \otimes M)(D \otimes \lambda I)])^{-1} (I \otimes J^t) \\ &= (I + D \otimes \lambda M)^{-1} (I \otimes M^{-1})^{-1} (I \otimes J^t) \\ &= (I + \delta)^{-1} (I \otimes M)(I \otimes J^t) \\ &= (I - \delta + \delta^2 - \dots) (I \otimes M J^t) \\ &= I \otimes M J^t - \lambda D \otimes M^2 J^t + (\lambda D)^2 \otimes M^3 J^t - \dots \end{aligned} \quad (6)$$

where $M = (J^t J + \lambda I)^{-1}$, $D = \Gamma^{-1} - I$ and $\delta = \lambda D \otimes M$. Reconstruction in (6) is first a spatial inverse, followed by temporal smoothing terms, where each time step is successively “filtered” by λM . Contributions from the past and future are thus blurred both in time and space.

Using the singular-value decomposition, $J = U \Sigma V^t$, and $M = V(\Sigma^2 + \lambda I)^{-1} V^t$. Thus each k^{th} term $M^k J^t = V(\Sigma^2 + \lambda I)^{-k} \Sigma U^t$. Finally, the S-T image at frame t , $\tilde{m}_t = L^{-1} \tilde{x}_t$ can be calculated from post-filtering spatial-only images \hat{x}_{t+i} at offsets i from the current frame, as

$$\tilde{x}_t = \hat{x}_t - \sum_{i=-T}^T ([\lambda D]_i M + [(\lambda D)^2]_i M \dots) \hat{x}_{t+i} \quad (7)$$

where $[D]_i$ represents the i^{th} offset on the centre row; for $D \in \mathbb{R}^{2T+1 \times 2T+1}$, $[D]_i$ is the $(T+1, T+1+i)^{\text{th}}$ element.

3 Results and Discussion

Fig. 1 shows sample results. An S-only reconstruction performs equally for moving and still targets, but with worse noise. Using temporal, then spatial regularization [3] offers improvements, like the S-T solution shown last, but the moving target is blurred in space.

In conclusion, we develop an efficient formulation for the S-T regularization of [1]. This approach clarifies how temporal regularization results in blurring in both space and time for each time-offset. This differs from successive S then T regularization [3], which does not introduce the additional S blur.

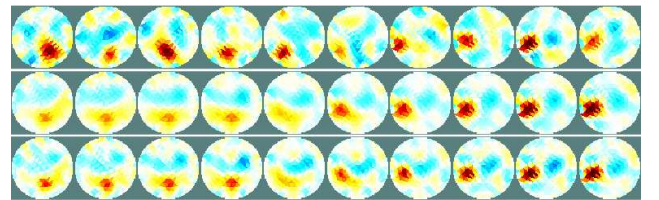


Figure 1: Images of a rotating contrast (with added noise) which stops at the 7th frame. *Top:* Spatial-only solution *Middle:* Temporal then spatial solution, *Bottom:* S-T solution, via (7)

References

- [1] A Adler, T Dai, WRB Lionheart, *Physiol Meas* 28:S1-S11, 2007.
- [2] M Vauhkonen, PA Karjalainen, JP Kaipio, *IEEE T Biomed Eng* 45:486-493, 1998.
- [3] RJ Yerworth, I Frerichs, R Bayford, *J Clin Monit Comput* 31:1093-1011, 2017

Sequential EIT Frame Reconstruction Exploiting Spatiotemporal Correlation

Shengheng Liu and Jiabin Jia

School of Engineering, The University of Edinburgh, Edinburgh, UK, Jiabin.Jia@ed.ac.uk

Abstract: Multiple high-resolution electrical impedance tomography frames are reconstructed within a sparse Bayesian learning framework. Both intra-frame spatial clustering and inter-frame temporal continuity are learned and exploited in an unsupervised manner by using hierarchical Bayesian model and structure-aware priors.

1 Introduction

To facilitate accurate, low-cost, and prompt-response diagnosis in emergency scenarios, fast and high-spatiotemporal-resolution Electrical impedance tomography (EIT) is in high demanding. We expand upon previous sparse Bayesian learning (SBL) based method [1, 2] in this work, and reconstruct sequential EIT frames with an enhanced resolution.

2 Methods and Test Results

The inverse model for simultaneously recovering multiple frames can be expressed as

$$\Delta \mathbf{Y}_{N \times L} = \mathbf{J}_{N \times M} \Delta \mathbf{K}_{M \times L} + \mathbf{V}, \quad (1)$$

where \mathbf{J} is the Jacobian matrix. $\Delta \mathbf{Y}$, $\Delta \mathbf{K}$, and \mathbf{V} are the matrices respectively containing the differential measurement vectors, conductivity change frames, and noise. (1) is termed multiple measurement vector (MMV) model in compressive sensing community. We assume in this work that all frames of $\Delta \mathbf{K}$ share identical or similar sparse support, i.e., inter-frame temporal continuity exists, which is a reasonable assumption in EIT since the variations of pixel amplitudes are slow compared to the frame rate. On the other hand, the non-zero entries in each frame are also assumed to exhibit intra-frame spatial correlation as in [2].

We assume the following priors for the vectorized weight and noise matrices: $\text{vec}(\Delta \mathbf{K}^T) \sim$

$\mathcal{N}(\mathbf{0}, \text{diag}\{\gamma_1 \mathbf{B}_1, \dots, \gamma_g \mathbf{B}_g\} \otimes \mathbf{A})$, $\text{vec}(\Delta \mathbf{V}^T) \sim \mathcal{N}(\mathbf{0}, \gamma_0 \mathbf{I} \otimes \mathbf{A})$, where \mathbf{A} and \mathbf{B} are respectively latent parameters controlling the inter-/intra-frame correlations. Then the conductivity map can be estimated from the maximum *a posteriori* mean of the posterior $p(\Delta \mathbf{K} | \Delta \mathbf{Y}) = \mathcal{N}(\boldsymbol{\mu}, \boldsymbol{\Sigma})$. Alternating-learning approach [3] is adopted during the learning process to estimate one of \mathbf{A} and \mathbf{B} in a whitened model towards another. We use expectation maximization method to update each latent parameter. The computational complexity is approximately $\mathcal{O}(M^3)$ when L is small compared to M .

In the experiment, a saline solution of blue jet ink with a conductivity of 4.21 S/m is prepared. A piston syringe is used to inject the solution into the sensor. The recovered EIT images of five diffusion stages are shown in Table 1, where a clear advantage of the proposed method in terms of spatial resolution and artifacts reduction can be observed.

3 Conclusions

We reconstruct sequential EIT frames with enhanced spatial resolution by imposing spatiotemporal prior within the SBL framework. Real-data experiments demonstrate the effectiveness of the proposed approach.





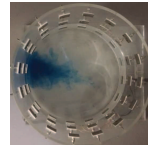
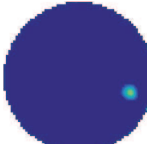

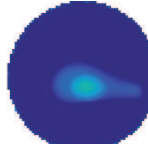
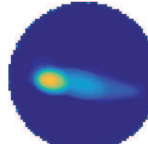


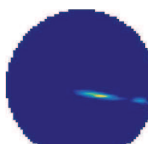
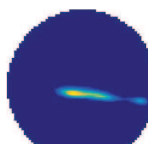
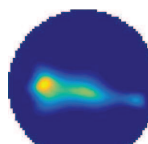
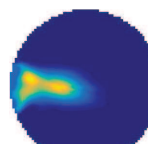
4 Acknowledgements

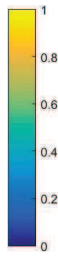
This work was supported in part by the UK EPSRC under Grant No. EP/P006833/1.

References

- [1] S Liu, J Jia, Y. Yang *Proc. 14th IEEE Int. Conf. Imaging Syst. Techni. (IST)*, Beijing, China, Oct 2017
- [2] S Liu, J Jia, et al *IEEE Trans. Med. Imaging*, Under Review
- [3] Z Zhang, T Jung, et al *IEEE Trans. Neural Syst. Rehabil. Eng.*, 22(6): 1186–1197, 2014.

Table 1: Successive reconstructed EIT frames and truth from video snapshots.

Truth					
ℓ_1 regularization					
Proposed approach					



Deep Neural Networks for Noise-Robust Cardiac Output Monitoring

Ethan K. Murphy¹, Justice Amoh¹, Saaid H. Arshad¹, Ryan J. Halter^{1,2}, and Kofi Odame¹

¹Thayer School of Engineering, Dartmouth College, Hanover, NH, ethan.k.murphy@dartmouth.edu

²Geisel School of Medicine, Dartmouth College, Hanover, NH, USA

Abstract: A neural network (NN) approach is presented for estimating cardiac output from noisy bioimpedance data. Our innovation is to train the NN with a subject-specific database of synthetic training examples. The NNs are shown to be robust to poorly-contacting electrodes on a measured tank and simulated thorax experiment.

1 Introduction

Adverse cardiac events account for more than 1 million hospitalizations per year in the United States [1]. Thus the ability to pro-actively monitor cardiovascular health is crucial. EIT is a promising technology to non-invasively and continuously monitor cardiac output (CO), an important cardiac diagnostic metric. Although EIT appears more promising than commercial electrical bioimpedance systems, there remain significant concerns of errors due to several sources, including, electrode contact issues. This study presents results from an algorithm based on deep neural networks (DNN) that is robust to faulty electrodes.

2 Methods

The steps of the proposed CO monitoring system (Fig. 1) are 1) Collect good data from a series of patients in a controlled clinical setting and perform EIT reconstructions and metric extraction, 2) Correlate metrics with stroke volumes, 3) Synthesize a database of training samples that realistically models various measurement errors, such as electrodes with partial contact, and 4) Train a DNN on the synthetic data so that it can accurately estimate stroke volume or CO when presented with actual, noisy measurements.

A measured tank experiment (Fig. 2A) was performed where two different DNNs were trained on synthetic data, and then used to estimate the area of an inclusion from surface impedance measurements. Three of the electrodes used for measurements were partially occluded, as might be encountered in a realistic, non-ideal setting. In a second experiment, the DNN were used to estimate stroke volume from bioimpedance measurements of a simulated chest phantom, which again included partially-occluded electrodes. Simulations and reconstructions used Dartmouth's custom software [2].

One can clearly see that DNN1 works well in both experiments regardless of knowledge of which electrodes are bad (Figs. 2B-C), and that by simply removing bad

electrodes EIT reconstructions themselves can work rather well (Fig. 2B).

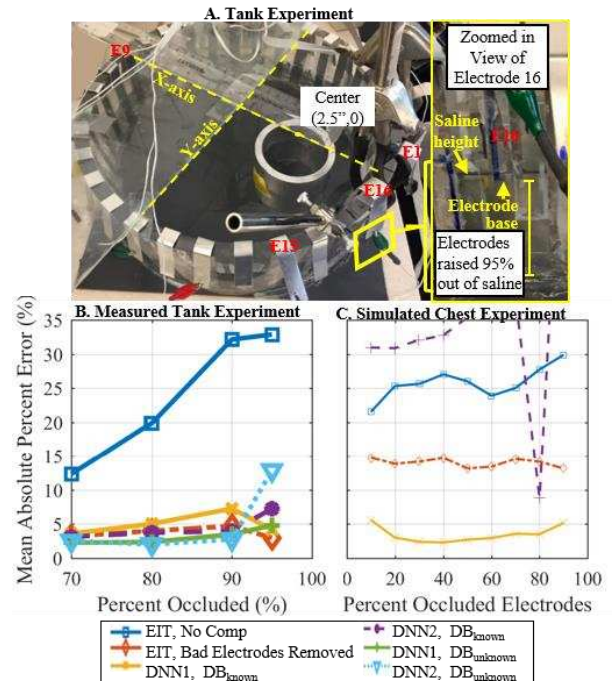


Figure 2: A. The cylindrical tank setup, and the mean absolute percent error for tank and simulated chest experiments. The DNNs were trained on databases that either assumed or did not assume knowledge of which electrodes were ‘bad’. DNN1 is a denoising autoencoder followed by a Gaussian process regression model, while DNN2 is a multilayer feedforward neural network.

3 Conclusions

Although, there are challenges to implement the full proposed CO monitoring approach, the results appear promising and highlight the robustness of DNNs.

4 Acknowledgements

This work was supported in part by the US NSF, Grant No. 1418497, the US NIH, Grant 5R01CA143020, and US DoD CDMRP, Grant W81XWH-15-1-0571.

References

- [1] R. Purcell, et al., BMC Fam. Pract., vol. 15, 43, 2014
- [2] A. Borsic, et al. Proc. Annu. Int. Conf. IEEE Eng. Med. Biol. Soc., Dec. 2008, pp. 1175–1177.

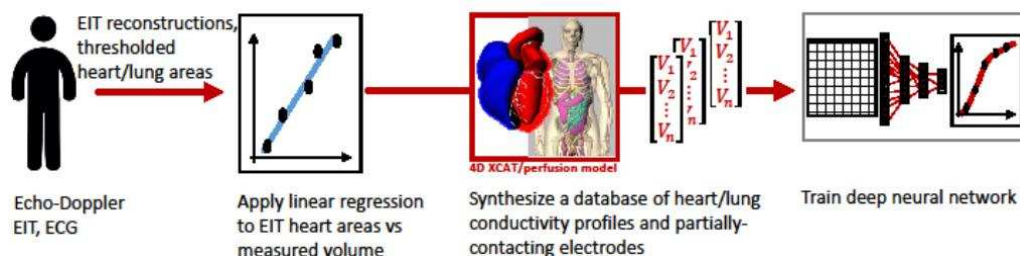


Figure 1. Flow chart of training scheme for the proposed cardiac output algorithm.

EIT for recognition of muscle activity for a physiological rehabilitation therapy

Christian Gibas, Steffen Büchner, Rainer Brück

Medical Informatics and Microsystems Engineering, University of Siegen, Siegen, D, christian.gibas@uni-siegen.de

Abstract: Physiotherapy according to Vojta is used for disorders of the central nervous and the postural and musculoskeletal system. The therapists exert a variable pressure at certain points of the human body, triggering motoric reflexes which have previously been unavailable to the patients (reflex locomotion). We propose to use electrical impedance tomography as a tool to monitor the muscle activity of patients via data patterns. Thereby, the therapist receives feedback as to whether he or she is exercising the therapy correctly.

1 Introduction

Patients and their relatives are often unsure whether previously taught therapy instructions are carried out correctly and comprehensively when at home and without the aid of an expert. This becomes particularly difficult when physiotherapy is performed on another person. In the case of Vojta therapy these persons are babies, often not older than 3 weeks [1]. In this paper we introduce a new technical system for the treatment support of infants and toddlers suffering from a central nervous system disorder. With the aid of our systems, parents can monitor the muscle activation of their child while under therapy and thus, gain insights about the quality of their therapy execution.

2 System Design

Our multi-level layered EIT system can be seen in figure 1(a). The top level consists of a rechargeable battery board, which enables the mobile power supply without cable connection. One layer beneath is a controller board that controls the EIT system and interprets and outputs the measured values. The two lower levels contain the EIT system. On one circuit board (upper) there are mainly the functions of signal generation and selecting the correct feed channel for the current [2]. The lower circuit board contains the evaluation units for the measurement signals. These include selecting the voltage channels, differential amplifiers and an

analog-to-digital converter (ADC). All layers are stacked over pin headers, which convert the electrical connection and the mechanical hold in parallel. The entire system has a size of 10 x 9 x 6 cm and can be used mobile due to its dimensions. Furthermore, the battery shield and the WLAN module underlines this aspect. An electrode belt with 16 electrodes has been developed for use on the body, which adjusts elastically to the lower thorax.

3 Results

We attached the system with the electrode belt to two test persons in the area of the hip in order to check our assumptions. The hip is one of the places where a good physiotherapy execution will most likely cause muscle activity. For our test, we conducted a comparative trial between a relaxed person (see figure 1(b)) and a person with very tense back and abdominal muscles (see figure 1(c)). As can be seen in the corresponding figures, a clear distinction between relaxed and tense muscles can be made. This suggests, that the system used can be helpful for supporting parents and relatives when executing the Vojta therapy at home. A subsequent pattern recognition on the activated muscles may in the future help the practitioners to monitor their therapy execution, document progress and thus gain confidence in their own actions.

4 Acknowledgements

This research has been funded by the Federal Ministry of Education and Research of Germany within the SenseVojta project (project number 13GW0166E).

References

- [1] D. Scrutton *Management of the Motor Disorders of Children with Cerebral Palsy*, doi:10.1136/adc.2004.060897, pp. 75, 1984
- [2] S. Kaufmann *Instrumentierung der Bioimpedanzmessung*, doi:10.1007/978-3-658-09771-4 Springer Vieweg, Wiesbaden, pp. 14-32, 2015

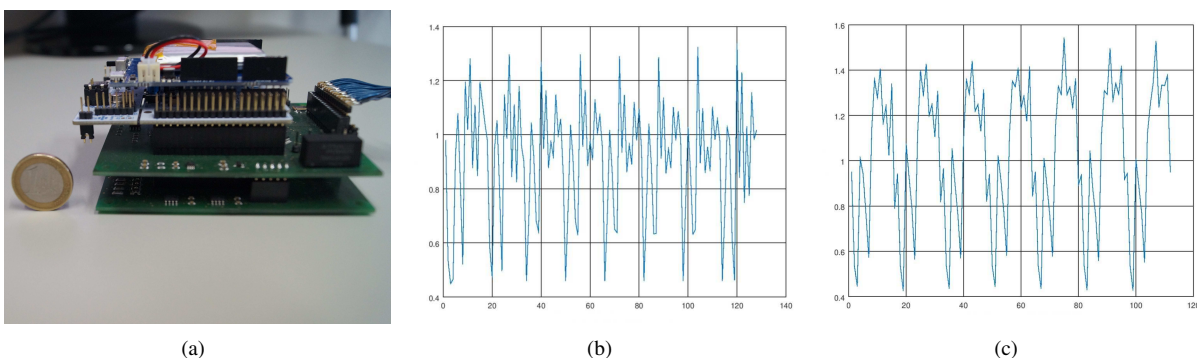


Figure 1: Results of muscle activity measurement with EIT: The developed EIT system can be seen under (a); Under (b) the test person with loose trunk muscles sits on a chair, i. e. is not strained muscularly (X-axis: Amount of measurements, Y-axis: Voltage); Under (c) the test subject is sitting on a chair with strained rum muscles (X-axis: Amount of measurements, Y-axis: Voltage)

Quasi-2D EIT-optical Dual Modality Sensor for Cellular Imaging

Yunjie Yang, Hancong Wu and Jiabin Jia

Agile Tomography Group, School of Engineering, University of Edinburgh, Edinburgh, UK, y.yang@ed.ac.uk

Abstract: A quasi-2D EIT-optical dual modality sensor for cellular imaging was investigated. The design of the micro EIT sensor was demonstrated. High-resolution conductivity contrast arising from MCF-7 cell aggregates was obtained in multiple experiments by using adaptive group sparsity constraint.

1 Introduction

Non-destructive cellular aggregate imaging technique with preferable spatial-temporal resolution is enormous demanded for long-term study of biological behaviour or capture transient cellular dynamics, such as cell culture process and cell-drug interaction [1, 2]. Being able to observe such processes as they happen within the cell aggregate adds a vital extra dimension to understanding of physiological behaviours. Yet, few such techniques have been comprehensively investigated and maturely applied.

This work aims to bridge the gap by demonstrating proof-of-principle that bioimpedance imaging based on a quasi-2D micro EIT sensor is well suited for real-time, high-resolution cell aggregates imaging. This represents a non-destructive cell viability assay based on membrane integrity. The proposed method also sets the stage for implementing multi-modality cellular imaging by combining EIT and optical sensing techniques.

2 Quasi-2D EIT Sensor

A quasi-2D EIT sensor with the ability of simultaneously incorporating optical sensing modalities was designed for real-time imaging of 2D cellular activities. Fig. 1 presents the sensor's schematic and the manufactured sensor. The sensor was directly fabricated on a printed circuit board. The diameter and height of sensing chamber is 14 mm and 1.6 mm. Around the circumference of the sensing region, 16 gilded micro electrodes were fabricated by using half hole process. The bottom of the sensor was sealed with a transparent glass substrate to facilitate microscopic observation while impedance measurement is performed.

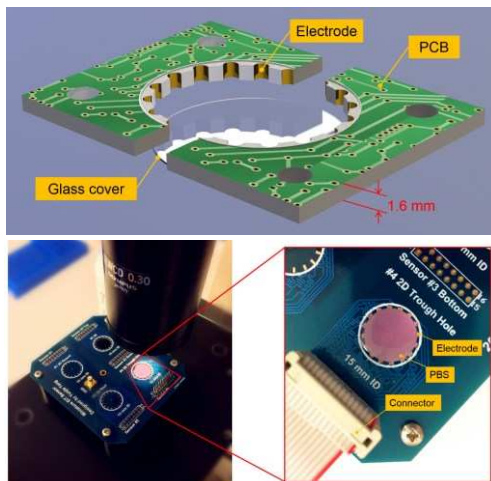


Figure 1: The quasi-2D micro EIT sensor. The first row gives the schematic; the second row shows the manufactured sensor.

Image reconstruction for the proposed sensor was based on an adaptive group sparsity constrained algorithm named AGS, which was developed by the authors and details can be found in [3]. This method combines sparsity and underlying structural information of conductivity to reduce the degree of freedom, which is formulated as:

$$\begin{cases} \min_{\Delta\sigma} & \|\Delta\sigma\|_{w,2,1} = \sum_{i=1}^N w_i \|\Delta\sigma_{s_i}\|_2 \\ \text{s.t.} & \mathbf{J}\Delta\sigma = \Delta V \end{cases} \quad (1)$$

where $\|\Delta\sigma\|_{w,2,1}$ is the weighted $l_{2,1}$ norm. w_i is the weight, and its value can be calculated according to the method given in [3].

3 Cell Aggregates Imaging Results

Two 3D cultured MCF-7 human breast cancer cell aggregates were imaged in the experiments. The diameter of each cell spheroid is approximately 2 mm leading to a diameter ratio of 14.29% with respect to the sensor. Four phantom imaging tests were performed as shown in Fig. 2. In the experiments, the injected current's frequency was 10 kHz and its amplitude was approximately 1.5 mA peak to peak. Image reconstruction was performed based on the conventional 2D model by using the AGS method with a maximum iteration number 500. The experiment results assured that high-resolution conductivity contrast arising from the cell aggregates can be obtained.

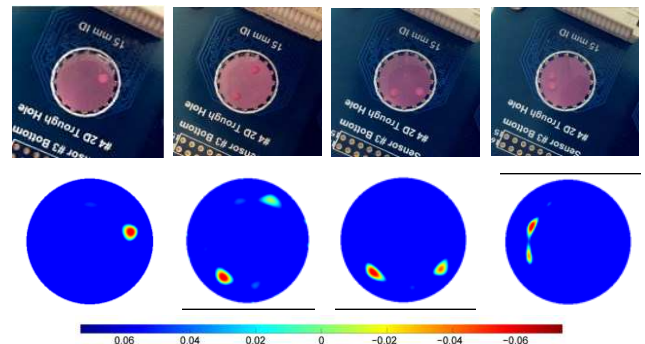


Figure 2: Experiment results. The first row shows four phantoms; the second row gives the image reconstruction results.

4 Conclusions

Based on the experiment results, conclusion can be drawn that by using the designed quasi-2D EIT sensor and AGS algorithm, high quality tomographic images of MCF-7 cell aggregates can be generated based on the real-time measurements. The promising results lay a solid foundation for performing EIT-optical dual modality cellular sensing in the near future.

References

- [1] D J Stephens, V J Allan *Science* 300.5616: 82-86, 2003
- [2] Y Yang, J Jia, S Smith, et al *IEEE Sens. J.*, 17.2: 514–523,2017
- [3] Y Yang, J Jia, *IEEE Trans. Instrum. Meas.*, 66.9: 2295–2305,2017

EIT for assessing muscle contractures: A convenient tool for a common condition?

Hyeuknam Kwon, Benjamin Sanchez, and Seward Rutkove

Beth Israel Deaconess Medical Center, Boston, MA, USA srutkove@bidmc.harvard.edu

Abstract: Fixed muscle contractures occur in primary neuromuscular conditions; the muscle is unable to extend to its full length due to fibrosis. EIT could serve as a valuable tool to assess for abnormal fibrosis. Here we performed finite element model analyses to evaluate the potential of EIT to fibrotic bands in muscle.

1 Introduction

Over the past 15 years, a number of studies have shown the potential value of electrical impedance methods in the evaluation of neuromuscular disease. Most of this work has used 4-electrode impedance technique, rather than EIT; since muscle is fairly homogeneous, such an approach is not unreasonable. However, in conditions in which there is substantial intramuscular heterogeneity, EIT has the potential to serve a valuable role.

One relatively common condition that can affect skeletal muscle is that of a contracture. A contracture causes inability to fully extend a joint/muscle. It can be caused from long-term immobility, a primary muscle injury, such as a tear, or a chronic muscle disease with associated tissue destruction and fibrotic scarring.

There is an increasing interest in primary contracture prevention and potential therapy. Yet, current technologies for assessing contractures are fairly limited, and include only MRI and ultrasound imaging. A convenient bedside/clinic based tool, could find wide application in primary medical and rehabilitative care.

2 Methods

We used conventional time difference frequency difference EIT applied to the surface of the limb at rest and during sustained contraction. Electrostatic simulations were performed using using Comsol Multiphysics (Comsol, Inc., Burlington, MA, USA) and MATLAB (The Mathworks, Natick, MA, USA) using the impedivity properties of tissues obtained from an online database [1]. We increased the impedivity of healthy and diseased muscle during contraction 20% and 10%, respectively. We included several inclusions representing fibrous tissue. The models for relaxed and contracted muscle are shown in fig. 1. The model did not incorporate any change in shape due to the contraction, and thus simulated a isometric contraction.

3 Simulation results

In this simple model we show bands of fibrous tissue in both healthy and diseased muscle while it is at rest. In the healthy muscle, these represent fascial planes, whereas in the disease muscle, these may be due to, in part, to primary muscle fibrosis. With contraction, in the healthy muscles, the tissue lengthens normally and the fibrous bands become invisible on the EIT reconstruction. In the

diseased muscle, when the muscle is extended, the fibrous bands continue to remain relatively unchanged in diameter as compare to baseline, and thus causing heterogeneities in the image, suggestive of persistent fibrotic alterations.

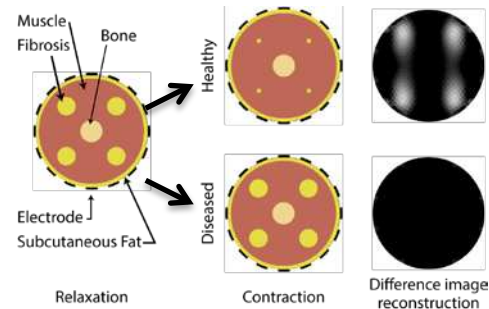


Figure 1: Modelling geometries and reconstruction results.

4 Conclusions

This FEM study suggests a new application for EIT: namely using EIT to assess contraction limitation induced by the presence of abnormal connective tissue. Future work will focus on obtaining actual human data in patients with primary neuromuscular disease with or without associated contractures and making assessments during both isometric contractions (not shape change) and isotonic contractions (with elongation of the muscle).

5 Acknowledgements

This work was supported by NIH Grant K24 NS060951

References

- [1] D Andreuccetti, R Fossi, C Petrucci IFAC-CNR Florence (Italy), 1997. Available: <http://niremf.ifac.cnr.it/tissprop/>

Wearable chest electrical impedance tomography system – a validation study in healthy volunteers

Inéz Frerichs¹, Barbara Vogt¹, Josias Wacker², Rita Paradiso³, Fabian Braun², Michael Rapin², Olivier Chételat² and Norbert Weiler¹

¹Department of Anaesthesiology and Intensive Care Medicine, University Medical Centre Schleswig-Holstein, Campus Kiel, Kiel, Germany, frerichs@anaesthesie.uni-kiel.de

²Swiss Centre for Electronics and Microtechnology, CSEM, Neuchâtel, Switzerland

³Smartex, Pisa, Italy

Abstract: The performance of a novel multi-sensor electrical impedance tomography (EIT) system integrated in a wearable vest was examined in 50 healthy adults. Ventilation-related impedance changes measured with EIT were adequately assessed in most of the studied scenarios with the worst performance determined during walking.

1 Introduction

The clinical use of EIT currently focuses on critically ill mechanically ventilated patients treated in intensive care units. EIT is applied to continuously monitor regional lung ventilation and for adjusting the ventilator settings in these patients [1]. Recent clinical studies carried out in spontaneously breathing patients suffering from chronic lung diseases [2-4] highlight the potential use of EIT in mobile patients for assessing the deterioration of their lung function and the effects of therapy. Patients with chronic obstructive pulmonary disease, asthma or cystic fibrosis might specifically benefit from wearable and remote EIT monitoring ideally combined with simultaneous acquisition of additional bio-signals.

2 Methods

A wearable multi-sensor vest was developed within the EU-funded project WELCOME [5]. The sensors integrated in the garment allowed the continuous measurement of electrical bioimpedance (used in EIT and for detection of breathing rate (BR)), ECG (used to measure the heart rate (HR)), peripheral O₂ saturation (SpO₂), chest sound and body activity. Four male and four female vests in the M, L, XL and XXL sizes were provided. The study was carried out on 50 healthy adult volunteers, 23 women (37 ± 9 yr) and 27 men (38 ± 11 yr). It was approved by local and federal authorities, written informed consent was obtained from all subjects.

The aims of the study were to establish the safety of the vest, the presence and plausibility of the signals and assess the comfort of wearing using questions with a Likert scale. The individual examinations were carried out in two phases. The vest was taken off and put on again in between to assess the reproducibility of findings. Phase 1 consisted of four intervals comprising quiet tidal breathing, deep breathing, forced full expiration and repeated quiet breathing in seated position. Phase 2 consisted of nine intervals. The first four were identical with phase 1, followed by periods of walking, sitting, lying, sitting and writing. Selected signals (BR, HR, single-lead ECG, SpO₂ and body activity) were streamed continuously on a mobile phone using Bluetooth and all signals downloaded via WiFi after the end of examination.

3 Results

WELCOME vests were safe, no adverse events occurred. All intended bio-signals were recorded. The quality of EIT recordings in each study phase, based on the presence of ventilation-related impedance changes in four and nine periods respectively, is presented in Figure 1. Excellent and very good quality was achieved in 66% of subjects in phase 1 and 62% in phase 2. Disturbed EIT signal was mostly detected during walking, where ventilation-related variation was reliably identified in only 20% of subjects.

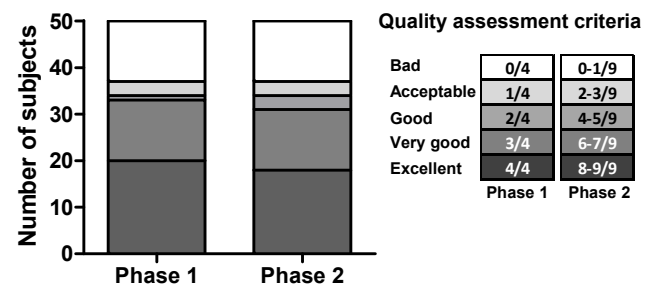


Figure 1: Numbers of subjects with bad, acceptable, good, very good and excellent measurement of ventilation-related impedance changes during the examination phases 1 and 2.

Assessment of body activity was excellent, ECG, HR, BR rendered plausible results. SpO₂ was systematically too low, chest sound quality was inadequate. The comfort of wearing was positively rated with the highest scores achieved for the skin-friendliness of the garment.

4 Conclusions

The safety and performance of the first fully wearable remote EIT system with parallel acquisition of multiple bio-signals was validated in healthy subjects. Our preliminary results imply that monitoring of patients at their homes using EIT might be achievable in the future.

5 Acknowledgements

This study was funded by the European Commission (7th Framework Programme for Research & Technol. Development, project WELCOME, grant agreement No. 611223).

References

- [1] I Frerichs, MB Amato, A van Kaam et al *Thorax*, 72:83–93, 2017
- [2] B Vogt, Z Zhao, P Zabel et al *Am J Physiol Lung Cell Mol Physiol*, 311: L8–L19, 2016
- [3] I Frerichs, Z Zhao, T Becher et al *Physiol Meas*, 37: 698–712, 2016
- [4] Z Zhao, Fischer, I Frerichs et al *J Cyst Fibros*, 11:412-418, 2012
- [5] J Wacker, O Chételat, M Rapin et al *Int. Conf. MOBIHEALTH*, pp. 47–50, Athens, Greece, Nov. 2014

Towards a thoracic conductive phantom for EIT

Serena de Gelidi¹, Andy Bardill¹, Nima Seifnaraghi¹, Yu Wu², Inéz Frerichs³,
Andreas Demosthenous², Andrew Tizzard¹, Richard Bayford¹

¹Middlesex University, London, United Kingdom, s.degelidi@mdx.ac.uk

²University College London, United Kingdom

³University Medical Centre Schleswig-Holstein, Germany

Abstract: Three materials will be characterized in order to generate a conductive and flexible neonatal thoracic phantom. Such model is going to mimic the deformation encountered in a lying position while a boundary reconstruction and EIT imaging are carried out.

1 Introduction

Despite the fact that several phantoms are available to clinicians for training purposes, none of these can mimic the skin conductivity. Therefore, saline-filled tanks, made of insulating materials and featuring metallic nodes, are usually adopted to perform pilot measurements for EIT reconstructions [1, 2]. Recently, a common cylindrical tank has been upgraded into a geometrically accurate skull keeping the insulating material [3]. The use of a conductive material has been introduced for an anatomically accurate pelvic phantom cast for EIT [4] and a 3D printed breast model for Microwave Imaging [5].

Following the development of a prototype for the thoracic boundary reconstruction [6], the need for a conductive, flexible and closable phantom arose. Hence, this work aims to model the lungs area inside an anatomically accurate neonatal thorax, which could be squeezed to mimic the respiration movement while an EIT belt is in place. The goals of the study consist into comparing the material performances and validating the boundary reconstructions.

2 Methods

Three different materials have been selected to develop the thoracic prototypes.

- A carbon impregnated polyurethane foam (Teknis Limited, UK). Five samples, featuring the same cross-section (10mm x 10mm) and different lengths, have been tested by means of a Solartron 1260 impedance analyzer. The resistance and the absolute permittivity have been measured by sweeping the frequency up to 2MHz. Successively, the conductivity and the relative permittivity have been calculated.
- A mix of a silicone (75%), carbon black powder (15%) and graphite powder (10%) [5], which needs to be synthesized. Carbon black powder has been preferred over carbon fibres in order to promote the isotropy of the generated material.
- A carbon filled thermoplastic polyurethane Palmiga 95-250 (Creative Tools, Sweden) has been acquired among the newest filaments available for 3D printing.

3 Results

The relative permittivity of foam samples is shown in Figure 1. The curing of the second material has been inhibited either while using a platinum-cure silicone Transil 20 (Mouldlife, UK) or a water white clear urethane Clear Flex

30 (Smooth-On, US). The same result has been observed even changing the methodology and the percentages.

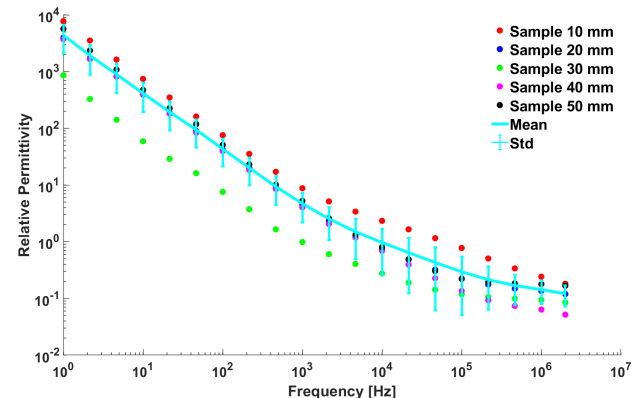


Figure 1: Relative permittivity calculated for each sample of the carbon impregnated polyurethane foam tested by means of an impedance analyzer.

4 Discussion

The curing inhibition, which surprisingly has not been experienced in previous works, could be related to impurities (e.g. sulphur) contained in the graphite. Further syntheses will be attempted. Following the dielectric characterization of samples for each material, two main comparisons will be addressed. Firstly, the materials performance, in terms of conductivity and versatility, will be evaluated for the same thoracic boundary. Such study appears to be novel to the best of the authors knowledge. Secondly, the phantoms will be used to validate the shape detection and reconstruction. Hence, the EIT reconstructed image of each undeformed phantom will be compared to the corresponding arbitrary deformed one.

5 Acknowledgements

This work is supported by the CRADL project which has received funding from the European Union's Horizon 2020 research and innovation programme 2014-2018 under grant agreement No 668259.

References

- [1] Grychtol B, Müller B, Adler A. *Physiol Meas*, 37:785–800, 2016
- [2] Busch C, Schullcke B, Moeller K. *Curr Dir Biomed Eng*, 3:291–294, 2017
- [3] Avery J, Aristovich K, Low B, Holder D. *Physiol Meas*, 38:1116–1131, 2017
- [4] Dunne E, McGinley B, O'Halloran M, Porter E. *Physiol Meas*, 10.1088/1361-6579/aaa3c0, 2017
- [5] Faenger B, Ley S, Helbig M, Sachs J, Hilger I. *11th EUCAP*, vol. 1, 1065–1068. 2017
- [6] de Gelidi S, Bardill A, Wu Y, Demosthenous A, Tizzard A, Bayford R. A Boyle, R Halter, E Murphy, A Adler, eds., *Proc. 18th Int. Conf. Biomed. Appl. Electr. Impedance Tomogr.*, 25, Hanover (US)2017

A Field Theory Approach in EIT with Green's Functions

Christos Dimas¹, Nikolaos Uzunoglou and Paul P. Sotiriadis

Dept. of Electrical and Computer Engineering, National Technical University of Athens, Greece

¹chdim@central.ntua.gr

Abstract: A field theory employing Green's functions is used to develop an imaging algorithm of weak conductivity variations in EIT. The algorithm results in a linear system of equations whose solution gives both the potential and the conductivity distributions.

1 Introduction

EIT imaging of soft deep-body tissues, away from the skin, challenges the numerous existing image reconstruction algorithms. Part of the difficulty is to image significantly small inhomogeneous internal conductivity variations without resorting to memory-expensive inverse problem solution ways [1].

2 Methods

2.1 The Forward Problem

Consider a 2D medium with conductivity $\sigma = \sigma(\mathbf{r})$ and two point electrodes sourcing and sinking current I and be placed at \mathbf{r}_+ and \mathbf{r}_- respectively. The EIT's equation is

$$\nabla\sigma\nabla V + \sigma\nabla^2 V = I[\delta(\mathbf{r} - \mathbf{r}_+) - \delta(\mathbf{r} - \mathbf{r}_-)] \quad (1)$$

where $V = V(\mathbf{r})$ is the potential and \mathbf{r} is the observing position. Assuming no other current sources are present and integrating over the domain of interest A' , with the use of Green's theorem [2], we get the integral equation

$$V(\mathbf{r}) = \iint_{A'} G(\mathbf{r}, \mathbf{r}') \frac{\nabla\sigma(\mathbf{r}')}{\sigma(\mathbf{r}')} \nabla V(\mathbf{r}') dA' + \frac{I[G(\mathbf{r}, \mathbf{r}_+) - G(\mathbf{r}, \mathbf{r}_-)]}{\sigma_0} \quad (2)$$

Where \mathbf{r}' is the position vector within A' where integration takes place. Let σ_0 be the homogeneous conductivity reference and G be a Green's function solution of the homogeneous Laplace's equation $\nabla^2 G(\mathbf{r}, \mathbf{r}') = \delta(\mathbf{r} - \mathbf{r}')$. Assuming a circular area of radius R_0 and keeping the 1st Fourier series term, the Green's function gives

$$G(\mathbf{r}, \mathbf{r}') = \frac{1}{2\pi\sigma_0} \left[\ln \frac{1}{|\mathbf{r} - \mathbf{r}'|} - \frac{r r'}{R_0^2} \cos(\varphi - \varphi') \right] \quad (3)$$

Where $r = \|\mathbf{r}\|$, $r' = \|\mathbf{r}'\|$ and φ, φ' are the angles of \mathbf{r}, \mathbf{r}' respectively. For small conductivity variation e.g. when $|\sigma - \sigma_0| < \sigma_0/10$ it is $\nabla V \approx \nabla V_0$ and the homogeneous potential V_0 equals the Green function's solution.

2.2 The Inverse Problem

To solve the inverse problem near the centre, the internally inscribed orthogonal parallelogram of the circle is discretized to square pixels, with $\Delta\alpha$ side length. Each pixel corresponds to a conductivity contribution $\sigma_{i_2 j_2}$ such that

$$\ln \sigma_{i_2 j_2} = \sum_{i_1=1}^M \sum_{j_1=1}^M a_{i_1 j_1} e^{-\frac{(x_{i_1} - x_{i_2})^2 + (y_{j_1} - y_{j_2})^2}{D^2}} \quad (4)$$

Where $\mathbf{r}' = (x_{i_2}, y_{j_2})$ are the central point coordinates of an arbitrary pixel and $\mathbf{r}_{central} = (x_{i_1}, y_{j_1})$ are the central coordinates of the referring pixel. Parameter D must be small enough to avoid aliasing. Taking the gradient of Eq. (4) and using it in Eq. (2) we replace the non-linear term $\nabla\sigma/\sigma$. Using the midpoint integral rule, the inhomogeneous part of equation 2 is written as

$$V(\mathbf{r})_{change} = \sum_{j_2=1}^M \sum_{i_2=1}^M \Delta\alpha^2 G(\mathbf{r}, \mathbf{r}') \frac{\nabla\sigma}{\sigma} \Big|_{i_2, j_2} \nabla V_0(\mathbf{r}') \quad (5)$$

In Eq. (5), vector \mathbf{r} is the position of the voltage observation points. Taking into consideration the homogeneous and inhomogeneous model measurements, the problem concludes to a linear system of equations $M\mathbf{x} = \mathbf{b}$, where \mathbf{b} is the measurement vector, \mathbf{x} is the unknown vector of the coefficients $a_{i_1 j_1}$ and the entries of M are

$$m_{kli_1 j_1} = \sum_{i_2=1}^N \sum_{j_2=1}^M \Delta\alpha^2 [G(\mathbf{r}_l, \mathbf{r}') - G(\mathbf{r}_{l+1}, \mathbf{r}')] \nabla \ln(\mathbf{r}') \Big|_{i_2, j_2} \nabla V_0(\mathbf{r}_{k, k+1}, \mathbf{r}') \quad (6)$$

Where $k, k+1$ refer to the current electrode pairs and $l, l+1$ refer to the voltage pairs. In order to have a well-defined problem, the total number of pixels is chosen in such a way to equal the number of the total measurements. Since M is close to singular, the system is solved using the biconjugate gradient's method with preconditioner [3].

3 Results

For the testing, inhomogeneous models were created using the FEMM along with the MATLAB tool. The electrode measurements were computed using Eq. (2) assuming opposite strategy with 32 electrodes and a reconstruction performed using the back-projection algorithm. Then, conductivities were calculated using the method described.

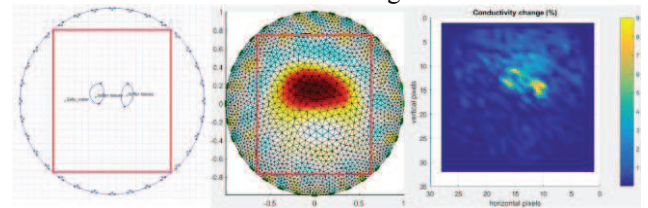


Figure 1: Image reconstruction of two small conductivities near the centre: EIDORS (centre), described approach (right).

4 Conclusion

This approach of EIT conductivity imaging provides a relatively simple and alternative way to image deep-body soft tissue conductivity variations. Applications could be developed in chest imaging and breast cancerous inhomogeneities detection.

References

- [1] A. Adler, Boyle: *IEEE Trans. on Biom. Eng.*, Vol 11, Issue 64, 2017
- [2] S. Hasebe, Y. Kano: *IEEE Trans. on Magn.*, Vol. 24, Issue: 6, 1988
- [3] Y. Mojddeh, S. Nejad Ash, Liu *Understanding the BiCGSTAB*, 2016

Deep learning method for lung EIT

Ariungerel Jargal¹ and Yizhuang Song²

¹Computational Science and Engineering department, Yonsei University, Seoul, South Korea, j.ariungerel@gmail.com

²School of mathematics and statistics, Institute of Data Science and Technology, Shandong Normal University, China, ysong@sdsnu.edu.cn

Abstract: In lung EIT, using the method in [1], two lungs tend to merge together for obese people. To handle this problem, a strong regularization term containing the geometrical information of two lungs should be added. We performed a pilot study on providing the constraint using deep learning method. Numerical simulations validate the theory.

1 Introduction

EIT has potential applications in continuously monitoring the function of lung of human body due to its ability to reconstruct a high temporal resolution conductivity image. EIT way of lung imaging is based on minimizing the mismatch between the boundary measured voltage data and the data from solving the forward model with the same boundary conditions. Due to the ill-posedness nature of EIT, existing methods of the minimizing procedure is usually accompanied with a regularization term. However, we found that in many cases the traditional regularization such as Tikhonov regularization does not work for the lung imaging; e.g. for obese people, two lungs are merged in the reconstructed image [1]. In this paper, we propose a deep learning method to provide a priori geometrical information including sizes, shapes and locations of two lungs. Numerical results validate the proposed method.

2 Methods

2.1 Conventional lung EIT method

Let Ω be the chosen imaging slice of the imaging object, the lung. The conductivity distribution of the lung is dependent on the time variable t . We denote $\sigma^t(\mathbf{r})$ as the conductivity distribution of Ω at $\mathbf{r} = (x, y) \in \Omega$ and the time t . Note that for EIT-based lung imaging, we are aiming at the reconstruction of the conductivity changes with respect to t , $\frac{\partial \sigma^t}{\partial t}$.

In an E-channel EIT system, to probe $\frac{\partial \sigma^t}{\partial t}$, we inject several sinusoidal currents $i(t) = I \cos \omega t$ ($\omega/2\pi \leq 1$ MHz) through selected electrode pairs $(\mathcal{E}_{p(j)}, \mathcal{E}_{q(j)})$ attached on $\partial\Omega$, the boundary of Ω . We can measure the voltage difference $V_{jk}^t = u_j^t|_{\mathcal{E}_{p(k)}} - u_j^t|_{\mathcal{E}_{q(k)}}$, where $p(j)$ and $q(j)$ are two different numbers chosen in $\{1, 2, \dots, E\}$, u_j^t is the induced voltage potential corresponding to the j -th injection current. Denoting $\mathbf{V}^t = (V_{12}^t, V_{23}^t, \dots, V_{EE}^t)$, the conventional methods for the reconstruction of $\frac{\partial \sigma^t}{\partial t}$ from $\frac{\partial \mathbf{V}^t}{\partial t}$ is based on minimizing $\Phi[\frac{\partial \sigma^t}{\partial t}] = \frac{1}{2} \|\mathbf{S}_{\sigma^0} \frac{\partial \sigma^t}{\partial t} - \frac{\partial \mathbf{V}^t}{\partial t}\|^2 + \lambda \text{Reg}(\frac{\partial \sigma^t}{\partial t})$, where the first term is the fidelity term while the second term is regularization term with a regularization parameter $\lambda > 0$, \mathbf{S}_{σ^0} is the sensitivity matrix [2, 3]. Unfortunately, the conventional regularization such as [1] does not work for a human body with a thick obese since their lungs are closely located and far from the boundary comparing to the people with normal weights. Hence, we need to add a strong constraint containing the geometrical information of two lungs to handle the ill-posedness for this situation.

2.2 Proposed method based on deep learning

In this section, we proposed a deep learning method for providing the geometrical information of two lungs. We learn a function $f : \frac{\partial \mathbf{V}^t}{\partial t} \mapsto \phi^t$ from many training data $\{(\frac{\partial \mathbf{V}_j^t}{\partial t}, \phi_j^t)\}_{j=1}^N$, where ϕ^t is a vector contains the information of the sizes, locations and shapes of two lungs. In our paper, f is achieved from

$$f = \underset{f \in \mathcal{U}_{MLP}}{\text{argmin}} \frac{1}{N} \sum_{j=1}^N \|f(\frac{\partial \mathbf{V}_j^t}{\partial t}) - \phi_j^t\|^2, \quad (1)$$

where \mathcal{U}_{MLP} is the MLP net. Hence, $\frac{\partial \sigma^t}{\partial t}$ could be reconstructed from the minimizing procedure containing the geometrical information $f(\frac{\partial \mathbf{V}^t}{\partial t})$.

3 Results

We used two ellipses which is close to each other to mimic the lungs of obese people. The number of training data is 5000 with different sizes, locations and shapes of the ellipses. The following figure shows the reconstruction result using the proposed method.

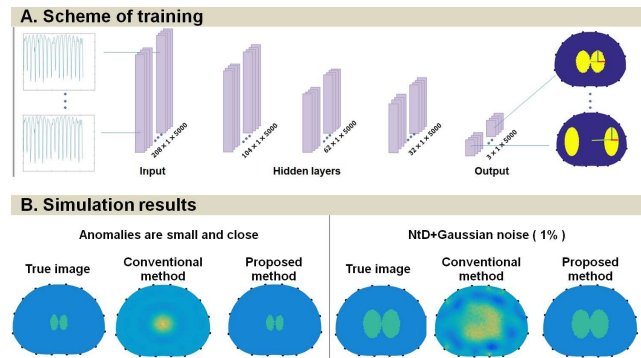


Figure 1: Scheme of the training and the simulation results.

4 Conclusions

This pilot study shows that deep learning method can be used to provide a reliable geometric constrained information in lung EIT for the obese people.

5 Acknowledgements

A.J was supported by the National Research Foundation of Korea (NRF) grant 2017R1E1A1A03070653. Y. Song was supported by National Natural Science Foundation of China (Grant No. 11501336).

References

- [1] K. Lee, E. J. Woo, J. K. Seo "A Fidelity-embedded Regularization Method for Robust Electrical Impedance Tomography" *IEEE trans. on Medical imaging*, 2017.
- [2] L. Zhou, B. Harrach, J. K. Seo "Monotonicity-based Electrical Impedance Tomography for Lung Imaging" *Inverse problems*, 2018.
- [3] DS Holder *Electrical Impedance Tomography* IOP Publishing: Bristol, 2005.

Fat volume quantification by using weighted frequency difference Electrical Impedance Tomography (wfdEIT)

Tingting Zhang¹, Geuk Young Jang¹, Tong In Oh¹, Eung Je Woo¹

¹Impedance Imaging Research Center, Kyung Hee University 23 Kyunghedae-ro, Dongdaemun-go Seoul 02447, Korea
zttysu@khu.ac.kr

Abstract: The human tissues show a frequency dependent behavior due to the existence of insulating membranes. fdEIT takes account of the frequency-dependent characteristics of tissues and is promising for the quantification of the volume of fat which is frequency-independent.

1 Introduction

Subcutaneous fat is stored below the layers of skin which is not necessarily hazardous to your health. Visceral abdominal fat is stored deeper in the abdomen which is wrapped around major organs like the liver, pancreas and your kidney. Too much visceral fat creates can lead to inflammation and high blood pressure. It is important to quantify the amount of visceral fat and muscle inside of abdomen for the long-term health. Bioimpedance spectroscopy (BIS) for body composition analysis [5] has been used to quantify the composition of the human body. The objective of this study is to evaluate the capability of the proposed method in non-invasively quantifying the amount of visceral abdominal fat through the weighed frequency difference electrical impedance tomography [1–3].

2 Methods

Let Ω denote the interested two-dimensional region embedded with multiple cells \mathcal{C}_k , $k = 1, \dots, N_c$ as shown in Figure 1.

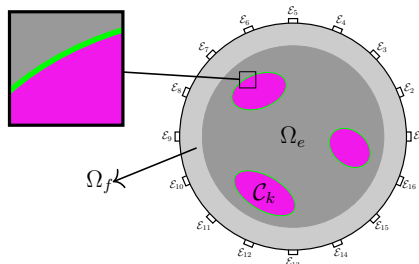


Figure 1: The configuration model of multi-frequency electrical impedance tomography system.

The circular layer Ω_f and Ω_e are assumed to have frequency independent electrical properties. The cell denoted as $\mathcal{C} = \cup_{k=1}^{N_c} \mathcal{C}_k$ is surrounded by uniform-thickness membrane:

$$d \ll d(\mathcal{C}_k) < d(\Omega).$$

When a sinusoidal current with an angular frequency ω ($0 \leq \omega/2\pi \leq 10^6$) is applied through boundary $\partial\Omega$ of Ω , the induced frequency dependent complex potential u^ω satisfies the following system:

$$\begin{cases} \nabla \cdot (\gamma^\omega \nabla u^\omega) = 0, & \text{in } \Omega, \\ \gamma^\omega \frac{\partial u^\omega}{\partial \nu} = g, & \text{on } \partial\Omega, \end{cases} \quad (1)$$

where $\gamma^\omega = \sigma + i\omega\epsilon$ is the admittivity distribution with conductivity σ and permittivity ϵ , ν is the outward unit normal vector and g is the magnitude of the current density on

$\partial\Omega$ due to the injection current [4]. The admittivity distribution inside Ω is assumed to be piecewise constant in each subdomain which can be written as

$$\gamma^\omega = \begin{cases} \gamma_f^\omega = \sigma_f + i\omega\epsilon_f, & \text{in } \Omega_f, \\ \gamma_e^\omega = \sigma_e + i\omega\epsilon_e, & \text{in } \Omega_e, \\ \gamma_c^\omega = \sigma_c + i\omega\epsilon_c, & \text{in } \mathcal{C}, \\ \gamma_m^\omega = \sigma_m + i\omega\epsilon_m, & \text{in Membrane,} \end{cases} \quad (2)$$

Since the thin layers are assumed to be insulating, then

$$\sigma_i \approx 0 \ll \sigma_b < \sigma_c. \quad (3)$$

The collected voltages \mathbf{V}_ω at ω_k can be written as [3, 4]

$$\mathbf{V}_k = [V_{1,1}^k, V_{1,2}^k, \dots, V_{p,q}^k, \dots, V_{N_e, N_e}^k], \quad (4)$$

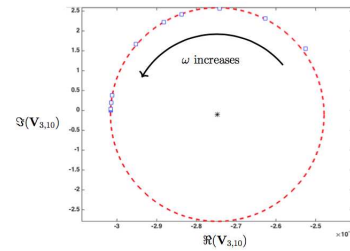


Figure 2: The Colo-plot of $\mathbf{V}_{3,10}$ collected between $\mathcal{E}_{10}, \mathcal{E}_{11}$ when current is injected through $\mathcal{E}_3, \mathcal{E}_4$.

3 Numerical simulations

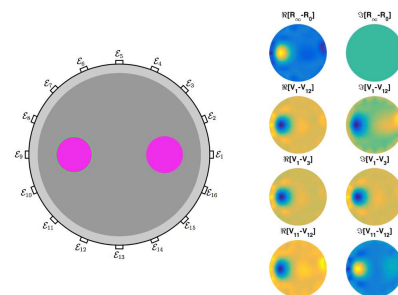


Figure 3: Numerical simulation models and result

References

- [1] TI Oh, H Koo, KH lee, SM Kim, J Lee, SW Kim, JK Seo, EJ Woo *Physiol Meas*, 29:295–307: 2008
- [2] JK Seo, J Lee, SW Kim, H Zribi, EJ Woo *Physiol Meas*, 29(8): 2008
- [3] DS Holder *Electrical Impedance Tomography* IOP Publishing: Bristol, 2005
- [4] JK Seo, EJ Woo *Nonlinear Inverse Problems in Imaging* Wiley Press, 2012
- [5] C Earthman, D Traugher, J Dobratz J, W Howell. *Nutr Clin Pract*. 22(4):389- 405:2007.

Effect of Thorax Deformation during Neonatal Lung EIT

Nima Seifnaraghi¹, Andrew Tizzard¹, Serena de Gelidi¹, Davood Khodadad², Sven Nordebo², Anton van Kaam³, Inéz Frerichs⁴, Andreas Waldmann⁵, Erich Sorantin⁶, Sebastian Tschauner⁶, Andreas Demosthenous⁷, Richard Bayford¹

¹Faculty of Science and Technology, Middlesex University, London, UK n.seifnaraghi@mdx.ac.uk ²Department of Physics and Electrical Engineering, Linnaeus University, Vaxjo, Sweden ³Faculty of Medicine, University of Amsterdam, Amsterdam, The Netherlands ⁴Department of Anaesthesiology and Intensive Care Medicine, University Medical Centre Schleswig-Holstein, Kiel, Germany ⁵Swisstom AG, Landquart, Switzerland ⁶Department of Radiology, Medical University of Graz, Graz, Austria ⁷Department of Electronic & Electrical Engineering, UCL, London, UK

Abstract: The potential effect of deformation of thorax on extracted clinical parameters in neonatal lung EIT is investigated based on developed pre-term models.

1 Introduction

Unfortunately knowledge regarding the precise anatomical and mechanical properties of neonatal chest (more specifically pre-terms) is quite limited. One of the main reasons for this is a rarity of medical images, a consequence of their critical medical conditions at birth, constant movements and hazardous effects of some imaging techniques, such as CT. Previously [1] we had shown using more age-appropriate models could lead to changes in the final clinical parameters such as silent spaces. However, the evaluation of such changes is extremely challenging since there is no reference to be used as standard for comparison.

During the modelling of pre-term neonates a considerable deformation in thorax has been observed. This is because the rib cage bones are not yet calcified and hence are soft and flexible. The deformation can have impacts on the extracted parameters both by affecting the reconstruction procedure because of deviation from the forward model and also on parameters such as silent spaces which are calculated from lung contour. Below an example of foetus with a gestational age (GA) of 29 wk is shown *in-utero*, demonstrating how the thorax and left lung have been affected. In neonatal lung EIT, the patients are positioned supine or prone and therefore the weight distribution is significantly different.

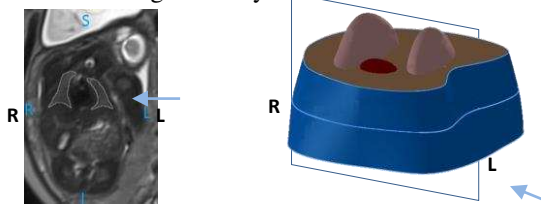


Figure 1: Thorax Deformation (a) Left arm pressing the thorax pushing left lung away (b) corresponding 3D model

2 Method

In addition to the quality of the reconstructed image breath rate is used to investigate the effect of deformation of the thorax during the EIT monitoring. The advantage of exploiting breath rate as a reference scale lies in the fact that it can be computed directly from measured voltages and independently from reconstructed images [2]. The change in shape will be simulated using structural mechanics analysis and compared against the unchanged model implementing the same inverse method and parameters.

3 Results

The 3D models have been developed directly based on MRI image from fetuses in gestational ages Fig. 2.

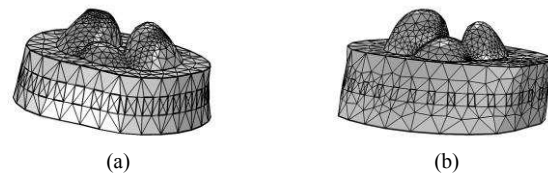


Figure 2: FEM models with projected electrodes; (a) 19 wk, 17.5 cm of circumference (b) 38 wk with 29.17 cm

4 Discussion

This paper presents the first FEM models for three fetuses in the GA range of 19 to 38 wk. Comparisons are made to assess the effect of improving the accuracy of the geometric features as opposed to scaling models from older infants to achieve approximate solutions and its effect on clinical parameters extracted from reconstructions based on these models.

Acknowledgements

This work is supported by the CRADL project which has received funding from the European Union's Horizon 2020, under grant agreement No 668259.

References

- [1] N. Seifnaraghi et al., *Proceeding 18th International Conf. in Biomedical Applications of EIT, Jun, 2017.*
- [2] D. Khodadad et al., *Physiol Meas*, bioRxiv 270348.

Creation and Visualization of High-quality Tetrahedral Meshes from Segmentations using 3D Slicer

Jared Vicory¹, Ethan Murphy² and Ryan J. Halter²

¹Kitware, Inc. Clifton Park NY 12065, USA, jared.vicory@kitware.com

²Thayer School of Engineering, Dartmouth College, Hanover NH 03755

Abstract: There is a need for a free, open-source software for producing segmentations of medical images and, from these segmentations, producing high-quality tetrahedral meshes suited for use in solving the EIT problem with finite element methods. This paper describes the use of 3D Slicer for producing and visualizing these meshes.

1 Introduction

Many medical applications, such as EIT, use finite element methods for various types of analysis. These methods require high-quality tetrahedral meshes of anatomical structures as inputs. Many software options exist for segmenting anatomical structures and for creating tetrahedral meshes of those structures, but many of these options require commercial licenses and lack integration between segmentation and meshing capabilities. In fact, many in the EIT community use different software platforms for segmenting and meshing. This abstract describes the use of 3D Slicer [1,2], a free and open-source program for both performing segmentations and creating and visualizing tetrahedral meshes.

2 Methods

Here, we describe the use of 3D Slicer to perform image segmentation, create high-quality tetrahedral meshes from these segmentations, and visualize tetrahedral meshes that can be used for EIT reconstruction.

2.1 Segmentation

Image segmentation in 3D Slicer is primarily done through the *Segmentations* and *Segment Editor* modules. These easy to use modules include many common segmentation techniques, ranging from manual operations such as drawing and contouring to more automatic techniques such as thresholding, region growing, and graph cut techniques. These modules also include common post-processing operations such as morphological operations, smoothing, island removal, hole filling, and interpolation from sparse contours. Figure 1b shows a chest MRI

segmented into background, chest, and lung segments using region growing from manually-placed seed points.

2.2 Meshing

Following segmentation, the resulting label map can be turned into a high-quality tetrahedral mesh using the *SegmentMesher* extension [3] available via the Slicer Extension Manager. The *SegmentMesher* extension interfaces 3D Slicer with two powerful meshing libraries: Cleaver [4] and TetGen [5]. It will export the segmentation to the chosen mesher and automatically load back in and display the resulting mesh for verification. This mesh can then be saved and used for EIT reconstruction. Figure 1c shows a mesh created via Cleaver loaded into 3D Slicer.

2.3 Visualization

3D Slicer also includes powerful visualization tools for volumetric meshes. Figure 1 shows the ability to both view and clip the model in 3D (1c) as well as show it overlaid on the image it was generated from (1b). There is also support for visualizing scalar fields defined on the mesh if there are specific values at each vertex.

3 Conclusions

3D Slicer is a powerful, free, and open-source program that allows for creating and visualizing high-quality tetrahedral meshes of anatomical structures.

References

- [1] <http://www.slicer.org>
- [2] Fedorov, A. et al. (2012). 3D Slicer as an image computing platform for the Quantitative Imaging Network. *Magnetic resonance imaging*, 30(9), 1323-1341.
- [3] <https://github.com/lassoan/SlicerSegmentMesher>
- [4] Bronson J., Levine, J., Whitaker R., "Lattice Cleaving: Conforming Tetrahedral Meshes of Multimaterial Domains with Bounded Quality". *Proceedings of the 21st International Meshing Roundtable* (San Jose, CA, Oct 7-10, 2012)
- [5] Si, H. (2015). TetGen, a Delaunay-based quality tetrahedral mesh generator. *ACM Transactions on Mathematical Software (TOMS)*, 41(2), 11.

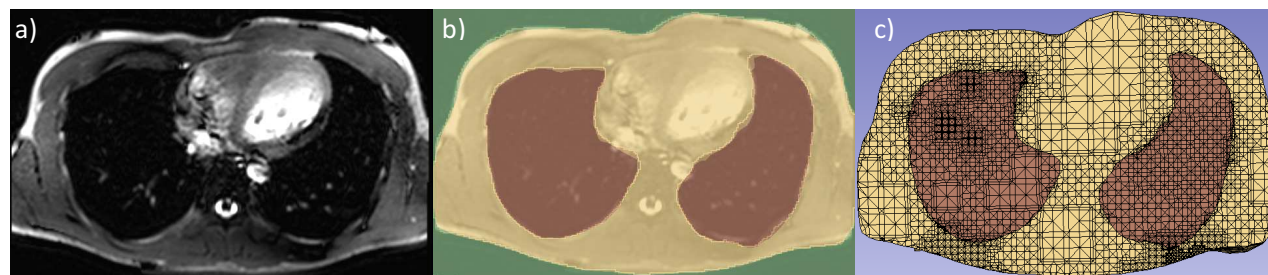


Figure 1: Processing an example chest MRI image in 3D Slicer. a) Input MRI. b) Segmentation into background, chest, and lungs using region growing. c) Tetrahedral mesh of the segmentation computed via Cleaver. The boundaries of the mesh components are overlaid on the segmentation in b.

An efficient classification-reconstruction method for 3D EIT

Bo Gong¹, Sabine Krueger-Ziolek¹ and Knut Moeller¹

¹Institute of Technical Medicine, Germany, bo.gong@hs-furtwangen.de

Abstract: EIT reconstruction in 3D domain suffers from a large number of unknown parameters associated with the FEM method. To circumvent this difficulty we developed a classification-reconstruction method based on an efficient labeling algorithm through a conditional random field model.

1 Introduction

EIT measurement is commonly modeled within the finite element model (FEM) framework. EIT reconstruction is an ill-posed inverse problem. One issue that induces such ill-posedness is the huge number of free parameters associated with the FEM modeling in comparison to the limited number of independent voltage measurements. As a consequence, the optimal solution of the inverse problem is not unique and unstable to noise. To circumvent this problem, different regularization methods have been applied to restrict the freedom the underlying parameters. An attempt to regularize the reconstruction is based on FEM elements clustering, by forcing the FEM elements within each element cluster sharing the same impedance [1, 2]. In previous studies, the clustering methods either require a patient-specific CT image or have a high computational complexity. In this study, we present an efficient approach of such cluster based regularization by applying a conditional random field model. The computation of the proposed method is efficient for 3D reconstruction.

2 Methods

Given the voltage measurement, an efficient linear reconstruction which employs a pre-calculated reconstruction matrix can be performed. The FEM elements are clustered with respect to their initially reconstructed impedance intensities and geometrical proximity. For each FEM elements, a feature vector is generated by combining its geometrical position and its initial conductivity intensity. Associate to each FEM elements, there is a random label variable defined over a fixed label set. Each label indicates a cluster that an element belongs to. By connecting each two of these random label variables, a fully connected random field can be formed. We are interested in the probability distribution of the random label variables in the random field. The collection of the feature vectors is identified as an observation of the fully connected label random field. The observed feature vectors and the hidden random field formed a conditional random field model [3]. The probability distribution of each random label variable conditioned on the feature vectors, i.e., the conditional probability of each label associated with an FEM element, can be determined efficiently[3]. On each FEM element, the label in the label set which has the largest probability was assigned. The FEM elements are grouped into the same cluster if they are assigned with the same label.

Within each cluster, the elements are forced to share the same conductivity. Hence, the degree of freedom of the inverse problem has been reduced. A conjugate gradient solver has been applied on these clusters for fast reconstruction. This framework is summarised as the flowchart in Fig. 1.

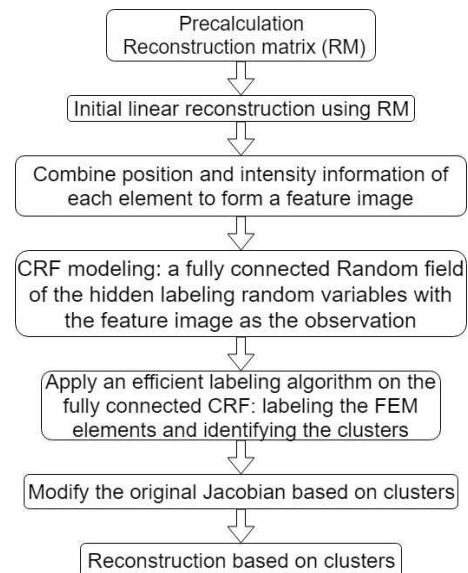


Figure 1: The flowchart of the proposed method.

3 Conclusions

The performance of the proposed framework has been examined on 3D image reconstruction in the simulation. An extruded 3D lung and heart model is employed for simulation (Fig. 2 (A)). The reconstructed images have been demonstrated in Fig. 2, with a top-down view. The 3D FEM mesh has 27,578 nodes. The proposed algorithm is implemented in C++ and Python. The total computation time including the initial reconstruction is around 2s on a laptop with an i5-7200U CPU.

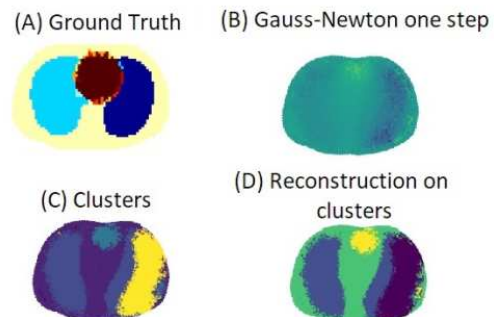


Figure 2: A 3D Simulation of the proposed framework

References

- [1] B. Gong et al., *PhysiolMeas*, 37:843–862,2016
- [2] B. Schullcke et al., *Medical Physics*,44(2): 426-435 2017
- [3] P. Krähenbühl and Valden Koltun *Conf NIPS Proceedings 2011*

Evaluating the Severity of Cystic Fibrosis related Lung Disease by Electrical Impedance Tomography

Sabine Krueger-Ziolek^{1,2}, Bo Gong^{1,2}, Hanna Zimmermann², Ullrich Müller-Lisse² and Knut Moeller¹

¹Institute of Technical Medicine, Furtwangen University, 78054 Villingen-Schwenningen, Germany, krue@hs-furtwangen.de

²Department of Clinical Radiology, LMU Hospital of the University of Munich – Inner City Campus, 80336 München, Germany

Abstract: Electrical Impedance Tomography (EIT) derived parameters indicating regional airway obstruction were correlated with the ‘Total Brody Score (TBS)’ from a computerized tomography (CT) scanning scoring system to investigate the suitability of EIT to evaluate the severity of cystic fibrosis (CF) related lung disease.

1 Introduction

Pulmonary function testing (PFT) and computerized tomography (CT) scanning are common methods in diagnosis and progress monitoring in patients with cystic fibrosis (CF) related lung disease. Compared to PFT which provides numeric data, the analysis in CT scanning is more subjective and depends on the experience of the radiologist. Thus, Brody et al. created a scoring system for the analysis of CT scans which should enable a comparable and quantifiable assessment of pulmonary abnormalities in CF [1]. The scoring system considers anatomical and physiological abnormalities, such as bronchiectasis or mucous plugging, on a lobar basis. The so-called ‘Total Brody Score (TBS)’ includes all lung lobes. However, the analysis of CT scans of the whole lung is very time-consuming, cost intensive and requires a lot of experiences.

In this study, the correlation between Electrical Impedance Tomography (EIT) derived parameters indicating regional airway obstruction and the TBS was investigated to figure out if EIT might be suitable to evaluate the severity of CF related lung disease.

2 Methods

Ethical approval of the study was obtained by the LMU Hospital of the University of Munich.

2.1 Determination of the Total Brody Score

Two radiologists determined the TBS of 10 CF patients (3 female and 7 male, age 35.2 ± 8.4 years, weight 63.9 ± 13.0 kg, height 177.0 ± 10.0 cm, (mean \pm SD)), respectively. The mean value of TBS was calculated for each patient.

2.2 EIT data collection, processing and evaluation

EIT measurements were carried out (Pulmovista 500®, Dräger Medical, Lübeck, Germany) on the mentioned CF patients during normal tidal breathing and a forced vital capacity (FVC) manoeuvre [2] to determine regional impedance changes within the lung related to FVC and the forced expiratory volume in one second (ΔI_{FVC} and ΔI_{FEV1}). EIT data were collected with a frame rate of 30 Hz at the 3rd and 5th intercostal space (ICS), respectively. EIT image reconstruction was performed by using the

Dräger EIT Data Analysis Tool 6.1 (Dräger Medical, Lübeck, Germany). A low-pass Butterworth filter of the 3rd order with a cut-off frequency of 50 min^{-1} was employed to exclude pulsatile components of the EIT signal. Regions of interest (ROI) were determined by utilizing a linear regression fit [3]. Lung areas were defined by pixel values higher than 20% of the maximum regression coefficient within the functional EIT image resulting from the linear regression fit [4].

Regional ratios of ΔI_{FEV1} and ΔI_{FVC} were assessed with the data obtained at the 3rd and the 5th ICS for each patient. Within each thorax section, the median of regional $\Delta I_{FEV1}/\Delta I_{FVC}$ were calculated and correlated with the mean TBS (Figure 1).

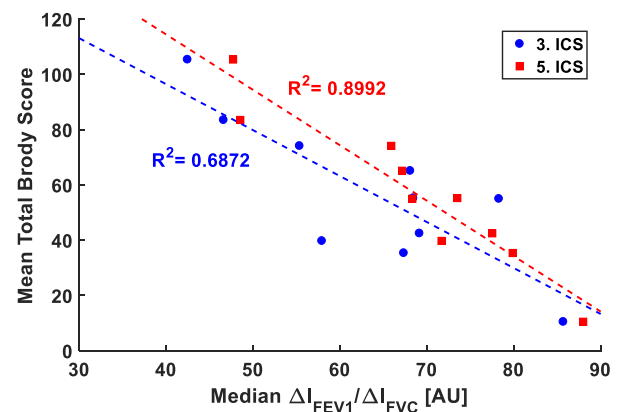


Figure 1: Mean Total Brody Score (TBS) of 10 cystic fibrosis (CF) patients in dependency of the median of regional $\Delta I_{FEV1}/\Delta I_{FVC}$ determined within the 3rd and the 5th intercostal space (ICS), respectively.

3 Conclusions

The mean values of TBS of the 10 CF patients showed a higher correlation with the medians of regional $\Delta I_{FEV1}/\Delta I_{FVC}$ obtained within the 5th ICS compared to the medians of $\Delta I_{FEV1}/\Delta I_{FVC}$ calculated within the 3rd ICS. Since the TBS comprises the whole lung, differences in correlations are most likely based on the lung volume captured at the different thorax sections by EIT. However, results indicate that EIT is suitable to assess the severity of CF-related lung disease.

References

- [1] AS Brody, JS Klein, PL Molina, J Quan, JA Bean, RW Wilmott *J Pediatr.*, 145(1):32-38, 2004
- [2] MR Miller, J Hankinson, V Brusasco, F Burgos, R Casaburi et al. *Eur Respir J*, 26(2):319-338, 2005
- [3] I Frerichs, S Pulletz, G Elke, F Reifferscheid, D Schadler, J Scholz, N Weiler *Respiration*, 77(3):282-291, 2009
- [4] S Pulletz, HR van Genderingen, G Schmitz, G Zick, D Schadler, J Scholz, N Weiler, I Frerichs *Physiol Meas*, 27(5):S115-S127, 2006

3D FEM Simulations of EIT Measurements on the Human Thorax

Anita Just, Michael Quintel and Günter Hahn

University Medical Center (UMG), Göttingen, Germany, anita.just@med.uni-goettingen.de

Abstract: Results of EIT measurements on the human thorax are dependent from the position of electrode plane. In order to quantify and correct for the influencing factors, 3D FEM thorax models from CT data of patients are constructed and used for numerical simulations.

1 Introduction

EIT devices for clinical application in lung monitoring currently use electrodes in a transversal plane at the thorax. However, several investigations [1-3] showed a considerable influence of the cranio-caudal position of the electrode plane on the results of absolute (a-EIT) and functional EIT (f-EIT) as well. One of the reasons is the inhomogeneity of the lung itself. On the other hand, geometrical elements as different thorax and lung shape or different distances of the planes and corresponding lung segments to the boundaries of the body and to other organs will influence the results. Therefore, information from different planes is not fully comparable. In order to investigate the various influencing factors of the plane position on the results of f-EIT and a-EIT, simulations on realistic 3D FEM models of human thorax are performed. On the basis of the known parameter distributions in the models (e.g. homogeneous lung) reconstructed parameters can be evaluated quantitatively and corrected accordingly.

2 Methods

3D Finite Element Models of human thorax are constructed from CT data of patients with healthy lungs by segmentation using Simpleware (Synopsis Inc., Mountain View, US). The meshes are imported into COMSOL Multiphysics (v5.0-5.3a, COMSOL AB, Stockholm,). The general procedure is principally described in [4]. Resistivities of the thorax and of the organs are set according to literature [5]. Resistivity of the lung is set in steps of 1 Ωm from 3 to 20 Ωm simulating a whole breath from deep expiration to deep inspiration. Electrodes are attached to the thorax as points in several planes and simulations were done assuming different drive patterns. From the simulated data sets of voltage differences, images of resistivity changes were reconstructed using

GREIT [6] and images of absolute resistivity by a modified SIRT algorithm [7] with azimuthal averaging.

3 Results and Conclusions

Results show a significant influence of the electrode plane position on both the reconstructions of resistivity changes and absolute resistivities. Fig.1 shows an example with 16 electrodes per plane and adjacent drive pattern in each plane. Generally, reconstructed resistivity appears to be higher in the right lung than in the left and in the upper plane higher than in the middle and bottom ones. Also resistivity changes are affected in a similar way. The reason for this is assumed to be the location of the planes at the lower end of the lung. The model with homogeneous thorax without lungs was used to calculate geometric correction factors in each plane. Tomograms of a-EIT calculated with these factors (right column) show nearly exact lung shapes and smaller differences between planes. Remaining differences are not due to thorax shape but due to position on lower end of the lung! In further investigations, universal approaches for correction of real measurements (a-EIT and f-EIT) in different planes are to be derived from simulations on models from a variety of different patients (different shapes, ages, gender).

4 Acknowledgements

This work is supported by the German Research Foundation (Deutsche Forschungsgemeinschaft DFG, project number HA 6829/2-1).

References

- [1] Just A, Hahn G, Dittmar J, Hellige G. In *10th Int. Conf. on Biomed. Applications of Electrical Impedance Tomography*, 2009
- [2] Hahn G, Just A, Dittmar J, Fromm K H, Quintel M. *Journal of Physics: Conference Series* **434**: 012039, 1-4, 2013
- [3] Karsten J, Stueber T, Voigt N, Teschner E, Heinze H. 2016 *Crit Care* **20**:3, 2016
- [4] Pettersen F J, Høgetveit J O. *J Electr Bioimp*, **2**: 13–32, 2011
- [5] Gabriel C, Peyman A, Grant E H. *Phys. Med. Biol.***54**: 4863–78, 2009
- [6] Adler A et al. *PhysiolMeas*, **30**: S35-55, 2009
- [7] Just A, Ruecker C, Hahn G, Hellige G. In *IFMBE Proceedings* **17**: 404-7, 2007

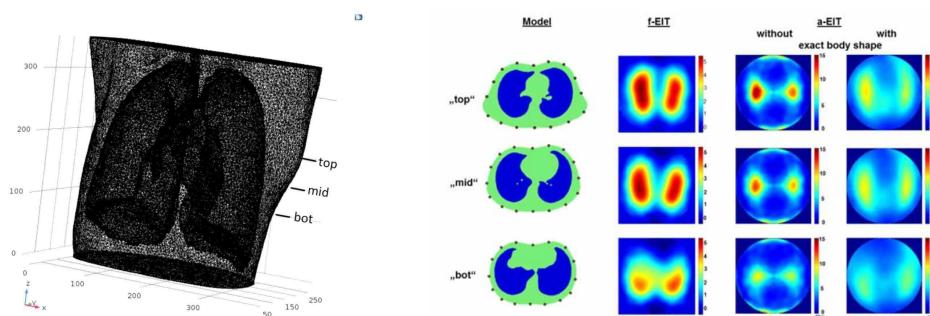


Figure 1: Results of simulated EIT measurements in 3 planes on human thorax with homogeneous lung. Left: 3D FEM thorax model, middle: cross sections in three planes, right: tomograms of resistivity changes (f-EIT, relative changes between full inspiration ($\rho_{\text{lung}}=20 \Omega\text{m}$) and full expiration ($\rho_{\text{lung}}=3 \Omega\text{m}$)) and absolute resistivities (a-EIT, $\rho_{\text{lung}}=10 \Omega\text{m}$) reconstructed assuming an elliptical cylinder and exact body shape.

Demonstration of Multi-frequency MREIT using Semipermeable Membrane Models and Experiments

Munish Chauhan¹, Andrew Xi², Neeta Ashok Kumar¹, Fanrui Fu¹, and Rosalind J Sadleir¹

¹SBHSE, Arizona State University, Tempe, AZ, United States rosalind.sadleir@asu.edu

²ECEE, Arizona State University, Tempe, AZ, United States

Abstract: Magnetic Resonance Electrical Impedance Tomography (MREIT) has been used to measure low frequency (~10 Hz) electrical conductivity properties. Here, finite element simulations are used to show that it should be possible to measure electrical properties at frequencies in the range 10--8000Hz using current waveform modulation. We also show imaging results that demonstrate differential signals can be measured in phantoms containing dialysis membranes with different thicknesses and permittivity characteristics.

1 Introduction

MREIT has typically been used to image low-frequency electrical properties of tissue [1]. Since, electrical properties of biological tissue are complex and frequency dependent, and show large variation in the range between 10 Hz and 1000s of Hz. Therefore, it is of interest to determine if MREIT can image frequency dependence separate from other stray conductive or scanner dependent effects. In this study, we performed simulations to determine the spectra of modulated MREIT waveforms and determined critical frequencies of a semipermeable membrane in a simulated phantom. Finally, we imaged several semipermeable membranes using spin-echo MREIT techniques and modulated MREIT waveforms.

2 Methods

A standard MREIT current waveform (cycle length of 100 ms, and a duty cycle of 64% [2,3]) was constructed using MATLAB, using a 10-kHz sample rate. The modulated waveform was created by multiplying a rectified 500 Hz sine wave, sampled at the same 10 kHz rate, with the standard waveform. The spectrum of the standard waveform was principally at 10 Hz, and rectification of the modulating function resulted in its spectrum having peaks at both 10 Hz around 1000 Hz. A two-dimensional COMSOL (Burlington, MA) model of a conducting square (10 cm) was constructed for FEM simulations. A cellulose membrane-like (thickness 72 nm [4]) inclusion was modeled using the COMSOL AC/DC Module contact impedance boundary condition. The conductivity and relative permittivity of the membrane were set to be 10^{-7} S/m, and 3 respectively. The conductivity of the medium surrounding and within the membrane was 1 S/m, and its relative permittivity was 80. A normal current density of 1 A/m² was applied at the upper edge, and the lower edge was grounded.

An experiment was performed using membrane from Fisher (S25645A, 0.8-inch diameter) which had molecular weight cut-offs of 12k and 3.5k. MR Spin-echo imaging was performed using a 7T Bruker MRI (Billerica, MA) with bore diameter 20cm, located at the BNI, AZ, USA. Imaging parameters were: Field of view = 80x80 mm², matrix size = 100x100, TR/TE = 1000/40 ms, slice thickness = 5 mm, averages = 4, injected current amplitude (I^{\pm}) = 2.5mA, Tc= 36ms, and total scan time = 400s. MR phase measured during separate positive and negative current injection were combined to compute the z -component of the magnetic flux density (B_z) and cancel the effect of systematic phase artifacts. Differences between magnitude images at different frequencies were compared.

3 Results

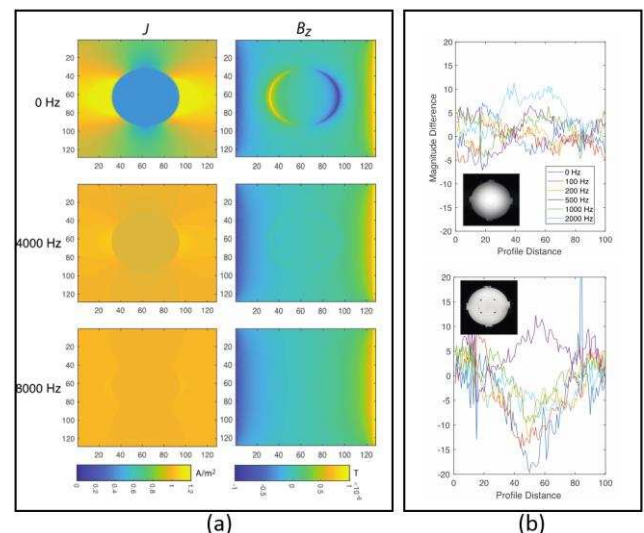


Figure 3. (a) The simulated magnitude of the complex current density as a function of frequency. Since the membrane did not conduct at low frequencies, the current density within the membrane was low below around 100 Hz, but as frequency increased the current distribution became more uniform. (b) Comparison of differences between positive and negative current magnitude images, showing pattern differences in magnitude images between different frequencies and 0 Hz for non-conducting (top) and conducting membranes.

4 Conclusions

We believe these results indicate that it may be possible to use MREIT to image frequency dependent properties of biological tissues.

References

- [1] JK Seo & EJ Woo *PhysiolMeas*, 29; R1–R26,2008
- [2] AK Kasinadhuni et al. *Brain Stimu*, 10:764-772,2017
- [3] AK Kasinadhuni et al. ISMRM, Singapore, 2016
- [4] K Asaka *Journal of Membrane Science* 50, 71-84, 1997

Clinical acceptance of various EIT parameters in neonatology and paediatrics: A systematic assessment of clinicians' opinions

Tobias Becher¹ and Inéz Frerichs¹

¹Department of Anaesthesiology and Intensive Care Medicine, University Medical Centre Schleswig-Holstein, Campus Kiel, Kiel, Germany tobias.becher@uksh.de

Abstract: A questionnaire to validate the clinical usefulness of 14 previously published EIT parameters was completed by 32 clinicians with different degrees of experience in EIT.

1 Introduction

The use of EIT in neonatal and paediatric patients is still rather limited compared with the use in adult patients. Nonetheless, several clinical studies have been published showing the potential of EIT chest monitoring in this fragile patient population, as summarized in the recent consensus article [1] with a specific online supplement dedicated to the EIT use in neonates, infants and children. EIT has been applied in the delivery room, neonatal and paediatric intensive care units, operation theatres and pulmonary function labs to assess regional lung function and its disease- and treatment-related changes.

The limited availability of EIT devices that are CE-marked for the use in neonates and infants is probably one of the reasons why the numbers of clinical studies in neonatology and paediatrics are relatively small and why EIT is not routinely used in this setting. Another reason is the general lack of a consensus on the most adequate EIT measures needed for clinical decision-making.

Therefore, we have conducted a survey among neonatologists and paediatricians active in EIT research with the aim of obtaining their personal assessment of multiple parameters that can be derived from EIT recordings.

2 Methods

36 clinicians with variable degrees of experience with EIT were asked to complete a questionnaire to evaluate 14 established EIT parameters: respiratory rate (RR), heart rate (HR), relative tidal volume ($V_{T,rel}$), absolute tidal volume ($V_{T,abs}$), ventral-to-dorsal centre of ventilation (CoV_{vd}) and ventilation ratio (VR_{vd}), right-to-left centre of ventilation (CoV_{rl}) and ventilation ratio (VR_{rl}), low tidal variation regions (LTVR), regional respiratory system compliance (C_{rs}), global inhomogeneity index (GI), coefficient of variation (CV), regional respiratory time constants (τ_e) and change in end-expiratory lung impedance ($\Delta EELI$). The questionnaire included a brief description of each parameter and its possible clinical

applications. Clinicians were asked to evaluate the EIT parameters on a numerical rating scale ranging from 0 (not useful) to 7 (very useful). We used descriptive statistics (mean \pm standard deviation) and compared the ratings of different EIT parameters with one-way analysis of variance (ANOVA) for repeated measures with Bonferroni post-test for multiple comparisons.

3 Results

34 clinicians responded to our invitation to fill in the questionnaires. 32 colleagues (clinical experience 19.4 ± 9.1 yr, experience with EIT 7.7 ± 5.8 yr) from 12 countries on three continents (Australia, Europe, South America) completed the questionnaire. 2 colleagues declined the invitation because of illness and cessation of working as a medical doctor. 2 colleagues did not react in spite of repeated invitations.

The ratings differed significantly among the parameters ($p < 0.0001$) with the highest scores given to GI (6.28 ± 0.87), LTVR (6.16 ± 0.94), $\Delta EELI$ (6.16 ± 0.87) and CoV_{vd} (6.13 ± 1.45). The lowest rating was obtained for HR (4.19 ± 2.26 , $p < 0.01$ vs. all other parameters except for $V_{T,abs}$). There were no other statistically significant differences between parameter ratings. All results are presented in Table 1.

4 Conclusions

Among the parameters in the questionnaire, GI index, LTVR, $\Delta EELI$ and CoV_{vd} were deemed particularly useful for neonatal use by a heterogeneous group of clinicians with various degrees of EIT experience. To establish a set of clinically relevant EIT measures undeniably not only subjective clinicians' assessments but also evidence-based data will be needed.

5 Acknowledgements

This study has been funded from the European Union's Horizon 2020 Research and Innovation Programme (project CRADL, grant agreement number 668259).

References

- [1] I Frerichs, MB Amato, A van Kaam et al *Thorax*, 72:83–93,2017

Table 1: Ratings for various EIT parameters, given on a 7 point scale (1-7), where 1 represented the worst and 7 the best possible rating. RR, respiratory rate; HR, heart rate; $V_{T,rel}$, relative tidal volume; $V_{T,abs}$, absolute tidal volume; CoV_{vd} , ventral-to-dorsal centre of ventilation; VR_{vd} , ventral-to-dorsal ventilation ratio; CoV_{rl} , right-to-left centre of ventilation; VR_{rl} , right-to-left ventilation ratio; LTVR, low tidal variation regions; C_{rs} , respiratory system compliance; GI, global inhomogeneity index; CV, coefficient of variation; τ_e , regional respiratory time constants; $\Delta EELI$, change in end-expiratory lung impedance.

Parameter	RR	HR	$V_{T,rel}$	$V_{T,abs}$	CoV_{vd}	VR_{vd}	CoV_{rl}	VR_{rl}	LTVR	C_{rs}	GI	CV	τ_e	$\Delta EELI$
Rating	5.22	4.19	5.84	5.34	6.13	5.88	5.97	5.69	6.16	5.69	6.28	5.81	5.56	6.16
SD	1.93	2.26	1.35	1.81	1.45	1.34	1.31	1.45	0.94	1.33	0.87	1.21	1.56	0.87

A 64-channel EIT system for the investigation of optimal measurement approaches for lung protective ventilation

Paul Wright*¹, Peter M. Green¹, Wrichik Basu¹, Michael G. Crabb², and William R. B. Lionheart²

paul.wright@manchester.ac.uk

¹School of Electrical and Electronic Engineering, ²School of Mathematics, University of Manchester, Manchester, UK

Abstract: Present lung EIT systems typically employ measurements made from electrodes describing a single transverse section through the chest. The sensitivity of measured transfer impedances to regional conductivity variation decreases with distance from this electrode plane. The full benefits of 3D reconstruction can only be realised when a 3D approach is also applied in the measurement of transfer impedances. A 64-channel EIT system is described that combines the flexibility and precision needed for the rapid experimental investigation of candidate 3D measurement strategies. Results from both phantom and human tests are presented.

1 Introduction

The continued reliance of lung EIT on a single annular arrangement of electrodes appears to be motivated more by ease of electrode application to the patient than the suitability of such arrangements for the measurement task. Indeed, the diminishing sensitivity of the transfer impedances with distance from the electrode plane suggests that such an arrangement cannot be optimal when the state of the upper and lower regions of the lungs is to be determined. Despite obvious interest in tidal conductivity variation in these ‘far from plane’ regions, there has been surprisingly little investigation of 3D measurement in human lung EIT, with even a recent ‘multiplanar’ EIT case study [1] relying on measurements from a single plane of electrodes. Crabb [2] demonstrated lung EIT from two planes of 16 electrodes, an arrangement previously shown [3] to be able to image an axially-varying conductivity inhomogeneity. Fully 3D electrode arrangements have long been standard in cranial EIT, where the skull does not lend itself to representation as the extrusion of a constant cross-section, and in industrial EIT, where multi-planar electrode arrangements are well established in the study of mixing and flow, e.g. [4]. These latter multi-planar electrode arrangements can be viewed as a boundary case, operable either as a co-operative group of planar systems, in which current flow is between electrodes within the same plane, or in a fully 3D manner, with interplane currents.

Attempts to determine optimal electrode arrangements by simulation have been frustrated by uncertainties associated with modelling errors. In this paper we describe efforts to experimentally characterise the performance of candidate electrode arrangements and measurement paradigms, using a highly flexible 64-channel EIT system developed within the R3M project.

2 Methods

Measurements of transfer impedance are made in resistor and saline tank phantoms and in human subjects using the R3M EIT system. This system uses a parallel

measurement architecture to allow high precision measurements of transfer impedance at frame rates above 30 fps. Although it is not intended that such a complex and costly system be deployed clinically, it provides a powerful tool for the rapid evaluation of strategies for future lung EIT systems. The system is controlled from a Java™ client providing full control of measurement parameters, down to the level of a single current-injection. Individual measurement requests are queued, allowing complex measurement protocols to be realised with a minimum of effort.

All measurements embody a ‘fully 3D’ ethos. Resistor phantoms are used for initial system validation. Saline tank phantom measurements are made in a torso-sized cylindrical tank featuring 4 planes of 16 equally-spaced electrodes. Measurements made on this tank phantom compare the effectiveness of in-plane and inter-plane current injection, including quantitative comparison of reconstruction results with those achievable from a single plane electrode arrangement. Initial human trials echo the electrode arrangements and measurement paradigms used in the tank (Figure 1). Subsequent human trials examine the potential advantages of alternative electrode arrangements.

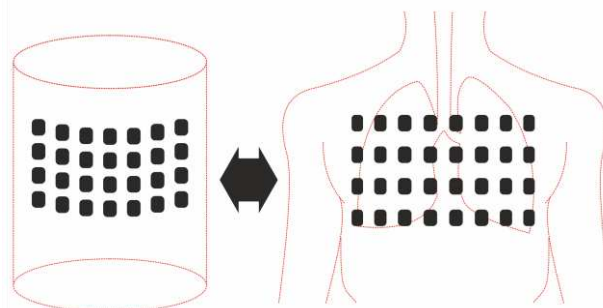


Figure 1: Corresponding saline tank and human trial electrode arrangements

3 Conclusions

Our measurements allow objective comparison of 2D and 3D approaches to EIT data collection

References

- [1] M. Miedema, A. Waldmann, K. E. McCall, S. H. Böhm, A. H. v. Kaam, and D. G. Tingay, *American Journal of Respiratory and Critical Care Medicine*, vol. 195, pp. 536-538, 2017.
- [2] M. G. Crabb, J. L. Davidson, R. Little, P. Wright, A. R. Morgan, C. A. Miller, et al., *Physiological Measurement*, vol. 35, pp. 863-879, May 2014.
- [3] J. L. Davidson, R. A. Little, P. Wright, J. Naish, R. Kikinis, G. J. M. Parker, et al., *Electronics Letters*, vol. 48, pp. 617-618, May 24 2012.
- [4] S. C. Murphy, S. J. Stanley, D. Rhodes, and T. A. York, *Measurement Science and Technology*, vol. 17, p. 3053, 2006.

Separation of 3D EIT electrode planes

Bartłomiej Grychtol¹ and Andy Adler²

¹Fraunhofer PAMB, Mannheim, Germany

²Carleton University, Ottawa, Canada

Abstract: Using multiple planes of electrodes, EIT can reconstruct three-dimensional images. For thoracic imaging, such a configuration appears to offer useful advantages, such as better slice specificity and reduced off-plane sensitivity. We describe a simulation study to determine recommendations for separation of the electrode planes.

1 Introduction

Most thoracic EIT studies have used a single plane of electrodes to reconstruct 2D images, which are sensitive to conductivity changes above and below the plane. Using two planes, it is possible to better control the vertical sensitivity of EIT [2], even if the goal is to reconstruct a better 2D slice [1]. Practically, however, it is important to have specific recommended configurations for two-plane EIT. Here we seek to understand the influence of the separation distance (s) between the electrode planes.

2 Methods and Results

Fig. 1 shows the configuration. The body is an elliptical cylinder with minor diameter 1.0. Small sagittal-plane contrasts simulated at height h above the centre of the planes.

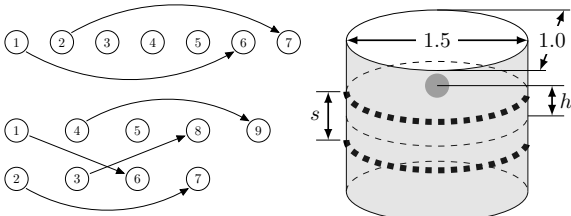


Figure 1: Left: One- and two-plane electrode configuration using the square pattern and $skip=4$; Right: Simulation geometry with electrode planes separated by s and a target h above the centre.

Reconstructions are shown for a single target position (fig. 2) for values of s , $skip$ and Noise Figure (NF).

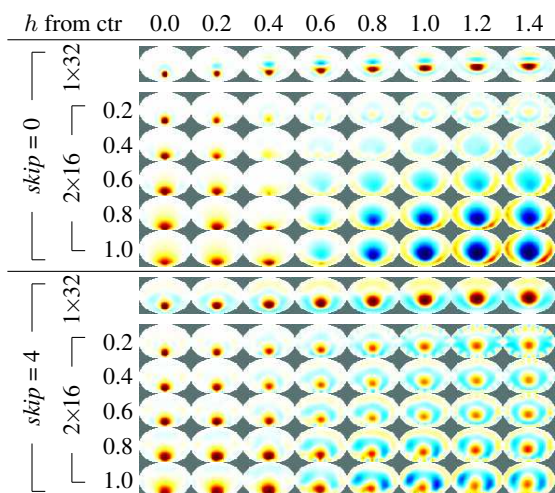


Figure 2: Reconstructed centre-slice images for an off-centre target moving vertically away from the centre plane, for $NF=1$ and the indicated plane separation. Image amplitude is normalized to the 1×32 reconstruction at each h .

For 1×32 there is a severe position error with increasing h ; targets above the plane are “pushed” to the centre. 2×16 shows less position error, but produces artefacts, especially for $skip=0$. For $s > 0.4$ resolution gets significantly worse.

To quantify the off-plane contribution, fig. 3 shows the normalized amplitude response for various algorithm parameters. We note that 1×32 shows poor off-plane sensitivity. There is a compromise between slice uniformity and slice thickness, which is worse at lower NF.

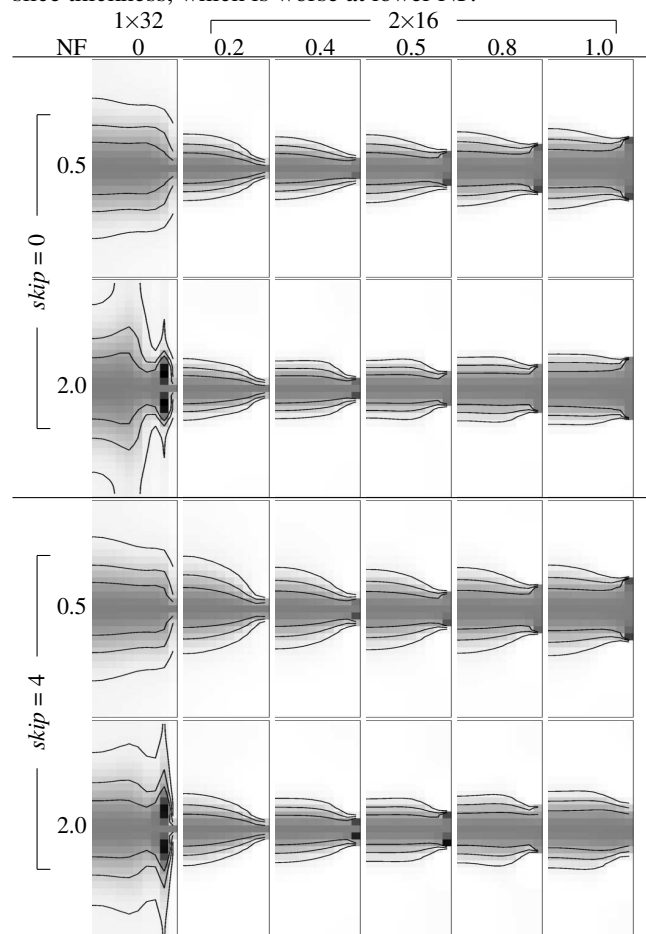


Figure 3: Normalized amplitude response (sum of in-plane image pixels divided by the value on the centre slice) for targets in the central sagittal plane. Each image has horizontal axis from centre to minor-axis side and vertical axis from $h = -1.5$ to 1.5 . Contours at 75%, 50% and 25% and only positive values shown.

3 Discussion

For thoracic EIT with two electrode planes, we study the choice of plane separation, s as a function of minimum thoracic diameter. We recommend a value between $s = 0.4$ and 0.6 (about 10 cm, adult) as the best compromise between off-plane rejection, thin imaging slice, in-plane resolution, and rejection of off-plane contrasts.

References

- [1] B Grychtol *et al*, Conf EIT 2017, Dartmouth, USA, p.7, 2017.
- [2] B Grychtol, B Müller, A Adler *Physiol Meas* 37:785–800, 2016.

Measures of lung fluid via posture-change fEIT

Xiaobo Huang¹, Hongli He¹, Jingying Luo¹, Zhanqi Zhao², Andy Adler³

¹Academy of Medical Sciences & Sichuan Provincial People's Hospital, China

²Furtwangen University, VS-Schwenningen, Germany

³Carleton University, Ottawa, Canada

Abstract: There is significant interest in possible monitoring of pulmonary oedema with EIT. One novel idea is to observe the short-term redistribution of lung fluid in patients following posture changes. We report on initial results in human subjects and a novel fEIT measure.

1 Introduction

Pulmonary oedema is the accumulation of extra-vascular fluid in the lungs. It impairs gas exchange and lung function, and can occur due to left-ventricular insufficiency or lung tissue injury. There would be considerable clinical benefit to a non-invasive ability to monitor the amount and location of oedema, and EIT has been proposed for this application by several studies (e.g. [1]). Results have been mixed, largely because it is difficult to distinguish slow changes in lung fluid from slow changes in FRC or drift in the electronics.

Recently a novel functional approach to monitor lung fluid [2] has been validated in pigs; lavage-injured animals were laterally tilted (roll) to each side. With increasing oedema, fluid filled the dependent spaces and ventilation moved more to the non-dependent lung.

The goal of this study is to examine whether these results can be reproduced in patients, and to develop relevant EIT-analysis methods.

2 Methods and Results

Subjects were adults diagnosed with ARDS, and were monitored with an invasive Pulse-Induced Contour Cardiac Output (PiCCO) which can be used as a gold-standard measure of lung water content (although not reported here).

The experimental protocol involves posture changes, as shown in fig. 1, and analysis of the EIT signal in the ten minutes following the posture change from which functional EIT parameters are calculated. On each day of the experiments (normally three days), patients are positioned at 45° to the left, 45° to the right and supine. Slow EIT changes after posture change were analysed, based on our assumption that extra-vascular fluid will slowly redistribute, followed by gas volumes.

We define two new fEIT measures based on the EIT image sequence after posture change: 1) redistribution of ventilation, $\text{RoV} = \frac{b-a}{V_T}$, and 2) redistribution of fluid, $\text{RoF} = \frac{c}{V_T}$, where tidal volume, $V_T = \sum a_i$, for each pixel i .

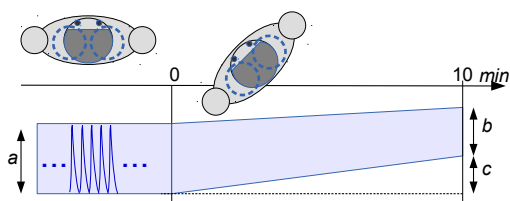


Figure 1: Block diagram of functional data analysis. After posture change, the envelope of tidal breathing (after rejecting outliers) of each EIT pixel waveform is analysed (\uparrow corresponds to $\uparrow \rho$)

Fig. 2 shows representative results for a patient on day 3 of treatment. On day 1, the left tilt image was similar, but no change was seen for the right tilt.

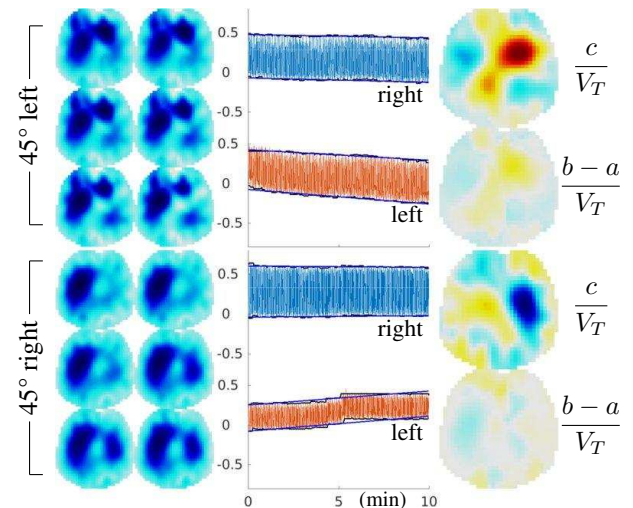


Figure 2: Left and right tilt results, for 10 min following each posture change. *Left:* end-inspiratory images (\rightarrow then \downarrow) at 0, 2, 4, 6, 8 and 10 minutes. *Middle:* time course of left and right image half and fitted trend. *Right:* fEIT images, RoF (top) and RoV (bottom).

This patient had severe left-lung oedema (fig. 3), which is consistent with the observed EIT results. With either tilt, there is little change in the right lung, which is more healthy. When tilting left, the left lung loses gas volume, especially in the non-dependent areas. When tilting right, the left lung loses fluid or gains gas volume.

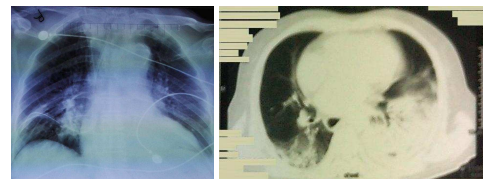


Figure 3: X-ray (*left*) and Transverse CT image (*right*) of patient in a supine position. Note severe left-lung oedema.

3 Discussion

We investigate EIT-measures of lung fluid, based on posture change-induced EIT signals. The idea is to supplement the assumptions of symmetry in the methodology of [2], since oedema is typically heterogeneous.

We develop two new fEIT measures which can be calculated from a patient in the minutes after a posture change. In this patient and others, the pattern of changes appears consistent with the distribution of oedema. In future work, we will focus on validating our calculations against PiCCO measures in these patients.

References

- [1] Victorino JA *et al*, *Am J RCCM* 169:791–800, 2004.
- [2] Trepte CJ *et al*, *Critical care* 20:18, 2016

Enhanced breast model for EIM simulation

Gerald Sze, Min Xu and Wei Wang

Micro Image Biotech Ltd, Cambridge, UK, w97wang@yahoo.co.uk

Abstract: This paper's work was based on previous simulation studies [1]. The aim of the research was to modify the 3D breast model in simulation for obtaining closer results to images that reconstructed from real data acquired by our EIM system.

1 Introduction

An electrical impedance mammography (EIM) system [2] using 85 planar electrodes has been developed for breast cancer detection. Massive simulation studies have been done with different simulation models, however images obtained from simulation were still found to have large different from human results. Hence, further studies have been carried out in terms of human breast anatomy and enhanced drawing method using higher resolution mesh.

2 Methods

Below sections introduce the two major differences (as described in sections 2.1 and 2.2) observed between results obtained from breast model using in previous simulation study (figure 1) and real data from human object measurement.

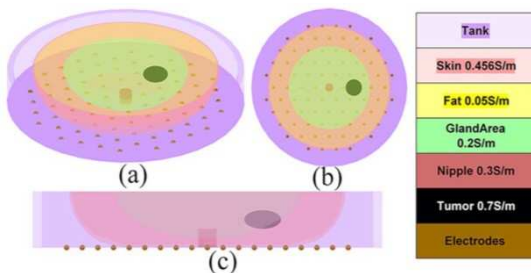


Figure 1: Breast model using in previous simulation study.

2.1 Structure inside the breast

The breast was typically defined using 4 different tissues in previous studies: skin, fat, gland area, and nipple. According to other anatomy study references [3, 4], gland area actually could be further defined by ducts and lobule.

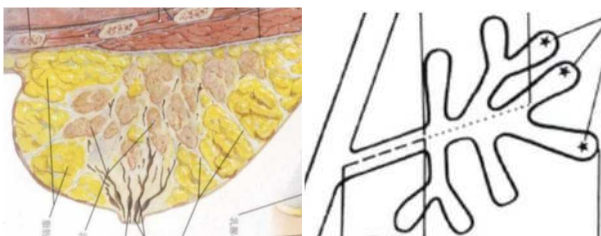


Figure 2: Look inside the breast (left); Duct, lobule, terminal duct and ductile (right)

Electrical properties of duct and lobules are difference from gland area, which are now considered as independent object in the breast model. The updated breast structure could be realized in high resolution mesh from the updated model presented in section 3.

2.2 Nipple

Nipple has higher conductivity than fat. As such a small higher conductivity circular object would usually be seen on the bottom layer of reconstructed volunteer images. Besides the x-y location of nipple was usually assumed to be located in the centre location of the breast, however it is not, and should stay close to the rear side of the body.

3 Results

Below shows the design of the updated 3D breast model, value 0 of X and Y axis indicate the centre position:

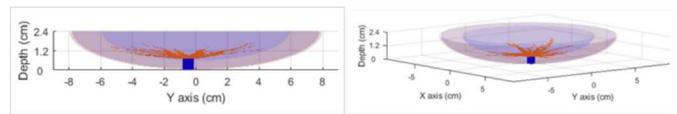


Figure 2: Different views of the updated 3D breast model.

A 2D mesh with 502 nodes and 930 elements is applied in the reconstruction process, and the whole model is divided into 4 layers. Conductivity of saline, fat, gland area, nipple and ducts were set as 0.05, 0.05, 0.08, 0.08 and 0.09 S/m respectively. Figure 3 shows the reconstructed images of the above model, the normalized (0 to 1) value of boundary between saline/fat (blueish green) and gland area (yellow) on the colorbar is around 0.7 to 0.8, which is slightly lower than the actual value.

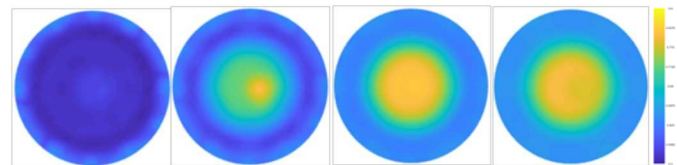


Figure 3: Reconstructed 3D breast image in simulation.

Below figures are the 3D image reconstructed from volunteer experiment. Similar structure of fat, gland area and nipple could be seen.

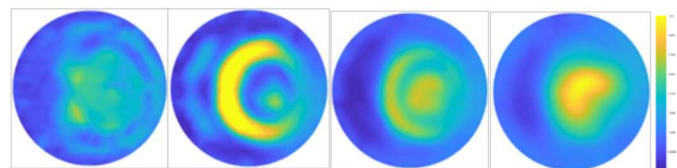


Figure 4: Reconstructed 3D image of a volunteer experiment.

4 Conclusions

Studies in human breast anatomy are carried out in order to enhance the similar between simulation and real system. This could help us customize the image reconstruction algorithm for breast imaging.

References

- [1] X Zhang, *An image reconstruction algorithm for 3-D Electrical Impedance Mammography*, IEEE trans on Medical Imaging vol. 33 no. 12, 2014
- [2] G Sze, *Dissertation*, Univ. Sussex, 2012
- [3] FH Netter, *Atlas of Human Anatomy, Sixth Edition*, 2014
- [4] SR Wellingsset *et al*, *An Atlas of Subgross Pathology of the Human Breast with Special Reference to Possible Precancerous Lesions, Sixth Edition*, Journal of the National Cancer Institute 55(2):231-273, 1975

Author Index

- Abreu, M. Gama de, 1
Adler, Andy, 2, 5, 20, 28, 43, 62, 63
Amoh, Justice, 45
Aristovich, Kirill, 11, 24, 36, 43
Arshad, Saaid H., 16, 45
Avery, James, 11, 24
- Bagnaninchi, Pierre O., 19, 41
Bardill, Andy, 50
Basu, Wrichik, 21, 61
Bayford, Richard, 26, 50, 54
Becher, Tobias, 25, 26, 60
Bergmans, D. C. J. J., 13
Bluth, T., 1
Böhm, Stephan H., 15, 27
Boyle, Alistair, 2, 20
Braun, Fabian, 23, 49
Braune, A., 1
Bronstein, Alex, 7
Brown, Alec, 29
Brück, Rainer, 46
Büchner, Steffen, 46
- Callahan, Joshua, 16
Chang, M. Y., 14
Chapman, Christopher A. R., 24
Chauhan, Munish, 8, 29, 30–32, 59
Chen, Xiao-Qian, 34, 64
Chételat, Olivier, 23, 49
Choi, Hyun Tae, 42
Crabb, Michael G., 21, 61
- Dambrun, Sébastien, 17
Demosthenous, Andreas, 50, 54
DeVries, James, 16
Dimas, Christos, 51
Donega, Matteo, 24
Dössel, O., 1
Dunne, Eoghan, 40
- Eimer, Christine, 25
Elenkov, M., 15, 27
- Fiuza, Leonardo, 11
Fortin-Pellerin, Étienne, 2
Frerichs, Inéz, 25, 26, 49, 50, 54, 60
Fu, Fanrui, 32, 59
- Gal, Robert Adrian, 35
Gelidi, Serena de, 50, 54
Gibas, Christian, 46
- Gong, Bo, 14, 56, 57
Gow, C. H., 14
Green, Peter M., 21, 61
Grychtol, Bartłomiej, 62
- Hahn, Günter, 58
Halter, Ryan J., 16, 18, 39, 45, 55
Hamilton, Sarah J., 4, 5
Hauptmann, Andreas, 4
He, Hongli, 63
Heines, S. J. H., 13
Hendler, Talma, 7
Hentze, Benjamin, 3
Holder, David S., 11, 24, 36
Hope, James, 12
Huang, Xiaobo, 63
- Indahlastari, Aprinda, 30, 31
- Jang, Geuk Young, 53
Jargal, Ariungerel, 52
Jeong, You Jeong, 42
Jia, Jiabin, 19, 41, 44, 47
Jiang, Yandan, 22
Just, Anita, 58
- Kaam, Anton van, 26, 54
Kallio, Merja, 26
Kampusch, S., 15
Kaniusas, E., 15, 27
Karadi, Zoltan, 35
Kasinadhuni, Aditya Kumar, 30, 31
Khodadad, Davood, 54
Kikuchi, Daisuke, 33
Kircher, M., 1
Koishi, Madoka, 33
Kozłowski, Edward, 6
Krueger-Ziolek, Sabine, 14, 56, 57
Kulam, Magdoom, 29–31
Kumar, Neeta Ashok, 8, 59
Kwon, Hyeuknam, 38, 48
- Leader, Geraldine, 40
Leonhardt, Steffen, 3, 17
Li, Jianping, 33
Lionheart, William R. B., 5, 21, 61
Liu, Shengheng, 19, 44
Luo, Jingying, 63
- Mareci, Thomas H., 29–31
Martucci, Maria, 39

McDaid, A., 12
 McDermott, Barry, 9
 McGinley, Brian, 9, 40
 Medvedovsky, Mordekhai, 7
 Menden, Tobias, 17
 Miedema, Martijn, 26, 28
 Möller, Knut, 14, 56, 57
 Muders, Thomas, 3
 Müller-Lisse, Ullrich, 57
 Murphy, Ethan K., 16, 18, 39, 45, 55

 Nadeau, Mathieu, 2
 Neugart, Sabrina, 37
 Nordebo, Sven, 54

 O'Halloran, Martin, 9, 40
 Odame, Kofi, 45
 Oh, Tong In, 42, 53
 Orschulik, Jakob, 17
 Ouypornkochagorn, Taweechai, 10

 Papadouri, Thalia, 26
 Paradiso, Rita, 49
 Perkins, Justin, 24
 Poll, M. C. G. van de, 13
 Porter, Emily, 9, 40
 Praud, Jean-Paul, 2
 Prosch, H., 15
 Putensen, Christian, 3

 Quintel, Michael, 58

 Rapin, Michaël, 23, 49
 Reuter, D., 27
 Roekaerts, P. M. H. J., 13
 Rutkove, Seward, 38, 39, 48
 Rymarczyk, Tomasz, 6

 Sadleir, Rosalind J., 8, 29–32, 59
 Sage, Michaël, 2
 Sajib, Saurav Z. K., 30, 31
 Sajjamark, Kulthisa, 17
 Sanchez, Benjamin, 38, 48
 Santorelli, Adam, 9, 40
 Santos, Susana Aguiar, 17
 Sapkota, Achyut, 33
 Schneider, Matthias, 37
 Schumann, Stefan, 37
 Seifnaraghi, Nima, 50, 54
 Skinner, Joseph, 39
 Soleimani, Manuchehr, 22

 Song, Yizhuang, 52
 Sophocleous, Louiza, 26
 Sorantin, Erich, 54
 Sotiriadis, Paul P., 51
 Stender, B., 1
 Stowe, Symon, 2
 Strauch, U., 13
 Strodthoff, Claas, 26
 Sze, Gerald, 34, 64

 Takei, Masahiro, 33
 Tarotin, Ilya, 36
 Thürk, F., 15, 27
 Tingay, David, 28
 Tizzard, Andrew, 50, 54
 Toth, Attila, 35
 Tran, Kiet Anh, 33
 Tschauner, Sebastian, 54
 Tsizin, Evgeny, 7

 Uzunoglou, Nikolaos, 51

 Vanholsbeeck, F., 12
 Vereczkei, Andras, 35
 Vicory, Jared, 55
 Vizvari, Zoltan, 35
 Vogt, Barbara, 49

 Wacker, Josias, 23, 49
 Waldmann, Andreas D., 26, 27, 54
 Walter, Marian, 3, 17
 Wang, Wei, 34, 64
 Weiler, Norbert, 25, 49
 Wendler, Anna, 25
 Wenzel, Christin, 37
 Wodack, K., 27
 Woo, Eung Je, 42, 53
 Wright, Paul, 21, 61
 Wu, Hancong, 19, 41, 47
 Wu, Xiaotian, 18
 Wu, Yu, 50

 Xi, Andrew, 59
 Xu, Min, 34, 64

 Yang, Yunjie, 19, 41, 47
 Yerworth, Rebecca J., 26

 Zhang, Tingting, 53
 Zhao, Zhanqi, 14, 63
 Zimmermann, Hanna, 57

Thank you to the sponsors of EIT2018

